Comparative Study of Phase Behaviour and Structure of a Water Soluble Synthetic Polymer and an Elastin-like Peptide

Vergleichende Studie des Phasen Verhaltens und Struktur eines Wasser Löslichen Synthetischen Polymer und einem Elastin-artigen Peptid

Zur Erlangung des Grades eines Doktors der Naturwissenschaften (Dr. rer. nat.)
genehmigte Dissertation von Alexander Daniel Matt aus Hanau
Tag der Einreichung: 08.10.2018, Tag der Prüfung: 05.11.2018
Darmstadt 2018 — D 17

1. Gutachten: Prof. Dr. B. Stühn
2. Gutachten: Prof. Dr. M. Vogel

TECHNISCHE
UNIVERSITÄT
DARMSTADT

Fachbereich Physik
Exp. Physik kondensierter Materie

Comparative Study of Phase Behaviour and Structure of a Water Soluble Synthetic Polymer and an Elastin-like Peptide
Vergleichende Studie des Phasen Verhaltens und Struktur eines Wasser Löslichen Synthetischen Polymer und einem Elastin-artigen Peptid

Genehmigte Dissertation von Alexander Daniel Matt aus Hanau

1. Gutachten: Prof. Dr. B. Stühn
2. Gutachten: Prof. Dr. M. Vogel

Tag der Einreichung: 08.10.2018
Tag der Prüfung: 05.11.2018

Darmstadt 2018 — D 17

Comparative Study of Phase Behaviour and Structure of a Water Soluble Synthetic Polymer and an Elastin-like Peptide

This work concerns itself with the structure and phase behaviour of water soluble macromolecules. The molecules are studied in solutions of different concentrations and the solutions are also brought into a soft confinement. We will study the influence of different chain ends of a polymer on the phase boundaries and structure formation of the bulk solution as well as on the surfactant layer of a water in oil microemulsion in the droplet phase providing the soft confinement. It will also be discussed how increasing temperature and chain length of the polymer changes the stability and radius of the microemulsion droplets. Further we will analyse structural changes of a peptide in a buffer solution in bulk and the microemulsion soft confinement.

DSC measurements are performed to establish the phase diagram of the water polymer mixtures and they reveal that an eutectic system is formed, regardless of the endgroup of the polymer. Structure formation of the polymer water mixtures is observed via WAXS and SAXS measurements, which reveal that upon crystallisation the polymer and water separate before freezing, instead of forming a solid solution or mixed crystal. For some concentrations of polymer the formed hexagonal ice crystal exhibits a preferred growth direction, that is independent of the endgroups. But there is also a concentration and temperature dependent preferred growth direction of the polymer crystal for one set of endgroups that is not found in the other set. Further it can be seen that adding water to the polymer increases the long period of the polymer crystal, by increasing the thickness of the crystalline phase instead of the amorphous phase. Only for high concentrations of water in the mixture there is an increase in the long period with increasing temperature.

SANS measurements are used, to analyse the structural conformation of the peptide in the buffer solution. Here we find that the radius of gyration of the peptide increases with temperature and concentration hinting at a strong aggregation process, except for low concentrations of peptide. In those samples it is possible to see an inverse temperature transition of the peptide. The structural conformation of the peptide is more that of a flexible polymer chain than of a folded particle, but deviates from the flexible behaviour with decreasing concentration.

To analyse the influence of polymer concentration, chain length and endgroups on the stability of the surfactant layer of the microemulsion droplet, BDS and SAXS measurements are employed. We find that the stability of the droplet depends highly on the number and size of the polymer chain, but not on the endgroups. There is an ideal polymer size and number of polymer chains inside the droplet at which the destabilisation or stabilisation of the droplet is maximal. The radius of the microemulsion droplets decreases with temperature regardless of their degree of stability. But stabilised droplets exhibit a slower decrease in radius than destabilised droplets. An attractive interaction between surfactant shell and polymer is found for both types of endgroups.

Finally, we use SANS and SAXS measurements in order to study the conformation of the peptide and of the surfactant layer in the microemulsion droplet phase. The peptide does not destroy the droplet phase and seems to adsorb at the surfactant interface, just like the polymer. This stabilises the droplet, which still decreases in radius with increasing temperature.

Vergleichende Studie des Phasen Verhaltens und Struktur eines Wasser Löslichen Synthetischen Polymer und einem Elastin-artigen Peptid

Diese Arbeit beschäftigt sich mit der Struktur und dem Phasenverhalten von wasserlöslichen Makromolekülen. Die Moleküle werden in Lösung mit verschiedenen Konzentrationen und die Lösungen in einen weichen räumlichen Einschluss untersucht. Wir ermitteln den Einfluss den verschiedene Kettenenden eines Polymers auf die Phasengrenzen und die Strukturbildung in der Lösung haben, genauso wie den Einfluss auf die Tensid-Schicht einer Wasser-in-Öl Mikroemulsion, die sich in der Tröpfchen-Phase befindet. Auch wird der Einfluss von steigender Temperatur und Kettenlänge des Polymers auf die Stabilität des Mikroemulsionströpfchens diskutiert. Weiterhin analysieren wir die Strukturveränderung eines Peptids in einer Pufferlösung und im räumlichen weichen Einschluss einer Mikroemulsion.

Dynamische Differenzkalorimetrie wird genutzt um das Phasendiagramm der Wasser Polymer Mischung zu erstellen und es zeigt sich, dass ein eutektisches System vorliegt, unabhängig davon, welches Kettenende vorliegt. Die Strukturbildung der Wasser Polymer Lösung wird mit Hilfe von Röntgenweitwinkel- und Röntgenkleinwinkelstreuung untersucht, die zeigt, dass das Wasser und das Polymer separieren, bevor es zur Kristallisation kommt. Dabei formt sich kein Mischkristall. Lösungen die eine bestimmtew Konzentration Polymer aufweisen bilden einen hexagonalen Eiskristall mit einer bevorzugten Wachstumsrichtung aus, die wieder unabhängig von den Kettenenden ist. Aber es existiert auch eine konzentrations- und temperaturabängige bevorzugte Wachstumsrichtung des Polymerkristall, allerdings nur für einen Typ Kettenende. Weiterführend stellen wir fest, dass die Zugabe von Wasser die Langperiode des Polymerkristalls verlängert, indem sich die Dicke der kristallinen Phase, anstatt der amorphen Phase, erhöht. Nur für hohe Wasserkonzentrationen vergrößert sich die Langperiode mit steigender Temperatur.

Neutronenkleinwinkelstreuung wird genutzt, um die strukturelle Konformation eines Peptids in einer Pufferlösung zu untersuchen. Es stellt sich heraus, dass der Gyrationsradius des Peptids sich mit steigender Temperatur und Konzentration vergrößert, was für einen starken Aggregationsprozess spricht. Für geringe Konzentrationen des Peptids zeigt sich jedoch ein anderes Verhalten. In diesen Proben ist es möglich den inversen Temperatur Übergang des Peptides zu sehen. Die strukturelle Konformation des Peptides entspricht mehr der Konformation einer flexiblen Polymerketten, als der eines gefalteten Partikels, aber weicht bei geringer Konzentration an Peptid mehr von dem Verhalten einer flexiblen Polymerkette ab.

Um den Einfluss von Polymerkonzentration, Kettenlänge und Kettenenden auf die Stabilität der Tensidschicht eines Mikroemulsionströpfchen zu untersuchen, führen wir Breitband dielektrische Spektroskopie und Röntgenkleinwinkelstreuung durch. Die Stabilität des Tröpfchens hängt dabei stark von der Anzahl und Größe der Polymerketten im Tröpfchen ab, aber nicht von den Kettenenden. Es exisitiert eine ideale Kettenlänge und Kettenanzahl, bei welcher das Tröpfchen maximal stabilisiert bzw. destabilisiert wird. Der Radius der Mikroemulsionströpfchen verringert sich mit steigender Temperatur, unabängig davon, ob es stabilisiert oder destabilisiert wird. Aber stabilisierte Tröpfchen zeigen eine verringerte Abnahme im Radius im Vergleich zu stabilisierten Tröpfchen. Eine

attraktive Wechselwirkung zwischen Tensidschicht und Polymer wird für alle Kettenenden gefunden.

Abschließend ermitteln wir die Konformation des Peptides und der Tensidschicht für Mikroemulsionen in der Tröpfchenphase. Das Peptid zerstört die Tröpfchenphase nicht und scheint an der Tensidschicht zu adsorbieren, wie das Polymer. Dies stabilisiert das Tröpfchen, dessen Radius sich immernoch mit steigender Temoperatur verringert.

Contents

1 Introduction

The internal conformation and structure of a protein depend highly on the hydrogen bonds the protein forms with its environment [1,2]. So due to the weakness of hydrogen bonds, when compared to $k_b T$, even small changes in the protein surroundings, like an increase in temperature or a different pH value, can cause the total loss of the biological function. Therefore it is of utmost importance to study the behaviour of proteins in changing environments in order to better understand the process of denaturation and to find possible countermeasures. Because the environment of a protein inside a human cell, for example, is very complex and the cell walls and other molecules act as confining influences it is much more reasonable to first study the protein in a much simpler environment, like pure water. The hydrogen bond network of water has been extensively studied [3,4] and most proteins dissolve in water, even if they contain very hydrophobic amino acids. In a protein water mixture the influence of changes in temperature, protein concentration or even addition of foreign crowding molecules etc. can be studied in great detail [5,6].

Since every protein consists of different sequences of amino acids it would be necessary to study every single protein in many different environments and under various conditions in order to obtain the desired knowledge of protein functionality. This is very impractical and thus it is much more sensible to study smaller amino acid sequences that occur in different proteins and to find similarities to other molecules. In recent years it has become common to compare protein water mixtures to polymer water mixtures and while there are many key differences between polymers and proteins, they also have some common properties. Polymers are able to form secondary structural elements, like helices or random coils, [7] and start to form aggregates under the same conditions as proteins [8–10]. So by choosing a polymer that exhibits the same properties as the protein under investigation, a very suitable model system can be obtained.

Polyethylene glycol (PEG) is a polymer very suitable for the task of standing in for a protein, because it dissolves in water at all concentrations above T_c [11], has a high ratio of hydrophobic to hydrophilic bonds [11,12] and at high temperatures there exists a lower critical solution temperature (LCST) [11,13]. These are all properties that polyethylene glycol shares with some proteins, for example elastin [14–17]. There are many studies concerning themselves with the influence of polymer chain length, polymer concentration, temperature, foreign molecule addition etc. in polyethylene glycol and water mixtures and thus it would be very useful to be able to draw on that wide knowledge in order to better understand the interplay between water and proteins.

To evolve the situation from the bulk solution one step closer to the environment found in a living cell many different approaches are possible. A second polymer standing in for another protein could be introduced, salts can be brought in and the mixture could be introduced into a soft confinement reminiscent of the confinement provided by the cellular walls. It has been found that the droplet phase of a microemulsion can provide such a confinement and the interactions between the confinement and polymers have already been studied to a great extent [18–23].

Inside a microemulsion a polar component, mostly water, and an unpolar component , mostly oil, are stabilised by a so called surfactant molecule, which has amphiphilic properties. The resulting microemulsion is thermodynamically stable and macroscopically isotropic. The structures formed in microemulsions are on a nano meter length scale and thus it is optically transparent [24]. The structures formed by microemulsions strongly depend on the concentration of the three components and at the right ratios water droplets dissolved in an oil matrix (w/o) or oil droplets dissolved in a water matrix (o/w) can form. The radius of these droplets is in the nano meter range and is tunable by changing the composition [24]. The surfactant shell of the droplets has a rather low rigidity, coining the term soft confinement [18], and thus can model the lipid bilayer surrounding a living cell very well.

Adding polymer inside the droplet can have no effect or the polymer might stabilise or destabilise the droplet [23,25]. So not only might the polymer be influenced by the confinement [22], but the polymer may influence the confinement as well. So it would not be surprising, if there is a reciprocal interaction between a protein and the surfactant shell of the soft confinement. Since there are many similarities between polymer and proteins in bulk solution, this interaction might be the same for proteins as it is for polymers.

So while bulk solutions and the confinement by a microemulsion droplet are both situations very far from the real architecture of a living cell, the investigation of these two systems will deepen the knowledge of protein structure and functionality. This is a necessary step in order to come closer to a complete understanding of the interaction of a protein with its environment inside a living cell.

After important theoretical concepts and the experimental methods are introduced, this thesis will concern itself with the structures formed in water and PEG mixtures upon freezing in order to understand the crystallisation behaviour. Then the polymer is introduced into the confinement provided by the w/o droplet phase of a microemulsion and the interplay between the polymer and the surfactant shell is investigated. Using concepts from polymer physics, the structure of an Elastin-like peptide in a buffer solution is then studied and compared to results obtained for PEG due to similar properties. The peptide is also introduced in the before mentioned confinement and from very few selected measurements extensive results can be derived based on the investigations on the confined PEG.

Part I.

Basic Concepts and Experimental Methods

2 Basic Concepts and Theoretical Models

Binary mixtures of water and polyethylene glycol (PEG) ranging from 5 to 95 wt% PEG will be studied in this work. Generally the phase diagram of such mixtures can be derived by the Flory-Huggins theory, which will be introduced in 2.1.1. This theory can also be used to describe the melting point depression that occurs by adding water to PEG and vice versa.
Furthermore peptide buffer solutions containing between 5 and 20 wt% peptide will be studied and thus section 2.1.4 will introduce key concepts about proteins and peptides, focusing mainly on their structure and biological functionality.
The droplet phase of a water-in-oil microemulsion will be used as the soft confinement in this work. A microemulsion is a ternary mixture comprising water, oil and a surfactant that presents microstructures on the nano meter scale. These structures can be observed and studied by using static scattering techniques, while the dynamics of such a system will be studied using dielectric spectroscopy. More details on microemulsions will be provided in 2.2

2.1 Binary Mixtures

As mentioned before there will be two types of binary mixtures studied in this work. The first are mixtures of water and PEG with a wide ranging volume fraction of PEG. In order to determine, if water and PEG form a homogeneous mixture or separate into a two phase system, one can turn to the Flory-Huggins theory. This mean-field approach reduces the question of miscibility to a single temperature depending parameter [7,26]. A detailed description and derivation of this model will be given in the following paragraph and can be found in additional literature [7,26]. Further this model will be used to calculate the melting point depression of the studied mixtures.

The second system is a solution consisting of a chemical buffer and an Elastin-like peptide. The concentration of peptide in the mixtures is smaller than 20 wt%. Biomolecules such as proteins and ELPs serve a biological function that can be lost due to denaturation [2,27]. Since the interaction of a biomolecule with its solvent depends strongly on the type of molecule, its size, surroundings etc. Chapter 2.1.4 will give a short introduction to the properties of proteins and peptides.

2.1.1 Theory of Water/Polymer Solutions: Flory-Huggins

To be able to predict, if two simple liquids form a homogeneous mixture or separate into a two phase system, one needs to consider the (Helmholtz) free energy of mixing F_{mix}. The Helmholtz free energy F can be used to describe the system, instead of the Gibbs free energy G, because the volume of the system is assumed to be constant. F_{mix} can be calculated by comparing a system of two components A and B in two different states. The

two species can exist in a single, mixed phase with free energy F_{A+B} or A and B can exist in separate, unmixed states, thus the free energy would be $F_A + F_B$. So the free energy of mixing becomes: [7,26]

$$F_{mix} = F_{A+B} - (F_A + F_B) \tag{2.1}$$

Since

$$F = U - TS \tag{2.2}$$

it is necessary to know the change of entropy on mixing S_{mix} and the change of inner energy on mixing U_{mix}. In order to calculate F_{mix} Flory and Huggins derived a mean field theory in which the molecules of the two components are arranged on a lattice. Each lattice site has z nearest neighbours. Introducing the volume fractions ϕ_A and ϕ_B of the two components as the probability that a lattice site is either occupied by a molecule of type A or B and making the assumption that the volume of the system is constant $\phi_A + \phi_B = 1$, the entropy of mixing can be expressed as: [7,26]

$$S_{mix} = -k_B(\phi_A \ln\phi_A + \phi_B \ln\phi_B) \tag{2.3}$$

Calculating the inner free energy of mixing U_{mix} can be achieved by assuming that the molecules only interact with their nearest neighbours (z). The interaction between two molecules of type A is given by ϵ_{AA}, between two molecules of type B by ϵ_{BB} and the interaction between a molecule of type A and a molecule of type B is described by ϵ_{AB}. Thus U_{A+B} can be calculated to: [7,26]

$$U_{A+B} = \frac{z}{2}(\phi_A^2 \epsilon_{AA} + \phi_B^2 \epsilon_{BB} + 2\phi_A \phi_B \epsilon_{AB}) \tag{2.4}$$

To obtain U_{mix} the energy of the unmixed state needs to be subtracted from U_{A+B} resulting in:

$$U_{mix} = \frac{z}{2}\left[(\phi_A^2 - \phi_A)\epsilon_{AA} + (\phi_B^2 - \phi_B)\epsilon_{BB} + 2\phi_A \phi_B \epsilon_{AB}\right] \tag{2.5}$$

Using the dimensionless Flory interaction parameter

$$\chi = \frac{z}{2k_B T}(2\epsilon_{AB} - \epsilon_{AA} - \epsilon_{BB}) \tag{2.6}$$

This becomes:

$$\frac{U_{mix}}{k_B T} = \chi \phi_A \phi_B \tag{2.7}$$

So χ can be interpreted as the energy it takes to take a molecule of type A out of an environment of pure A and put into an environment of pure B. It should be noted that $\chi \propto T^{-1}$ only holds true for nearest neighbour interaction. Combining the results for S_{mix} and U_{mix} and inserting them into $F = U - TS$, the free energy of mixing per lattice site can be obtained: [7,26]

$$\frac{F_{mix}}{k_B T} = \phi_A \ln\phi_A + \phi_B \ln\phi_B + \chi \phi_A \phi_B \tag{2.8}$$

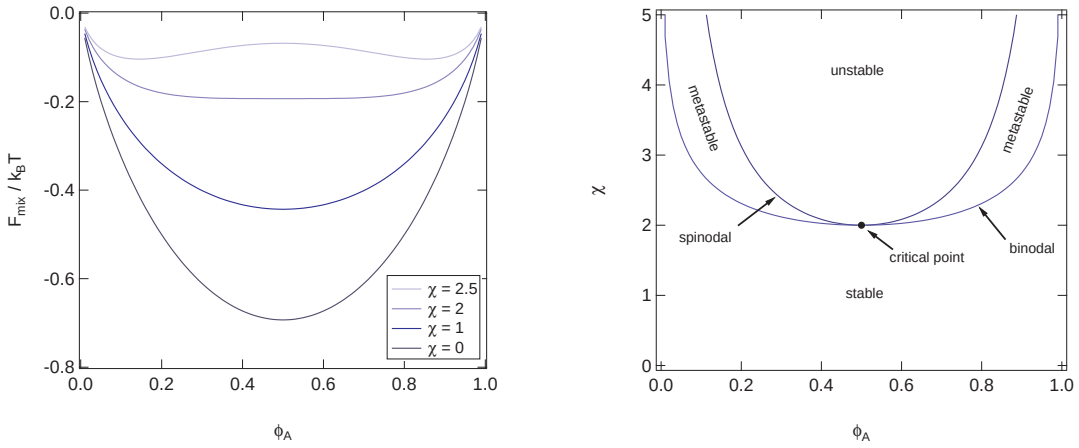

Figure 2.1.: Left: The free energy of mixing, as derived by the Flory-Huggins theory, for different values of the interaction parameter χ. Right: The ϕ_A χ plane of the phase diagram of a binary mixture.

Figure 2.1 shows the value of F_{mix} for different values of the interaction parameter χ. The curves illustrate that at $\chi = 2$ the behaviour of the mixture changes. For $\chi < 2$ the curve is concave with a single minimum at $\phi_A = 0.5$, thus demixing into two phases with different composition will increase the free energy. This can be made clear by looking at a connecting line between the free energy of mixing of two phases with different composition. Every point of this line lies above the free energy of mixing of the homogeneous phase that the two phases can form by mixing. However for $\chi \geqslant 2$ the minimum at $\phi_A = 0.5$ becomes a maximum and two minima appear. Between the two minima and the maximum two inflexion points arise also. Every mixture with a composition between those two inflexion points is unstable and therefore will demix. However, if concentration fluctuations are large enough, demixing can also occur for a composition located between a minimum and an inflexion point. This composition region is called metastable. The right side of figure 2.1 illustrates this, by showing the ϕ_A χ plane of the phase diagram of a binary mixture. As discussed for $\chi < 2$ all compositions are stable. The spinodal line is given by the positions of of the inflexion points, while the binodal line is given by the positions of the minima. The passing of the phase boundary from the meta-stable region into the unstable region causes the mixture to demix. However this process is not instantaneous, for it follows very complex kinetics, described by the theory of spinodal decomposition. This theory lies outside the scope of this thesis and the reader is thus referred to further literature on this theory[26]. The Flory-Huggins theory can easily be generalised in order to describe polymer solutions and polymer blends. The theory is adjusted so that now not a molecule, but a monomer of the polymer sits on one lattice site, thus at least one neighbouring lattice site needs to be occupied by another monomer of the polymer. So the degree of polymerisation, N_A and N_B, needs to be considered. The free energy of mixing becomes:[7]

$$\frac{F_{mix}}{k_B T} = \frac{\phi_A}{N_A} \ln \phi_A + \frac{\phi_B}{N_B} \ln \phi_B + \chi \phi_A \phi_B \tag{2.9}$$

For a simple liquid the degree of polymerisation becomes one.

2.1.2 The Crystallisation Process

Before calculating the melting point depression inside the scope of the Flory-Huggins theory, this paragraph will discuss the process of crystallisation. A liquid is a state in which there is no long range order in contrast to a crystal in which every molecule has a definite lattice position causing a high degree of long range order. The theory of the crystallisation process is much more complicated than the liquid-liquid-unmixing transition and lies outside the scope of this work. For a mean-field theory of the process the reader is referred to [28]. Here the phenomenology of crystallisation will be discussed.

Looking again at the free energy, it can be seen that at the transition from a liquid to a crystal, the derivatives of the free energy with respect to other thermodynamic variables are discontinuous [26], making it a first order phase transition. The entropy of freezing can be calculated by: [26]:

$$\Delta S_m = \frac{\Delta H_m}{T_m} \tag{2.10}$$

Where ΔH_m is the latent heat released at the melting temperature. The melting temperature is the temperature at which the free energy of the liquid is equal to the free energy of the solid. So a liquid that is held at the melting temperature, if it is free of impurities and the walls of its confinement do not affect it, will never freeze, because creating a crystal costs free energy. The crystal will have an interface with the liquid associated with the interfacial energy γ_{sl}. It is clear from this that in order to create a crystal, the liquid must be undercooled below its melting point. The process of nucleation then initiates freezing. Since melting/freezing processes are often characterised by the latent heat released and investigated at constant pressure rather than constant volume, the Gibbs free energy G is investigated to describe the nucleation happening upon freezing, instead of the Helmholtz free energy F.

The spontaneous appearance of a crystal nucleus initiates "homogeneous nucleation". Assuming a spherical crystal with radius r, the change in free energy can be written as a sum of two terms. One term contains the contribution of the liquid to solid interface with the interfacial energy γ_{sl}, while the other term is proportional to the volume of the crystal, containing the change in Gibbs free energy on going from liquid to solid : [26]

$$\Delta G(r) = \frac{4}{3}\pi r^3 \Delta G_b + 4\pi r^2 \gamma_{sl} \tag{2.11}$$

The change in free energy is shown in figure 2.2.

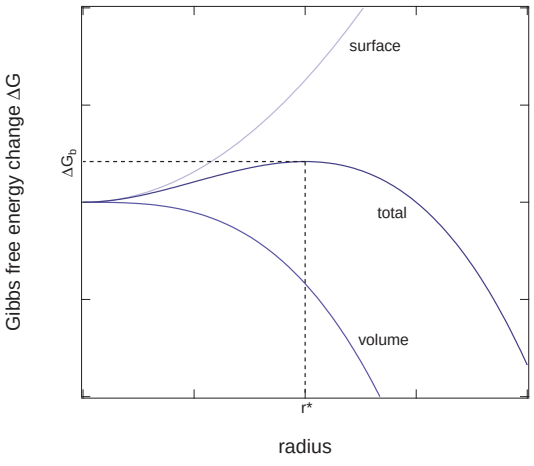

Figure 2.2.: Gibbs free energy of the liquid solid transition. The total change of free energy is shown as well as the contributions of the two terms. Further the Gibbs free energy on going from liquid to solid and the critical radius r^* is shown

The Gibbs free energy change per unit volume when a melt is undercooled by ΔT is given by: [26]

$$\Delta G_b = -\frac{\Delta H_m}{T_m}\Delta T \tag{2.12}$$

So equation 2.11 becomes:

$$\Delta G(r) = -\frac{4}{3}\pi r^3 \frac{\Delta H_m}{T_m}\Delta T + 4\pi r^2 \gamma_{sl} \tag{2.13}$$

At the critical radius r^* the change of Gibbs free energy has a maximum. This radius can be calculated to:

$$r^* = \frac{2\gamma_{sl} T_m}{\Delta H_m \Delta T} \tag{2.14}$$

Only crystals that have a larger radius than r^* will continue to grow, while crystals smaller than r^* will remelt. This is illustrated im figure 2.2, where it can be seen that crystal growth only lowers the Gibbs free energy if the radius is larger than r^*. The energy barrier that must be overcome in order to nucleate a viable crystal can be calculated with the critical radius: [26]

$$\Delta G^* = \frac{16\pi}{3}\gamma_{sl}\left(\frac{T_m}{\Delta H_m}\right)^2 \frac{1}{\Delta T^2} \tag{2.15}$$

The probability of a crystal being nucleated is a very strong function of temperature, since it is proportional to $e^{(-\Delta G^*/k_B T)}$ [26]. This would indicate that a significant rate of nucleation can only be observed tens of degrees below the melting point. The reason for this deviation from reality is that liquids are usually not completely pure and the contained impurities provide sites for nucleation. So one must expand from a theory of homogeneous to one of heterogeneous nucleation.

Taking into account the contact angle θ between a heterogeneously nucleated crystal and a solid surface the energy barrier for nucleation becomes: [26]

$$\Delta G^* = \frac{16\pi}{3}\gamma_{sl}\left(\frac{T_m}{\Delta H_m}\right)^2 \frac{1}{\Delta T^2}\frac{(1-cos\theta)^2(2+cos\theta)}{4} \tag{2.16}$$

For a derivation of this equation the reader is referred to [26]. It can be seen that the energy barrier is modified by a term including only the contact angle θ. This term becomes zero for a contact angle of 0°, yielding the result obtained for homogeneous nucleation. Increasing the contact angle causes the term to take on values smaller than one and thus reducing the energy barrier. This explains why impurities cause crystallisation to take place at lesser undercooled temperatures when compared to pure materials.

2.1.3 Melting Point Depression

Combining a polymer and a solvent into a homogeneous liquid will result in a different melting temperature than those of the two pure components. In the following the melting point depression of a solvent by adding polymer and vice versa will be discussed. Using the Flory-Huggins theory (2.1.1) the molar Gibbs energy of mixing ΔG can be calculated to: [29–31]

$$\frac{\Delta G}{RT} = n_A \ln\phi_A + n_B \ln\phi_B + \phi_A \phi_B \chi \tag{2.17}$$

where R is the Gas-constant and n_A/n_B is the number of moles of solvent and polymer. This equation is similar to equation 2.9 and contains the number of moles instead of only the volume fraction.

The activity a of either component can be written as: [31]

$$\ln a = \frac{\Delta H}{R}\left[\frac{1}{T_m^0} - \frac{1}{T_m}\right] - \Delta c_p \ln\frac{T_m^0}{T_m} - \Delta c_p T_m^0 \left[\frac{1}{T_m^0} - \frac{1}{T_m}\right] \tag{2.18}$$

Where T_m is the temperature at which the solution is in equilibrium with the corresponding liquid phase, T_m^0 is the melting temperature of the pure component, R is the gas constant, ΔH is the molar heat of fusion of the pure component at T_m^0 and Δc_p is the difference between the molar heat capacity of the solid and the partial molar heat capacity of the same component in solution. In the following the Δc_p term will be omitted, since the temperature dependence of the heats of fusion can be neglected for the samples investigated in this work [31].

The activity a_A of the solvent can also be expressed as: [31]

$$\ln a_A = \left[\ln\phi_A + \left(1 - \frac{1}{V_r}\right)(1-\phi_A) + \chi(1-\phi_A)^2)\right] \tag{2.19}$$

with $V_r = v_B/v_A$ as the ratio of molar volumes of polymer and solvent. For the activity a_B it follows: [31]

$$\ln a_B = R\left(\frac{V_u}{V_A}\right)\left[\ln(\phi_B)\frac{1}{V_r} - \left(1 - \frac{1}{V_r}\right)(1-\phi_B) + \chi(1-\phi_B)^2\right] \tag{2.20}$$

With V_u as the volume of the polymer repeat unit and V_A as the volume of the solvent molecule. By combining the two equations for the activity of the solvent and the polymer the melting point depression can be calculated to: [30,32]

$$\frac{1}{T_{MA}} - \frac{1}{T_{MA}^0} = \frac{-R}{\Delta H_A}(\ln(1-\phi_B) + \left(1 - \frac{1}{V_r}\right)\phi_B \chi \phi_B^2) \tag{2.21}$$

Where T_{MA} is the "depressed" melting temperature, T_{MA}^0 is the melting temperature of the pure solvent, ΔH_A is the molar melting enthalpy of the solvent. For the melting point of the polymer follows: [30,32]

$$\frac{1}{T_{MB}} - \frac{1}{T_{MB}^0} = \frac{-RV_u}{\Delta H_B V_A}\left(\left(1 - \frac{1}{V_r}\right)\phi_A - \frac{1}{V_r}\ln(1-\phi_A) - \chi\phi_A^2\right) \tag{2.22}$$

Where T_{MB} is the "depressed" melting temperature, T^0_{MB} is the melting temperature of the polymer and ΔH_B is the molar melting enthalpy per monomer of polymer. It is obvious that, if the solvent melting point gets depressed as well as the polymer melting point that both equations are only valid for a certain concentration range. By adding polymer to the solvent the melting point will first be depressed, but at some concentration the melting point will increase again in order to match the melting temperature of the pure polymer. This concentration can be found by calculating/measuring the intersection between the two functions. It should also be mentioned that the depressed melting point references the temperature at which a homogeneous liquid mixture of the two components is in equilibrium with another phase containing a solid phase. In the case of an eutectic system this would correspond to the so called "liquidus line", where the homogeneous liquid phase is in equilibrium with a phase consisting out of a solid and a liquid. The "eutectic line" occurring in eutectic systems, yields the temperature at which a phase consisting of only solids is in equilibrium with the phase containing a solid and liquid mentioned before. The eutectic line can not be calculated with this theory, except at the eutectic concentration, where liquidus and eutectic line intersect.

The assumption of the Flory Huggins theory that the interaction parameter χ does not depend on the concentration of polymer is only true for some polymers[30]. In other cases χ might increase or decrease with increasing polymer concentration. In order to take that concentration dependence into account, but not deviate much from the result derived by Flory and Huggins, the interaction parameter χ will be expanded into a power series:[29,30,33]

$$\chi = \chi_0 + \chi_1 \phi_B + \chi_2 \phi_B^2 \tag{2.23}$$

It should be noted that this representation is just a phenomenological expression to describe experimental findings. So the parameters χ_0, χ_1, χ_2 can only be seen as indicators of how strong χ changes with polymer concentration.

Water and Polyethylene Glycol Mixtures

There are many studies concerning themselves with mixtures of water and polyethylene glycol (PEG), so this section will focus on results related to this work. PEG has a unique solubility in water. It is the only water soluble polyether[11,34] and is completely miscible in water above the melting temperature of PEG and below the miscibility gap[13,34]. Below the melting temperature of PEG the system shows eutectic behaviour. Two phase transitions can be measured, one whose transition temperature is independent of concentration (eutectic) and one where the transition temperature depends strongly on concentration (liquidus)[30]. This only holds true for polymer chains large enough (>1000g/mol), for smaller chains the crystallization of the mixture is hindered and does not show two or any phase transitions for some concentrations, because the pure PEG does not crystallise and only shows a glass transition[30].

PEG can be synthesised with different endgroups. There can be an -OH group on both ends or a -OCH_3 group and of course there can be both one on each end. Changing the endgroup however has no large influence on the solubility, but rather on the solvating process. Since the -$CH_2 - CH_2$ unit is hydrophobic, water forms a hydration shell around

it. If both chain ends are -OH groups, the polymer will dissolve. But the -OCH_3 is also hydrophobic, so it hast to "stick" to other hydrophobic units creating a network[12]. So the reason, why PEG still dissolves in water even with hydrophobic endgroups can not be found by looking at the number of hydrophobic bonds, but rather is a structural aspect. Bringing PEG inside the water disturbs its hydrogen bond network and in order to dissolve it the water needs to incorporate the PEG molecule inside the network by hydrogen bonding. It has been suggested that the distance between oxygen atoms plays a deciding role in the solubility of PEG, since the distance equals that of oxygen atoms in the water network. This would also explain why other polyethers are not soluble in water and the hydrophobicity of the endgroup only has a minor influence on the solubility of PEG.[11,12].

2.1.4 Proteins and Peptides

Since this work studies the similarities and differences between an Elastin-like peptide and a synthetic polymer, some key features of proteins and peptides will be explained here. For a deeper introduction into proteins and their functionality the reader is referred to further reading[1,2].

Amino acids are the building blocks that make up a protein. They are connected via peptide bonds in which the nitrogen atom of the amino group of one amino acid binds to the carboxy group of another amino acid. In this process two hydrogen atoms of the amino group and the single bonded oxygen atom of the carboxy group bind together and are expelled as water[1,2]. Proteins are polypeptides that contain 50 or more amino acids, molecules containing less then 50 amino acids are called peptides[1].

Proteins and peptides form very complex structures that are categorised in primary, secondary, tertiary and quaternary structure, with each step increasing in complexity[1,2].

- **Primary structure**

  The primary structure of a protein is the sequence of amino acids it contains, starting with the N-terminal and ending with the C-terminal amino acid[2]. In this structure one can already see, if a protein contains some repeating amino acids blocks that can be compared to the monomers of a (Block-)copolymer.

- **Secondary structure**

  Amino acids in a protein form a local conformation that is called the secondary structure. This structure is stabilised by hydrogen bonds between the amino group and keto group of the peptide bond. The four most common structural elements: α-helix, β-strand, turns and coils. There are few proteins that contain other elements, which are so rare that they are not mentioned here[1,2].

- **Tertiary structure**

  The global conformation of a protein is called tertiary structure. It describes how the structural elements of the secondary structure are arranged in space and is determined by ionic interactions, hydrophobic interactions, hydrogen bonds and van-der-Waals bonds[2]. It should be mentioned that some proteins do not form a tertiary structure, but are still able to fulfil biological functions[1].

- **Quaternary structure**

  A single protein is formed by several polypeptide chains. The arrangement of the polypeptides in space is called the quaternary structure. It, too, is determined by ionic and hydrophobic interactions. The name of a protein with a quaternary structure depends on the number of polypeptide subunits(di-, tri-,tetra-,...) as well as if they are identical or not(homo/hetero). For example a protein made up of two identical polypeptides would be called a homodimer[1,2].

Figure 2.3 gives an illustration about the different structures of a protein and their interplay. The formation of protein structures is called folding. This folding process already starts when the protein is synthesised, because the structures are determined by the amino acid sequence only. So a disruption of the folding process can be caused by only one faulty amino acid and result in a complete loss of functionality[2].

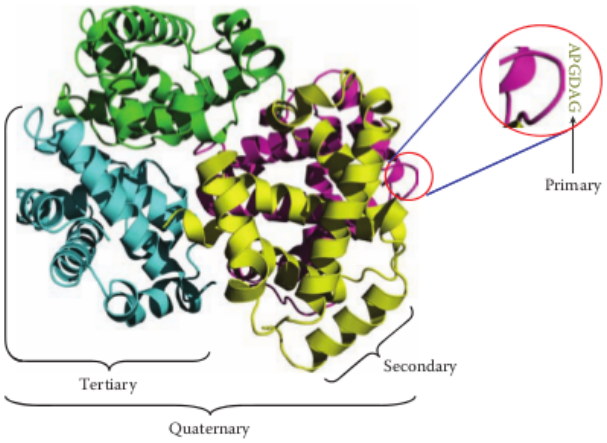

Figure 2.3.: Illustration of protein structures[1]

In order for a protein to function properly, the formation of secondary, tertiary, quaternary structures in addition to the primary structure is crucial. Since these structures are determined by very weak interactions, like hydrogen bonds, a change in the environment of the protein can lead to the loss of those structures, by breaking the involved bonds. Thus the protein would lose its biological function. This process is called denaturation[2]. Denaturation can be caused by heat, pressure, mechanical stress, salt, etc. . The increase in temperature increases the motion of molecules, which in turn can cause hydrogen bonds to break. So there exists a critical temperature at which denaturation suddenly occurs and is already finished at a temperature that is slightly higher than the critical temperature. For example the human body dies, if the core temperature is higher than 42°C, where key proteins lose their function[2]. Proteins can also be denaturated by adding denaturants, such as salt, to the environment of the protein. The denaturants remove water that is involved in the hydrogen bonds of the protein, causing it to denature. Salt can also act as an counter ion and so disturb ionic bonds in the protein structure, such a disruption can also be caused by a change in pH[2].

Elastin-like Peptide $(VPGVG)_n$

Elastin is an important and very interesting protein. Amongst other things it governs the stretching and recoil process of the lung, while breathing. It can undergo this cycle of expansion and recoil billions of times without failing and more importantly without breaking. This is crucial, because damaged Elastin can not be replaced [35]. Another interesting feature of Elastin is the so called Inverse Temperature Transition (ITT). When heating Elastin above a certain temperature it will change its conformation to a denser state before it undergoes denaturation [5,14,36,37]. This is contradictory to other proteins, which exhibit larger structures when the temperature is increased. The structural change occurring during the ITT is reversible, meaning, that cooling down the protein causes it to expand again. So the structural conformity of Elastin is not only influenced by breaking hydrogen bonds upon heating, but the ability to form new intra molecular hydrogen bonds by breaking hydrogen bonds to the hydration shell and vice versa. This feature is essential in order for Elastin to provide its biological function and is attributed to the (VPGVG) (Valin, Prolin, Glycin) amino acid sequence. There are many studies investigating peptides of $(VPGVG)_n$ with varying numbers of n. Nicolini et al. for example studied a peptide with $n = 1$ [5], while Urry et al. used $n = 251$ [36]. Zhao et al. found evidence that for $n > 4$ the found transition temperatures of the peptides can also be explained with a Lower Critical Solution Temperature. Under increasing temperature the peptide will lose hydrogen bonds to the water shell and increase the number of intramolecular hydrogenbonds. Above the LCST the peptide becomes unsolvable in water, resulting in a peptide rich and a peptide poor phase (this behaviour can also be found for PEG) [15], but for smaller peptide chains the expected LCST would be much higher then the reported transition temperatures found by Nicolini et al. and Ma et. al. [5,37]. Therefore it remains an open question, if there is a LCST for small peptide chains and why the critical temperatures for the LCST and ITT agree for large peptide chains and not for small peptide chains.

2.2 Microemulsions

Microemulsions are composed of three or more components. The three basic components of a microemulsion are a hydrophobic/non-polar, a hydrophilic/polar and an amphiphilic component. In the following the hydrophilic component is referred to as water, the hydrophobic component as oil and the amphiphilic component as surfactant. A surfactant molecule can be divided into two parts, the hydrophilic head and the hydrophobic tail. So the surfactant is able to form a layer between the hydrophilic and hydrophobic component. This causes microemulsions to be macroscopically isotropic, thermodynamically stable and to form nano structures, in contrast to regular emulsion, which are thermodynamically unstable. In addition to the three basic components other components, like co-surfactants, polymers etc., can be inserted into the microemulsion system as well [24].

2.2.1 Phase Diagram of Microemulsions

In order to completely characterise the composition of a microemulsion, there a two variables most commonly used [24]. First the mass fraction of the oil in the water-oil mixture:

$$\alpha = \frac{m_o}{m_o + m_w} \tag{2.24}$$

Second the mass fraction of the surfactant in the mixture of all three components:

$$\gamma = \frac{m_s}{m_s + m_o + m_w} \tag{2.25}$$

With these two parameters a Gibbs phase triangle can be constructed. This is shown in figure 2.4, where both parameters define one point in the triangle. As one can see compositions with a constant α would be represented by vertical lines, while compositions with a constant γ are represented by horizontal lines. The edges of the triangle stand for the pure components. The phase diagram shows three main regions, denoted by the numbers 1,2 and 3, indicating the number of phases in that region. In the one-phase region the system is in the microemulsion phase. While in the two-phase region there exists an excess phase of either pure oil or water in addition to the microemulsion phase. Lastly, in the three-phase region the two excess phases are simultaneously present in addition to the microemulsion phase [24]

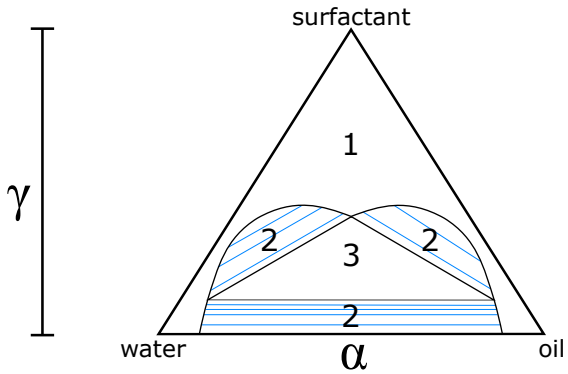

Figure 2.4.: Schematic of a Gibbs phase triangle of a tenary microemulsion. The numbers indicate regions with corresponding number of phases. Tie lines in the two-phase region, at which demixing occurs, are shown in colour.

The phases present in a microemulsion are not only determined by composition, but also influenced by temperature. In order to construct a phase-diagram for a constant water to oil ratio at all temperatures (constant α), one needs to obtain the phase triangles of the microemulsion at all temperatures. These triangles can then be stacked into a phase prism, which can be seen in figure 2.5 on the left side. By intersecting the phase prism at a constant α, one obtains the γ T phase diagram of the microemulsion (figure 2.5). Because of its unique form, the phase-diagram is called the fish plot. There are several points of interest in the phase-diagram, for example the mass fraction γ_0 of surfactant which is solubilised monomerically in water and oil, and the upper and lower temperature of the three phase body T_u and T_l. The minimal mass $\tilde{\gamma}$ needed to solubilise water and oil and the phase inversion temperature $\tilde{T}$, define the point at which the system is in its optimal state state [24].

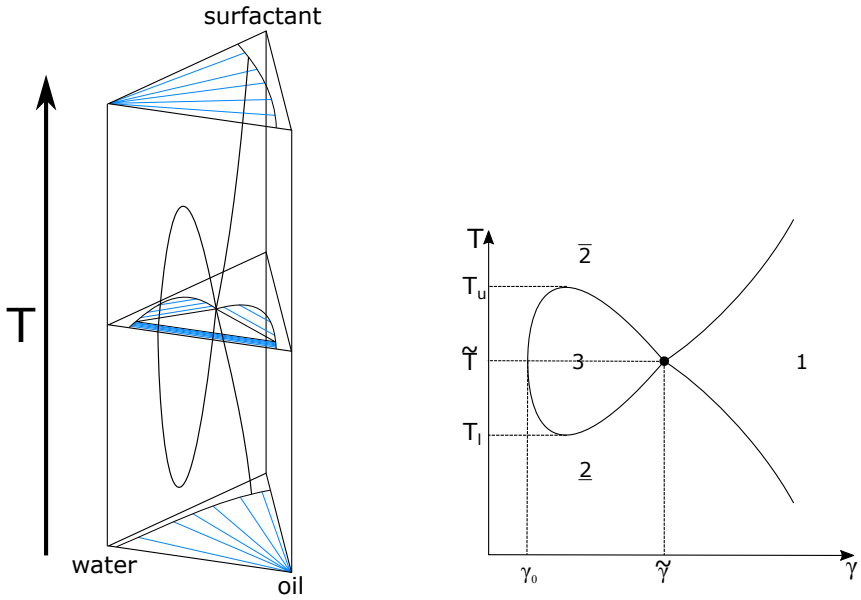

Figure 2.5.: Schematic of a phase prism and phase diagram of a microemulsion. An intersection through the phase prism yields the T γ phase-diagram. The fish plot contour separates the areas of different phases. The lines above or under the number 2 indicate, if an excess phase is under or above the microemulsion phase. The diagrams are derived from [24].

2.2.2 Structures in Microemulsions

Due to the amphiphilic character of the surfactant molecules, microemulsions are able to form micro structures. In order to determine the structure formed, it is helpful to first look at the structure formation inside a binary system, for example water/surfactant, before looking at the entire ternary system. Since the tail of the surfactant is hydrophobic, the head groups will try to "shield" the tails from water molecules, if the surfactant is dissolved in water. The structure resulting out of this self assembling of the surfactant molecules will have the lowest free energy out of all possible arrangements. By looking at the area occupied by the surfactant molecule, it is possible to determine this structure. Therefore we will assign the tail group of the surfactant a volume v and a full stretched critical

length l_c. Each head group is able to screen the area a_0. So, if there are N surfactant molecules in the water/surfactant mixture, the volume $V = N \cdot v$ would be occupied by the tail groups, while the area $A = N \cdot a_0$ would be screened by the head groups. The comparison between volume and surface already occurred in section 2.1.2, where a sphere was used to describe nucleation and the surfactant molecules should be able to form such a structure. So it will be discussed under what circumstances the surfactant molecules are able to arrange in a sphere. The radius of such a sphere would have to be $r = 3v/a_0$. This can be derived by simple geometry of a sphere with volume V and surface A. In a water/surfactant mixture the inside of such a sphere can only be occupied by tail groups of the surfactant molecules, thus the radius of the sphere must not exceed the critical length l_c. This yields a condition under which the formation of a sphere is possible. Defining a packing parameter $p = v/l_c a_0$, one can calculate that for $p \leq 1/3$ a spherical micelle is formed. If p is larger than 1/3 the surfactant molecules will form cylinder shaped micelles or even bi-layer structures, such as vesicles or lamellae [26]. This very simple approach did not take oil as the third component into consideration. The hydrophobic nature of oil allows for the formation of spheres, even if $p > 1/3$, since it can be inside of the sphere and cause a swelling of the micelle. Thus increasing the likelihood of the formation of spherical structures. The description of this situation is much more complex and requires a look at the spontaneous curvature c_0 of the surfactant. The radius of a spherical micelle that results in the lowest free energy is given by $r = 1/c_0$ [38]. If the micelle is not able to reach the desired spontaneous curvature, it will be deformed. The deformation will cause the free energy f to increase and results in two radii of curvature. The energy can then be written as: [38]

$$f = \frac{1}{2}\kappa_c \left(\frac{\partial n_x}{\partial x} + \frac{\partial n_y}{\partial y} - c_0 \right)^2 + \overline{\kappa_c} \left(\frac{\partial n_x}{\partial x}\frac{\partial n_y}{\partial y} - \frac{\partial n_x}{\partial y}\frac{\partial n_y}{\partial x} \right) \tag{2.26}$$

Here $\vec{n}$ is a local normal on the layer, while κ_c and $\overline{\kappa_c}$ are the bending moduli of the surfactant layer, giving the flexibility of the surfactant shell. The increase in f must be small in order for the deformed micelle to be stable. If the increase is too large the microemulsion will form other non-spherical micelles or decompose.

The Surfactant AOT

In this work AOT(Sodium 1,4-bis(2-ethyhexoxy)-1,4-dioxobutane2-sulfonate) is used as the surfactant. Figure 2.6 shows the chemical structure of AOT. The hydrophobic tail consists out of two hydrocarbon tails, while the hydrophilic head group contains Na^+ cations and SO_3^- anions. When used in a microemulsion the sodium ion will dissociate into the polar component (water), leaving only the SO_3^- anions connected to the head, making AOT an anionic surfactant. The figure also illustrates the cone shape of the AOT molecule.

Due to this cone shape, a microemulsion containing water/AOT/alkane will favour the inclusion of water domains in an oil matrix. Early experiments on such ternary systems were done by Eicke et al. and Kotlarchyk et al. [39–43] and revealed a very large one phase region in the phase triangle as well as the structure of water droplets surrounded by an AOT shell that are dissolved in an oil matrix.

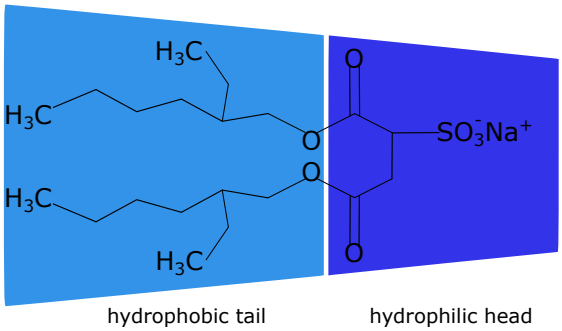

Figure 2.6.: Chemical structure of the AOT surfatant molecule

Microemulsions in the mentioned droplet phase can be characterised by the already introduced parameters α, γ, but another set of parameters can be defined, which is very useful describing microemulsions in the droplet phase. First the ratio of water molecules to surfactant molecules is described by the parameter w. Second the volume fraction ϕ of the droplets is used:

$$w = \frac{n_w}{n_s} \qquad \phi = \frac{V_w + V_s}{V_w + V_s + V_o} \tag{2.27}$$

In the previous section it was discussed, that n_s moles of surfactant are able to cover a surface of $A = n_s \cdot N_A \cdot a_0$ and n_w moles of water have a volume of $V = n_w \cdot \nu_w \cdot N_A$, where ν_w is the volume of one water molecule. Since we are in the droplet phase, we can assume a spherical structure, which allows us to express w:

$$w = \frac{n_w}{n_s} = \frac{4\pi r^3 a_0 N_A}{12\pi r^2 \nu_w N_A} = \frac{a_0}{3\nu_w} r \tag{2.28}$$

So the parameter w is directly proportional to the radius of the spherical droplet, allowing for an approximation of the size of the confinement and the determination of a_0 via experiments. This enables a characterisation of the surfactant.

Studying soft confinement effects on molecules and vice versa there are two main challenges. The first challenge is to bring the molecule into the confinement and the second is to insure that the confinement is not destroyed by the molecule. For the water-in-oil droplet phase, there are interesting types of molecules that can be inserted into the droplet. For example an amphiphilic molecule, like a block copolymer. They have been found to act as a co-surfactant and enhance the surfactant performance ("boosting effect") [44,45]. Another type of molecule would be a hydrophilic one, such as an ELP or the

homopolymer PEG. It was found that PEG can be inserted into the water core and attaches to the surfactant layer[18,46]. The influence of PEG on the droplet phase of water-in-oil microemulsions has been studied extensively since the 1990s[18,23,47] and is still subject of current experiments[20,48]. Many different droplet sizes, droplet concentrations, polymer chain lengths and polymer concentrations were studied. It was found that PEG increases the lower phase boundary as well as the upper phase boundary of the one phase region. Further the droplet phase remains stable under the addition of the polymer, but it increases the tendency of the droplets to form clusters.

Determination of Structural Changes of the Droplet Phase

In this work Small Angle X-ray Scattering (SAXS) experiments are used to determine structural properties of water/AOT/octane microemulsions in the droplet phase. SAXS measurements can show, whether the microemulsion is in the droplet phase and give information about key parameters of that phase, like the average droplet radius. The details of SAXS and scattering experiments in general will be outlined in chapter 3.4.

Since X-rays scatter on the electron shell of the sample, it is obvious that the three components of the microemulsion need to have significantly different electron densities ρ in order for X-ray scattering experiments to yield explorable results. Figure 2.7 shows the scattering situation for water/AOT/octane microemulsions. The large AOT molecule is again divided into its head and tail group. The tail group has the same scattering length density for X-rays as the octane matrix, due to its composition, while the head group has a much higher scattering length density than the matrix or the water. This difference allows for the scattering at the surfactant shell of the microemulsion droplet.

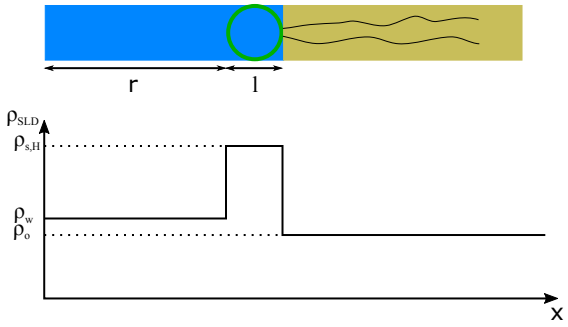

Figure 2.7.: Schematic sketch of the Xray scattering length density distribution in a water/AOT/octance microemulsion droplet. The values in the graph are not absolute, but represent that there is a large contrast between water core and AOT head group.

With the help of the scattering length density distribution outlined in figure 2.7 the "form factor F($\vec{q}$)" can be calculated:[49]

$$\begin{aligned} F(q,r,l) =& 4\pi r^3(\rho_w-\rho_{s,H})\frac{\sin qr - qr\cos qr}{q^3r^3} \\ &+ 4\pi(r+l)^3(\rho_{s,H}-\rho_o)\frac{\sin q(r+l)-q(r+l)\cos q(r+l)}{q^3(r+l)^3} \end{aligned} \tag{2.29}$$

Due to the spherical symmetry of the investigated system, the vector properties of $\vec{q}$ can be omitted. Here ρ_w, $\rho_{s,H}$ and ρ_o are the scattering length densities of water, the AOT head group and octane, respectively. The radius of the water core is given by r and l

gives the thickness of the AOT head group shell. By taking the square of the form factor in equation 2.29, the scattered intensity can be calculated. However this only holds true, if the microemulsion droplets are far apart and the scattering from different droplets does not interfere coherently. But as soon as the the droplet concentration becomes too large or cluster processes begin to occur, the form factor has to be multiplied by a "structure factor S(q)", taking those effects into account.

Since the calculation of a structure factor for microemulsion droplets is quite complicated, it might be interesting to find simpler models, that describe microemulsions as well sufficiently. In this case the structure factor of hard spheres with radius r_{HS} is sufficient, even though it is not entirely the case. Hard spheres don't interact, if their centres are $2r_{HS}$ or further apart, but have an infinite interaction potential below this critical distance. So the radius of the hard sphere r_{HS} gives important information about the size of the microemulsion droplet. Ashcroft et al. calculated the structure factor for hard spheres: [50]:

$$S_{HS}(q) = \frac{1}{1 + 24\eta \dfrac{c(q, 2r_{HS})}{4qr_{HS}}} \tag{2.30}$$

Here once again the vector properties are omitted due to the spherical symmetry and η is the hard sphere volume fraction (not necessarily equal to ϕ). The function $c(q, 2r_{HS})$ is periodic and related to the pair distribution function of hard spheres.

It should be noted that the hard sphere structure cannot describe the microemulsion droplets, if they start clustering. In this case the structure factor needs to be replaced by one that does not use the radius of the hard spheres, but instead looks at a correlation length, which describes the average size of a droplet cluster [42]. A microemulsion in the droplet phase can also exhibit both of the mentioned structure factors at once. Describing the situation of large droplet clusters paired with a still high proportion of freely diffusing single droplets [19].

Up until now it was assumed that all droplets are monodisperse and have the same radius r or r_{HS}, although there are of course some variations in the radii of different droplets. As the droplets diffuse through the oil matrix they will eventually collide with other droplets and thus exchange material. In addition the droplets exhibit internal shape fluctuations [21,51–53]. So it is necessary to introduce a function that takes this polydispersity into account and to convolute it with the hard sphere structure and core shell form factor in order to average it. Here it is assumed that the shell thickness will not fluctuate, while the water core radius can show polydispersity. The function used in this work will be the Schulz-Zimm distribution function, which is centred around a average radius r_{avg} with a relative polydispersity σ [43,54,55]

$$f(r) = \left(\frac{1}{\sigma^2}\right)^{\frac{1}{\sigma^2}} \left(\frac{r}{r_{\mathrm{avg}}}\right)^{\frac{1}{\sigma^2}-1} \frac{e^{-\dfrac{r}{r_{\mathrm{avg}}\sigma^2}}}{r_{\mathrm{avg}}\Gamma\left(\dfrac{1}{\sigma^2}\right)} \tag{2.31}$$

The influence of this distribution on the core-shell form factor can be seen in figure 2.8. Where the core-shell form factor for a system with a(n) (average) core radius of $r = 40\,\text{Å}$,

a shell thickness of 10 Å, a core scattering length density of 1×10^{-6} Å^{-2}, a shell scattering length density of 2×10^{-6} Å^{-2}, a solvent scattering length density of 3×10^{-6} Å^{-2} and a polydispersity of $\sigma = 0$ respectively $\sigma = 0.15$.

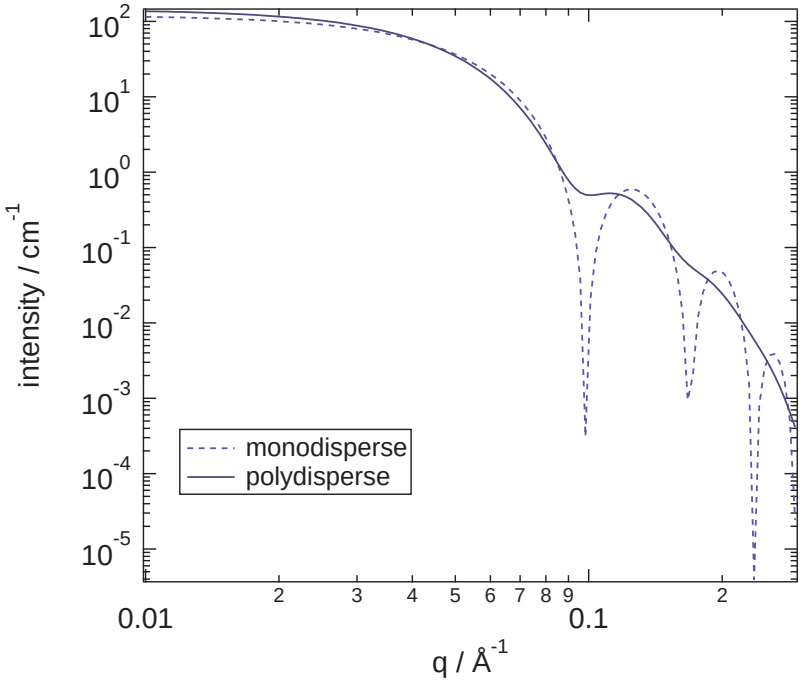

Figure 2.8.: Display of the influence of the Schultz-Zimm distribution on the core-shell form factor.

So with the help of SAXS the average radius of a microemulsion droplet can be measured, as well as the polydispersity of the radius distribution and it yields information about the overall structure of the microemulsion, namely if clusters and free single droplets coexist or not. The same insights can be gained by neutron scattering, because only the scattering length density distribution changes and can be influenced by an according deuteration scheme.

2.2.3 Microemulsion Dynamics

The final aspect of this chapter will focus on the dynamics in microemulsions. There are a variety of different dynamics that occur in a microemulsion, ranging over a timescale from pico seconds to micro seconds [56]. Hereby the reorientation of "free" water molecules in the droplet core is the fastest observable process, with a relaxation time around 10 pico seconds at room temperature [3]. The amount of free water found in a microemulsion is limited, because of the confinement and thus the reorientation of confined water can be observed as well. Confined water exhibits a slower relaxation time than free water [57]. The alkane molecules of the matrix reorientate on a timescale that is one magnitude slower than water, since they are larger in size [58].

Microemulsion droplets show three distinct dynamical processes in addition to the already discussed single molecule processes. The fastest of these three are the already men-

tioned shape fluctuations of the surfactant shell and they take place on the nano second time scale [59]. The second fastest dynamical process is droplet diffusion, translational as well as rotational. Diffusion happens on a timescale of hundreds of nano seconds [21,60,61]. Lastly the slowest process that can be observed are droplet collisions and the following exchange of material, leading to the so called "percolation" of a microemulsion in the droplet phase. The timescale of this process is the micro second range [20,56]. Still it should be mentioned that without droplet diffusion there would be no droplet collisions, the timescale references the frequency of collisions. This work will only deal with the phenomenon of percolation, for which a short introduction will be given in the following

Percolation in Water-in-Oil Microemulsions

Static percolation is a random and very important process that can be found when studying oil in rock formations or forest fires [27]. In order to theoretically analyse percolation, a cubic lattice with infinite proportions is observed. Every site of the lattice is occupied by a particle with the probability p. This simplified model is very far from the dynamical percolation process in a microemulsion, but will be considered to derive fundamental basics of percolation theory [27,62].

There exists a threshold probability p_c at which the lattice is criss crossed by an infinite cluster of particles from one side to the other. In the case described above this probability can be calculated to $p_c = 0.3116$. So for all probabilities $p > p_c$ an infinite cluster reaching through the lattice will form. For $p < p_c$ it is interesting to study how many different particle clusters arise and how large they are on average, before they form the infinite cluster at $p = p_c$. In order to do so the correlation length ξ is introduced. It gives the average distance between two occupied lattice points belonging to the same cluster. For $p \to p_c$ the correlation length will diverge, since the cluster becomes infinitely large at $p = p_c$. This divergence can be characterised by a power law, with the exponent ν that can be evaluated to $\nu \approx 0.9$ [27].

$$\xi \propto |p - p_c|^{-\nu} \tag{2.32}$$

By assigning empty lattice points a finite conductivity and occupied lattice points an infinite conductivity, the considered model can be turned into a system with a physical property. So for $p > p_c$ the lattice will show an infinite conductivity, while for $p = 0$ the lattice will have the same conductivity as an empty lattice point. The more interesting case is now the conductivity of the lattice for $0 < p \to p_c$, which can be also described by a power law with the exponent s [27]

$$\sigma \propto |p_c - p|^{-s} \qquad p < p_c \tag{2.33}$$

Changing the set up above to one, where empty lattice points have a conductivity of zero and occupied ones have a finite conductivity, the lattice will show no conductivity for $p < p_c$. At $p = p_c$ a conductivity will now arise and continue to increase for $p > p_c$. Once again this can be described by a power law with the exponent μ [27]

$$\sigma \propto |p - p_c|^{-\mu} \qquad p > p_c \tag{2.34}$$

This set up now shows a certain similarity to a microemulsion system. The oil matrix has a basically non existing conductivity, whereas the droplets exhibit a rather high conductivity, since there are composed of water containing dissolved sodium ions of the AOT surfactant. Assuming that the droplets would be static and not diffuse through the matrix, the percolation threshold would be $\phi = p_c = 0.3116$, as already discussed. But since the droplets do show diffusion and are dynamic we need to look at dynamic percolation instead of static percolation [62].

To be able to describe the dynamic percolation in microemulsions, the introduced model needs to be expanded, allowing lattice sites to perform a random walk movement around the lattice. Further two jump rates Γ_1 and Γ_2 are introduced. Γ_1 gives the timescale on which the droplets (occupied lattice sites) jump along the lattice, while Γ_2 sets the jump rate of single charge carriers. The charge carriers will move from one occupied lattice site to a neighbouring occupied one, simulating the exchange of ions between the droplets. The overall dynamics of the charge carriers, which move from droplet to droplet but also move within the droplets, is found to be only dependent on the ratio of the two jump rates $\gamma = \frac{\Gamma_1}{\Gamma_2}$. Within this model the conductivity can be calculated again, yielding the same results already found in equation 2.33 and 2.34, with a change of the exponent in the power law for $p < p_c$ [63].

In spite of a large difference between static percolation and the microemulsion system, the conductivity shows the same behaviour around p_c for both systems. A key difference though is that in a water/AOT/octane microemulsion system, percolation cannot only be achieved by increasing the concentration ϕ (or p), but also by increasing the temperature T of the system [20]. This is a consequence of the already discussed tendency of the droplets to form clusters at higher temperatures [62,64]. This leads to a percolation temperature T_p rather than a percolation threshold p_c. So the percolation phenomenon in microemulsions can be studied dependent on concentration at one temperature or dependent on temperature at one concentration. In this work the latter case will be investigated.

Finally the bending modulus introduced in equation 2.26 is considered. The percolation in microemulsions depends on the ability of charge carriers to move from one droplet to another. An important factor in this mechanism are the kinetics of droplet collisions, which depend on the deformability of and thus on the bending modulus of the surfactant shell. Refining considerations about membrane fluctuations of De Gennes and Taupin, Gompper and Kroll introduced a temperature dependent persistence length [65,66]. This persistence length is equal to the radius of the microemulsion droplet at the percolation threshold [18] and thus the percolation temperature can be related to the core radius of the droplet via the bending modulus [18,62,65,66]

$$T_p = \frac{4\pi\kappa}{k_B} \frac{1}{\ln r_c/a} \tag{2.35}$$

With the Boltzmann constant k_B and a as the shortest undulation of the membrane, which is comparable to the size of the AOT head groups in this work.

So by measuring the conductivity of a water/AOT/octane microemulsion in the droplet phase for different temperatures with dielectric spectroscopy, the percolation temperature T_p of the system can be found [20]. Allowing for the observation of percolation phenomena

and even the calculation of the bending modulus of the surfactant shell, by combining the results from dielectric spectroscopy with structural results (droplet radii) obtained via SAXS measurements.

It should be noted that this entire section just considered a pure microemulsion without any additives. The influence of different co-surfactants, polymers or other additives on the percolation in water/AOT/octane microemulsion is very difficult to predict. In this work the influence of PEG on the bending modulus and the percolation temperature will be studied.

3 Experimental Methods and Primary Data Evaluation

The following chapter will introduce the experimental methods used for studies in this work. Additionally the primary data evaluation will be explained. Before any experiment can take place, samples must be prepared, which in this case mostly consisted of mixing appropriate amounts of the single components together. A detailed description of the preparation method and the components used will be given in 3.1. In order to obtain phase transition temperatures, Differential Scanning Calorimetry (DSC) is deployed. Briefly speaking, it allows the measurement of endothermic/exothermic processes when heating or cooling a sample. A more detailed introduction of this method will be given in section 3.2. As already mentioned, it is possible to obtain percolation temperatures of microemulsions via Broadband Dielectric Spectroscopy (BDS). BDS measures the impedance of a sample and so can give information about the orientation of electric dipoles inside an external electric field. This method will be further explained in section 3.3. Finally section 3.4 will introduce the general principles of static scattering experiments. This section will deal with X-ray as well as neutron scattering. Further it will outline small angle and wide angle scattering techniques.

3.1 Sample Preparation

In the following preparation of the binary mixtures and microemulsions studied in this work will be described. Since this study also uses neutron scattering information on the deuterated materials will be given. Further the production of a buffer solution for the ELP will be explained. All samples were prepared using a microbalance with an accuracy of 50 μg. The hygroscopic components of the samples, like the polymer PEG and the surfactant AOT were held in a vacuum oven at 45°C and 10 mbar for at least 24 hours before sample preparation in order to "dry", removing possibly adsorbed water from them.

3.1.1 Preparing Binary Mixtures

This study uses two different types of PEG. One has -OH groups at both ends of the chain, while the other is capped with -OCH_3 groups. The first type will be referred to as PEG, since it is the standard and the second type will be abbreviated as PEGDME, with DME meaning dimethyl ether, referring to the two -OCH_3 endgroups. For binary mixtures of PEG/PEGDME and water, the polymer was dried as explained above and then put into a vial. Then the desired amount of water was added in order to create mixtures with different weight percentages ($wt\% = \frac{m_{polymer}}{m_{polymer} + m_{H_2O}}$) of PEG/PEGDME. Samples in this study contained 5, 10, 20, 30, 40, 50, 60, 70, 80, 90, 95 (wt%) PEG with a molecular weight of 1500 g/mol or PEGDME with a molecular weight of 1650 g/mol.

- H_2O was provided by a DirectQ3 system (Millipore)
- Polyethylene glycol 1500 was purchased from *Alfa Aesar*
- Polyethylene glycol dimethyl ether 1650 was purchased from *polymersource*

The other binary mixture studied in this work was an ELP dissolved in a deuterated buffer solution in order to be studied with neutron scattering. The ELP used was $GVG(VPGVG)_3$ and it was specially synthesised by Susann Weißheit under the supervision of Christina Thiele of the AK Thiele of TU Darmstadt, Germany[67]. The buffer solution was prepared using the Henderson-Hasselbach equation:[1].

$$pH = pK_a + \log\frac{[R]^-}{[RH]} \tag{3.1}$$

Where pH is the desired environment. pK_a is the dissociation constant and [RH] is the molar concentration of the used acid, while $[R]^-$ is the concentration of the conjugated base. The buffer used in this work is a deuterated 50 mM (milli molar) phosphate buffer. So sodium dideuterium phosphate (D_2NaO_4P) is the acid and disodium deuterium phosphate (DNa_2O_4P) its conjugated base with the dissociation constant $pK_a = 7.7804$[68]. The buffer should stay at a neutral $pH = 7.43$ for deuterated water and therefore equation 3.1 becomes:

$$7.43 = 7.7804 + \log\frac{[R]^-}{[RH]} \tag{3.2}$$

with the intention of a 50 mM phosphate buffer the molar concentration of the acid and the base can be related:

$$[RH] + [R]^- = 0.05 \tag{3.3}$$

With this it is possible to calculate the amount of D_2NaO_4P and DNa_2O_4P that needs to be added to deuterated water in order to produce the desired buffer. Since the values calculated from this equation are theoretical and the weighed in masses may differ from the ones calculated, deuterated hydro chloric acid (DCL) and deuterated sodium hydroxide (NaOD) is used to tune the buffer to the desried $pH = 7.43$ value after the phosphate acid and base are added. The pH values were determined with the "HI 9811-5 pH- Meter" from "HANNA instruments". Due to the small molar concentration of the phosphate in the buffer, 99% of the buffer are made up by deuterated water. Then the buffer was added to the ELP producing mixtures with 5.4, 10.1, 14.5 and 18.4 wt% of ELP (These wt% are calculated by calculating the wt% of ELP in a microemulsion droplet with $w = 15$ containing one, two, three and four peptide chains).

- D_2NaO_4P and DNa_2O_4P were purchased from *CDN ISOTOPES*
- D_2O was purchased from *Sigma Aldrich* with a purity of 99%
- DCl was purchased from *deutero* 36-38% in D_2O with 99.5% purity
- NaOD was purchased from *deutero* 40% in D_2O with 99.5% purity

3.1.2 Preparing Microemulsion Samples

Microemulsion without additive polymer or ELP were prepared by first weighing in the amount of AOT and then calculating the amount of water/buffer and octane necessary to produce the desired w and ϕ. Therefore the molar weight and the densities of all components have to be known. Then the water/buffer is added to the AOT and then the octane as the last component. Due to the high precision of the microbalance the estimated uncertainty of w and ϕ is below 1%. The preparation of microemulsions containing polymer/ELP is the same, except that before the water/buffer is added to the surfactant the desired amount of polymer/ELP is added. Here we introduce a new parameter Z, which gives the average number of polymer chains/peptide chains per droplet of the microemulsion. In order to calculate the amount of polymer/ELP that needs to be added, the radius of the water core r_c has to be estimated. Here the relation $r_c = 1.4 \cdot w$ [41,69] is used for that estimation. Because of this estimation and the very low weight of polymer/ELP that needs to be added to the microemulsion the uncertainty of Z is larger than that of w and ϕ and estimated to be around 10%. In this study PEG with the molecular weights of 200, 400, 600, 1500, 4000, 6000, 12000 g/mol were added to non deuterated microemulsions as well as PEGDME with 270, 1650 and 13000 g/mol molecular weight.

- All polyethylene glycols were purchased from *Alfa Aesar*
- All polyethylene glycol dimethyl ethers were purchased from *polymersource*
- Octane was purchased from *ACROS ORGANICS* with a purity above 99%

The ELP was added to microemulsions where all other components were deuterated. Since deuterated AOT can not be purchased it was specially synthesised by Sebastian Schöttner under the supervision of Markus Gallei from the Ernst-Berl-Institut für Makromolekulare Chemie in Darmstadt, Germany. Synthesis was done according to Trickett et al. [70] and proven to have worked in synthesising deuterated AOT [22].

- Deuterated octane was purchased from deutero with a purity of 99%

3.2 Differential Scanning Calorimetry

Differential Scanning Calorimetry (DSC) is a powerful thermal analysis technique. It measures the amount of heat needed to change the temperature of a sample and compares it to the heat flow of a reference kept at the same temperature, allowing to determine, if the sample needed more or less heat than the reference due to a chemical reaction, its heat capacity or physical phase transition. There are two types of calorimeters mainly used for studying thermal properties of a sample, heat-flux and power compensated calorimeters [71]. Since in this work a DSC of the second type is operated, the theory of power compensated DSC measurements will be explained in the following.

In a power compensated DSC there are two holders, the sample holder and the reference holder. Both of the holders are fed power to increase/decrease the temperature of the holder. A power compensated DSC now measures the differential electric power $p_s - p_r$ required to keep the sample holder and the reference holder at the same temperature, during an experiment. Here p_s is the power fed to the sample holder and p_r

the power fed to the reference holder[71]. For the following discussion the term "sample holder" refers to the sample and the holder taken into account together. Applying the first law of thermodynamics to the sample holder yields:[71]

$$\frac{dH}{dt} = \frac{dQ}{dt} + \frac{dW}{dt} \tag{3.4}$$

with H the enthalpy of the sample holder, Q the heat transferred to the sample holder and W the electrical work done on the sample holder. Considering every term in equation 3.4 starting with the first one. The enthalpy H depends on the extent of the chemical reaction or phase transition ξ and the temperature T, it can be written as:[71]

$$\frac{dH}{dt} = \frac{\partial H}{\partial \xi}\frac{d\xi}{dt} + \frac{\partial H}{\partial T}\frac{dT}{dt} + v(t) + C\frac{dT}{dt} \tag{3.5}$$

Here $v(t)$ is the rate of enthalpy change of a physical phase change or chemical reaction of the sample, while C yields the heat capacity of the sample holder. Further analysing equation 3.4 one can write the heat flow rate dQ/dt as:[71]

$$\frac{dQ}{dt} = h(T_E - T) \tag{3.6}$$

With the heat transfer coefficient h and the temperature of the environment T_E, which surrounds the sample holder. The sample will thermally change, which is compensated by the electric power $P(t) = dW/dt$. It can be expressed as:[71]

$$\frac{dW}{dt} = K(T_p - T) \qquad T_p > T \tag{3.7}$$

$$= 0 \qquad T_p < T \tag{3.8}$$

With a constant K and the programmed temperature T_p. The second definition is a consequence of the fact that the electrical power always is positive. So in the case that $T_p < T$, the temperature T of the sample holder will approach T_p, because energy will be transferred into the environment with $h(T_E - T)$. Combining the above equations results in:[71]

$$v(t) + C\frac{dT}{dt} = h(T_E - T) + P(t) \tag{3.9}$$

In this study the programmed temperature will change linearly with time t at a given rate α:

$$T_p = T_{p,0} + \alpha t \tag{3.10}$$

If no physical or chemical change of the sample takes place, the sample is in a steady state and thus the sample holder temperature will change linearly with time at the rate α, just as the programmed temperature will. So equation 3.9 will become:[71]

$$C\frac{dT_{ss}}{dt} = h(T_E - T_{ss}) + P_{ss}(t) \tag{3.11}$$

The subscript "ss" denotes the steady state. By subtracting this equation from equation 3.9 the following equation is derived: [71]

$$v(t) + C\frac{d\theta}{dt} = -h\theta + p(t) \tag{3.12}$$

With

$$\theta = T - T_{ss} \tag{3.13}$$

and

$$p(t) = -K\theta = P(t) - P_{ss}(t) \tag{3.14}$$

Using the last definition in order to eliminate θ from equation 3.12 yields:

$$v(t) = \frac{C}{K}\frac{dp(t)}{dt} + \frac{h+K}{K}p(t) \tag{3.15}$$

This equation states that $p(t)$ gets recorded as a function of time t and due to a change in the enthalpy $v(t)$ of the sample the recorded curve will deviate from the zero line in the form of a step or peak. One can also read $v(t)$ as the input signal of the DSC system, while $p(t)$ becomes the output signal of the calorimeter. Ideally the output signal $p(t)$ follows exactly the input signal $v(t)$.

By integrating $v(t)$ over time t the overall change in enthalpy can be calculated, assuming that the integral converges and $p(0) = p(\infty) = 0$: [71]

$$\Delta H = \int_0^\infty v(t)dt = \frac{h+K}{K}\int_0^\infty p(t)dt \tag{3.16}$$

One can see that $\int_0^\infty p(t)dt$ is the area under a peak in a curve that records $p(t)$ over time. Equation 3.16 shows that the enthalpy change of the sample holder is proportional to the peak area of the output signal, but not exactly equal to it. Therefore calibration measurements are necessary in order to determine the exact value of the enthalpy change.

So far $p(t)$ was recorded over time in order to determine the enthalpy of an eventual physical phase transition, but in order to observe the "Onset temperature" of that transition, $p(t)$ is recorded over the temperature T_s of the sample holder. A physical phase transition will also show a peak in this presentation. The onset temperature of the transitions is then determined by fitting a line throughout the first flank of the peak and taking its intersection with the hypothetical baseline. In order to determine the correct Onset temperature a calibration with known standards is required and can be combined with the calibration for enthalpy values.

The Perkin Elmer DSC8000

DSC measurements in this work were performed using a *Perkin Elmer DSC8000* combined with a *CLN2 Cooling Accessories*. The cooling block temperature was set to -135°C in order to observe a temperature range from -80 °C to 100 °C. Cyclohexan (Onset temperature: 6.54 °C and Melting Enthalpy: 32.25 J/g) and Dodecane (Onset temperature: -9.63 °C and Melting Enthalpy: 216.73 J/g) were used as calibration standards for temperature and enthalpy calibration with a heating rate of 2 K/min. These values were taken from the software *Pyris* provided by *Perkin Elmer*. The software does not yield the values for h and K in equation 3.16. The samples are inserted into *Auto sampler Aluminum Sample Pans* with a volume of 40 μL and a thickness of 0.15 mm. Samples weighed between $\approx$ 1 - 10 mg and were inserted into the sample pans via a syringe. Then the pans are hermetically sealed using the proper press from *Perkin Elmer*. Sample holder and reference holder are covered with the special *Auto sampler lids*.

3.3 Broadband Dielectric Spectroscopy

Dielectric spectroscopy measures the dielectric response in polarisation $\vec{P}$ of a system to an external electric field $\vec{E}$. Due to the spectrometers available, dynamical processes on a timescale from pico seconds to several days can be observed. By applying an external electric field, a polarisation is induced into the system [72]

$$\vec{P} = \epsilon_0 \chi \vec{E} \tag{3.17}$$

With χ the dielectric susceptibility and ϵ_0 the vacuum permittivity. The polarisation is made up out of all microscopic dipole moments $\vec{p}$ in the sample $\vec{P} = \frac{1}{V}\sum \vec{p}$. These dipole moments can come from shifted electron clouds, permanent dipoles, which are oriented or stretched, or separated ionic charges dipoles. The simple relationship in equation 3.17 only holds true for homogeneous, isotropic and linear mediums, otherwise terms need to be added taking the non-linearity and/or anisotropy of the system into account. In that case χ is no longer a scalar, but becomes a second order tensor. Since microemulsions are considered to be isotropic the vector properties can again be omitted and no non-linear terms need to be added. Using the relationship between the dielectric permittivity ϵ and χ, $\epsilon = 1 + \chi$, the polarisation can be written as [72]

$$P = \epsilon_0(\epsilon - 1)E \tag{3.18}$$

The orientation of dipole moments in an external electric field will take time. So it is of high interest to not only study the magnitude of the induced polarisation, but also its time dependence, which can give information about the dynamics in a system when an external time dependent electric field is applied. For electric fields that are weaker than the internal fields of the sample, linear response theory can be applied and the time dependent polarisation can be calculated to [72,73]

$$P(t) = P_\infty + \epsilon_0 \int_{-\infty}^{t} \epsilon(t - t') \frac{dE(t')}{dt'} dt' \tag{3.19}$$

Here P_∞ is the spontaneous polarisation that includes all polarisation effects that are faster than the observable time scale of the experiment. So it can be seen that all the information about system dynamics is contained in $\epsilon(t)$. As already mentioned the dynamics of a system can be very slow (several days) or very fast (pico seconds), resulting in very long or very short observation times, thus it is more convenient to change from the time domain into the frequency domain by Fourier transformation [72,73].

$$\hat{P}(\omega) = \epsilon_0(\hat{\epsilon}(\omega) - 1)\hat{E}(\omega) \tag{3.20}$$

Since Fourier transformation was used, the quantities in the equation are complex numbers, denoted by the $\hat{}$ above them. Further the time dependent dielectric function $\epsilon(t)$ can be related to the frequency dependent dielectric function via Laplace transformation [72,73]

$$\hat{\epsilon}(\omega) = \epsilon_\infty - \int_0^\infty \frac{d\epsilon(t)}{dt} e^{-i\omega t} dt \tag{3.21}$$

Where ϵ_∞ is the value of the dielectric function at infinite high frequencies. Since the frequency dependent dielectric function is a complex quantity, it can be divided into its real and imaginary part

$$\hat{\epsilon}(\omega) = \epsilon'(\omega) - i \cdot \epsilon''(\omega) \tag{3.22}$$

The negative sign is used due to the convention, because the fluctuation-dissipation theorem makes $\epsilon'(\omega)$ the energy stored reversibly in the system, while $\epsilon''(\omega)$ the energy dissipated. The real part and the imaginary part of the complex dielectric function are related to each other by the Kramers-Kronig relation [72,73]

$$\epsilon'(\omega) - \epsilon_\infty = \frac{1}{\pi} \oint \frac{\epsilon''(\xi)}{\xi - \omega} d\xi \qquad \epsilon''(\omega) = -\frac{1}{\pi} \oint \frac{\epsilon'(\xi) - \epsilon_\infty}{\xi - \omega} d\xi \tag{3.23}$$

With this relation it becomes clear, that either $\epsilon'(\omega)$ or $\epsilon''(\omega)$ contains the entire information about the dielectric properties of the sample.

In this work percolation of microemulsions is measured by the increase in conductivity [20]. Thus the dielectric function is of high interest, because it can be related to the frequency dependent conductivity of the microemulsion [72]

$$\hat{\sigma}(\omega) = i\omega\epsilon_0\hat{\epsilon}(\omega) \tag{3.24}$$

Due to the complex number i in this equation, the DC conductivity can be calculated from the imaginary part of the dielectric function.

The experimental set-up used to study a sample depends highly on the desired frequency range. Frequencies below 1 MHz can be investigated using a frequency-response analyser. This range is usually referred to as the low frequency range. The high frequency range, above 1 MHz up to several GHz, can be studied using impedance analysers, which measure the reflection of electromagnetic waves of the sample positioned at the end of a coax line [72]. This is necessary, because at such high frequencies the impedance of the measurement cables starts to critical influence the result of the experiments.

Novocontrol Alpha Analyzer

For this work all dielectric measurements are carried out using a *Novocontrol Alpha-N High Resolution Dielectric Analyzer*, covering the frequency range of 1 Hz to 10 MHz. The frequency of the analyser has an uncertainty of 10^{-4}. The temperature was controlled by *Quatro Cryosystem*, which is commercially available, allowing a reproducible temperature accuracy better than 0.5 K[20]. Voltage applied was sinusoidal and had an amplitude of 0.3 V. In order to calculate the impedance of the sample the complex voltage $\hat{u}$ and the complex current $\hat{i}$ are measured over frequency[72]

$$\hat{Z}(\omega) = \frac{\hat{u}(\omega)}{\hat{i}(\omega)} = \frac{1}{i\omega\hat{\epsilon}(\omega)C_0} = \frac{1}{\hat{\sigma}(\omega)C_0} \tag{3.25}$$

C_0 is the capacity of the empty sample cell and needs to be determined in order for the dielectric function or conductivity to be calculated. Impedances measured by this set up have an uncertainty of about 0.1%. The sample cell used in this work was developed by Wagner and Richert and has the geometry of a plate capacitor. Since the octane in the microemulsion would evaporate during the measurement, the sample volume is sealed with two O-rings, preventing evaporation from happening[20,74]. The sample cell has a diameter of 18 mm and a plate distance of around 400 μm. C_0 is determined by measuring the dielectric function of three reference samples, in this case air, decane and chloroform, and comparing the results to the values from literature[20,75]. The sample is inserted into the cell via a syringe, taking care that the amount of sample is sufficient for the measurement, but also not so large that the sample gushes out of the cell.

3.4 Static Scattering Experiments

In order to investigate the structures formed by binary mixtures and microemulsions studied in this work, static X-Ray/neutron scattering experiments are used, since they allow for structural determination on a length scale from several nano meters to Angstrom. All experiments performed are static scattering experiments, meaning that only the time averaged scattering is measured, leaving the energy distribution of the scattered particles unresolved. The basic principles for X-ray scattering are almost the same as for neutron scattering, with the only difference being the exact location where scattering takes place. Neutrons scatter at the atomic nuclei of a sample, while X-Rays scatter at the electron shell of the sample atoms. Thus the scattering cross section and with it the scattering contrast in a sample strongly depends on the type of scattering experiment employed. In the following the basic concepts that are equal for X-Ray and neutron scattering experiments will be discussed as well as differences due to the different scattering contrasts will be mentioned. For the following discussion X-Ray and neutrons will be addressed together as radiation unless a distinction needs to be made[76].

Figure 3.1 shows a schematic sketch of a scattering experiment. Monochromatic radiation is scattered from the sample under the *scattering angle* of 2θ and registered by a detector. The incident radiation can be described by a plane wave with a wave vector $\vec{k}_i$ and, since the detector is placed in "far field", the scattered radiation can be described by a plane wave as well with the wave vector $\vec{k}_s$. Assuming a complete elastic scattering

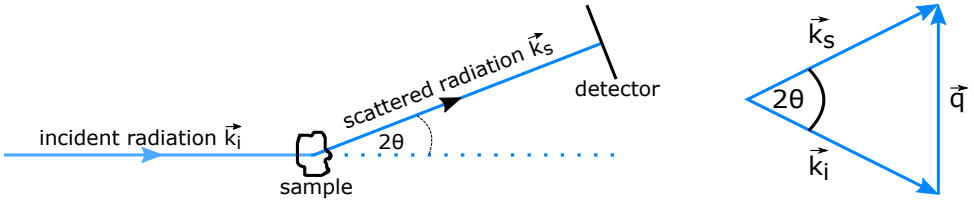

Figure 3.1.: Schematic of a typical scattering experiment and the definition of the scattering vector $\vec{q}$

process, both wave vectors have the same equal absolute value $|\vec{k}_i| = |\vec{k}_s|$. Introducing the scattering vector $\vec{q} = \vec{k}_s - \vec{k}_i$ and its modulus for elastic scattering [76–80]

$$q = |\vec{q}| = |\vec{k}_s - \vec{k}_i| = \frac{4\pi}{\lambda}\sin\theta \tag{3.26}$$

with λ the wave length of the radiation. So the modulus of the scattering vector is directly related to the scattering angle. The scattering vector gives information about the momentum transfer as well, since the momentum of the radiation contains the wave vector $\hbar\vec{k}$. The energy transfer is equal to zero, due to purely elastic scattering and thus measuring the scattered radiation in dependence of the scattering angle 2θ yields a full description of the scattering process [76]. As already mentioned the incident radiation can be described by a plane wave $A_0(\vec{r}, t) = A_0 e^{i(\omega t - \vec{k}_i\vec{r})}$. This wave is scattered at every atom in the sample (either at the nuclei for neutrons or the electron shell for X-Rays). Since the atoms are not fixed in place, the average position $\vec{r}_n$ of every atom is introduced. Assuming coherent scattering without any phase shift during the scattering process the resulting scattered wave can be written as a sum of all single scattered waves [76]

$$A(\vec{r}, t) = \sum_n A_n(\vec{r}, t) = A_0 b \sum_n e^{i(\omega t - \vec{k}_s(\vec{r}_n - \vec{r}))} = A_0 b e^{i(\omega t - \vec{k}_s\vec{r})} \sum_n e^{i\vec{k}_s\vec{r}_n} \tag{3.27}$$

Here the scattering length b is introduced as a measure of the scattering strength of a single atom. Considering a fixed scattering angle 2θ and thus a constant $\vec{k}_s$, $\sum_n e^{i\vec{k}_s\vec{r}_n}$ only yields information about the phase difference between the waves that were scattered at different atoms. This phase difference $\Delta\phi$ can be calculated to $\Delta\phi = -\vec{q}\vec{r}_m$, where $\vec{r}_m$ is the vector between two scattering atoms. Before using this fact to simplify 3.27, it should be mentioned that only intensities, not amplitudes, can be measured. Since intensity is the square of the amplitude $I = A \cdot A^*$, the exponential factors that depend on t and $\vec{r}$ cancel each other out, further simplifying equation 3.27 to [76]:

$$A(\vec{q}) = A_0 b \sum_m e^{-i\vec{q}\vec{r}_m} = A_0 b \int_V n(\vec{r}) e^{-i\vec{q}\vec{r}} dr \tag{3.28}$$

Here the summation was replaced with an integral over the sample volume, assuming that there are numerous continuously dispersed scatterers in the sample and $n(\vec{r})dr$ was introduced as the number of scatterers within a volume element. So for only one species of scatterers, the experiment measures the Fourier transform of the scattering length density $\rho(\vec{r}) = bn(\vec{r})$ [76]. Using Bragg's law, the scattering angles for soft matter samples can

be estimated [79]. Assuming a typical wave length for X-Ray and neutrons of 1.5 Å, scattering angles above 10° are necessary to observe the atomic distances in a crystal lattice. Microemulsions on the other hand form structures in the nano meter regime. Structures on a length scale of about 10 nm would require scattering angles below 1°. Due to this great difference in scattering angels, static scattering experiments are usually divided into *Wide Angle Scattering* and *Small Angle Scattering* experiments [76].

3.4.1 Wide Angle Scattering

As mentioned before, *Wide Angle Scattering (WAS)* can be used to investigate structures on the length scale of Angstroms. So structures of crystals as well as amorphous systems can be resolved. In this work crystalline and semi-crystalline samples will be studied with WAS measurements, so the scattering of crystalline and amorphous systems will be discussed in the following. In a crystalline system the number density of scatterers $n(\vec{r})$ can be expressed as:

$$n(\vec{r}) = n_a(\vec{r}) \otimes n_l(\vec{r}) \tag{3.29}$$

Here the scatterer density of a single atom $n_a(\vec{r})$ was convoluted with the lattice function $n_l(\vec{r})$. Since the system is a crystal with defined lattice positions of the atoms, the lattice function becomes a sum of delta peaks, while $n_a(\vec{r})$ completely depends on the type of radiation used in the scattering experiment. For neutrons $n_a(\vec{r})$ becomes a delta peak, since the wave length of neutrons is usually much larger than the size of a single atomic nucleus and for X-Rays $n_a(\vec{r})$ is the electron distribution of a single atom. The derived convolution can now be inserted into equation 3.28 and simplified by using the convolution theorem [79]:

$$A(\vec{q}) = A_0 b \int_V (n_a(\vec{r}) \otimes n_l(\vec{r})) e^{-i\vec{q}\vec{r}}\, dr = A_0 b \int_V n_a(\vec{r}) e^{-i\vec{q}\vec{r}}\, dr \cdot \int_V n_l(\vec{r}) e^{-i\vec{q}\vec{r}}\, dr \tag{3.30}$$

Since b and $n_a(\vec{r})$ depend on the atom of the sample, they are taken together into the so called *atomic form factor* $f_a(\vec{q})$. Introducing $f_a(\vec{q})$ into the equation yields

$$A(\vec{q}) = f_a(\vec{q}) \cdot \int_V n_l(\vec{r}) e^{-i\vec{q}\vec{r}}\, dr \tag{3.31}$$

It is clear that $f_a(\vec{q})$, like $n_a(\vec{r})$ also depends on the type of radiation used in a scattering experiments. While it is independent of $\vec{q}$ for neutrons, it decreases for X-Rays with increasing $\vec{q}$. Now the lattice function $n_l(\vec{r})$ can be developed into an expanded Fourier series [79]

$$n_l(\vec{r}) = \sum_{h,k,l} n_{hkl} e^{i\vec{G}_{hkl}\vec{r}} \tag{3.32}$$

Where $\vec{G}_{hkl}$ is the reciprocal lattice vector, h,k,l are the Miller indices and n_{hkl} are the Fourier coefficients [79]

$$n_{hkl} = \frac{1}{V} \int_V n(\vec{r}) e^{-i\vec{G}_{hkl}\vec{r}}\, dr \tag{3.33}$$

This can be done, because crystals are symmetric under translation. The new expression for $n_l(\vec{r})$ can also be inserted into equation 3.31, yielding [79]

$$A(\vec{q}) = f_a(\vec{q}) \cdot \sum_{h,k,l} n_{hkl} \int_V e^{i(\vec{G}_{hkl}-\vec{q})\vec{r}}\, dr \tag{3.34}$$

The exponential function in this equation oscillates with a period much smaller then the sample volume, leading to the conclusion that for $\vec{q} \neq \vec{G}_{hkl}$ all contributions from the exponential function are averaged out, by integration over the entire sample volume. This is due to destructive interference of the scattering contributions from the single atoms. Only for $\vec{q} = \vec{G}_{hkl}$ the scattering will not be extinguished, because the exponential function takes on the value of 1 and the integration simply yields the sample volume V. This is the so called "Laue condition" and can also be interpreted as equivalent to *Bragg's law* [79]. Additionally the summation in equation 3.31 can be omitted, since every reciprocal lattice vector $\vec{G}_{hkl}$ represents exactly one Fourier coefficient ρ_{hkl}. Therefore the scattering intensity becomes [79]:

$$|A(\vec{q} = \vec{G}_{hkl})|^2 = |\rho_{hkl}|^2 V^2 \tag{3.35}$$

Thus the scattering angle under which a scattering peak appears is determined by the position of the atom in the unit cell of the sample. The same peaks can be found using *Bragg's law*, where the lattice plane is considered [79]

$$2d_{hkl}\sin\theta = \lambda \tag{3.36}$$

With the d_{hkl} the distance between two atomic planes in the crystal. Both relations can be used in order to determine the crystalline structure of a sample under investigation.

All considerations so far assumed a infinitely expanded crystal, which is not the real case. In a finite crystal there will be no delta peaks, but instead a broadening of the peaks will occur. The smaller the sample crystal is, the more the peaks will be broadening. Also the atoms in a crystal will not be completely still, but their positions will fluctuate, due to the temperature. This causes the peak intensity to decrease with increasing scattering angle. This reduction is called *Debye Waller factor*. Still both phenomena have no effect on the peak position, only on its intensity and width and since the main interest of this work focuses on the peak positions a further discussion of these phenomenons will be omitted, but can be found in literature [79].

Amorphous samples are more difficult to describe theoretically, since they do not have lattice planes and thus scattering occurs in all directions instead of just under a certain angle. The short-range order in amorphous materials causes the scattering intensity to be modulated. This modulation also depends on the scattering angle. Still the intensity can be derived by connecting the scattering intensity to the pair correlation function, which describes the structure of amorphous materials. Taking the scattering amplitude of a single atom $A_m(\vec{q}) = f_m(\vec{q})e^{i\vec{q}\vec{r}_m}$ and its interference with all other n atoms with positions $\vec{r}_n$ into account, the scattering intensity can be calculated [79]

$$|A(\vec{q})|^2 = \sum_m f_m(\vec{q})e^{i\vec{q}\vec{r}_m} \sum_n f_n^*(\vec{q})e^{-i\vec{q}\vec{r}_n} \tag{3.37}$$

By assuming that there is only one sort of atom in the sample and considering that every atom in an amorphic sample has on average the same surrounding, so that $n(r)$ does not depend on direction or choice of reference atom, the intensity of an amorphous sample can be calculated to [79]:

$$\frac{|A(\vec{q})|^2}{Nf^2(\vec{q})} = 1 + \int 4\pi r^2[n(r) - n_0]\frac{\sin(qr)}{qr}dr + \int 4\pi r^2 n_0 \frac{\sin(qr)}{qr}dr \tag{3.38}$$

Where N is the number of atoms in the sample and n_0 is the average particle density. The three terms on the right side of the equation describe different scattering contributions of the sample, The first term describes the scattering of the reference atoms and thus includes no interference. Since $[n(r) - n_0]$ already becomes zero after a few atomic distances, only neighbouring atoms contribute to the scattering of the second term. So it reflects the local structure around the randomly chosen reference atom. Finally the third term becomes larger with increasing distance r from the reference atom and yields the scattering contribution of distant atoms. Additionally this scattering contribution only shows itself in forward scattering ($q \approx 0$), due to the $\frac{\sin(qr)}{qr}$ factor, causing the integrand to already oscillate rapidly for small values of q. The third term is also often referred to as *Small Angle Scattering* and will be discussed later, still it yields no information on the local structure of amorphic systems [79].

For partially crystalline materials the scattering will become even more complex, consisting of crystalline and amorphic scattering contributions. Since most polymers can only form semi crystalline solids, instead of pure crystals, their scattering profile will strongly depend on the size of crystalline/amorphous parts as well as if there is a preferred orientation of the chain inside a unit cell. So a detailed discussion of the scattering of semi crystalline samples lies outside the scope of this work and will be omitted here.

The Bruker D8 diffractometer

For *Wide Angle X-Ray scattering (WAXS)* a *Bruker D8 Advance* in combination with a *TTK 211* from *Anton Paar* was used. The diffractometer uses the copper K_α line with a wavelength of $\lambda = 1.54\,\text{Å}$. Monochromatisation is achieved by using a göbel mirror. The measurements are performed in the $\theta/2\theta$ setup with moving sample holder and detector. The sample holder is made out of stainless steel and contains a trough in which the sample is put in its liquid state. Self adhesive Kapton foil is put on top of the sample trough and holds the sample in place. This prevents the sample from spilling out of the trough when in liquid form and tilted due to the measuring process. Additionally the sample holder can be heated or cooled and allows for the observation of a temperature range from $-65\,°\text{C}$ to $60\,°\text{C}$, when cooling with liquid nitrogen. The sample holder is put inside a vacuum sealed sample chamber that is flooded with nitrogen gas. Measured intensities are not corrected for background or primary beam intensity, because the main interest of this work lies on the peak positions. The used Våntec detector measures with an angle step size of 0.0047°.

3.4.2 Small Angle Scattering

Investigating scattering angles smaller than 1° is done using *Small Angle Scattering*. Since the size of the scattering particles studied is inversely proportional to the scattering angle, the structures *Small Angle Scattering* can determine are in the nanometer regime. Starting with equation 3.28, the scattering intensity of the scattered radiation can be calculated to [76]

$$I(\vec{q}) = |A(\vec{q})|^2 = A(\vec{q}) \cdot A^*(\vec{q}) = \left[\int_V \rho(\vec{u'}) e^{-i\vec{q}\vec{u'}} d\vec{u'}\right]\left[\int_V \rho(\vec{u'}) e^{i\vec{q}\vec{u'}} d\vec{u'}\right] \tag{3.39}$$

By substituting in $\vec{r} = \vec{u'} - \vec{u}$ into the intensity equation and introducing the autocorrelation function of $\rho(\vec{r})$, $\Gamma_\rho(\vec{r})$ the intensity becomes

$$I(\vec{q}) = \int \left[\int \rho(\vec{u})\rho(\vec{u}+\vec{r}) d\vec{u}\right] e^{-i\vec{q}\vec{r}} d\vec{r} = \int \Gamma_\rho(\vec{r}) e^{-i\vec{q}\vec{r}} d\vec{r} \tag{3.40}$$

The scattering length density will vary smoothly due to the spatial resolution of several Angstrom. So a mean scattering length $\langle\rho\rangle$ can be defined, as well as deviations from this mean value $\eta(\vec{r}) = \rho(\vec{r}) - \langle\rho\rangle$. If the sample dimension is much larger than $|\vec{r}|$, the auto correlation function of the scattering density $\Gamma_\rho(\vec{r})$ can be expressed as [76]

$$\Gamma_\rho(\vec{r}) = \Gamma_\eta(\vec{r}) + \langle\rho\rangle V^2 \tag{3.41}$$

Where V is the sample volume. Thus equation 3.40 becomes [76]

$$I(\vec{q}) = \int \Gamma_\eta(\vec{r}) e^{-i\vec{q}\vec{r}} d\vec{r} + \langle\rho\rangle V^2 \delta(\vec{q}) \tag{3.42}$$

So the scattering intensity consists of two terms. The second term represents the scattering caused by the sample as a whole. It is often referred to as the *null scattering* and is not observable in an experiment, because at $\vec{q} = 0$ it is drowned out by the much stronger, unmodified transmitted beam [76]. Thus this term will be omitted from now on. The first term yields the detectable intensity and is only caused by deviations from $\langle\rho\rangle$, so only contrasts in scattering length densities can be measured. It can also be seen that the correlation function $\Gamma_\eta(\vec{r})$ is not sensitive to the sign of the deviation. So an image shows exactly the same scattering intensity as its negative, this is known as *Babinet principle*.

Since the intensity measured in *Small Angle Scattering* only depends on the difference in scattering length densities, the intensity can once be divided into a form factor and a structure factor part. For samples containing a low concentration of scattering particles, the positions of the particles are not correlated and the sum of the scattering signal from different particles becomes zero. So the absolute scattering intensity only depends on the number of scattering particles, while the q-dependence is fully described by one scattering particle and is called the form factor $F(\vec{q})$. It is derived by Fourier transforming the difference in scattering length densities between the scattering particle and the matrix in which it is dissolved. The form factor can be calculated, if the structure of the scattering particle

is well known, for example the form factor of a spherical droplet was given in section 2.2.2. Increasing the concentration of scattering particles or if particles start to aggregate, the positions of the particles become correlated. This leads to a coherently summed up scattered intensity of the single particles. Now the form factor alone can not describe the scattering intensity and thus the structure factor $S(\vec{q})$ needs to be introduced. This factor can either be calculated, like the *Hard sphere* structure factor in section 2.2.2, or be determined phenomenologically. The time and ensemble averaged scattering intensity of the sample as a whole can be expressed as [76,78,81]

$$\langle I(\vec{q})\rangle = N\left(\langle F(\vec{q})^2\rangle S(\vec{q}) + \langle F(\vec{q})^2\rangle - \langle F(\vec{q})\rangle^2\right) \tag{3.43}$$

It is necessary to average the intensity, due to the fact that the scattering particles are not monodispers and are diffusing through the sample volume. The second and the third term in the equation above are caused by scattering, which deviates from the averaged form factor. This scattering is also called *Laue scattering*.

Instruments for Small Angle Scattering

Small Angle Scattering experiments in this work are done using X-Rays and neutrons. For *Small Angle X-Ray Scattering (SAXS)* measurements a setup by *Molecular Metrology* working with the copper K_α line is used. This line has a wavelength of $\lambda = 1.54\,\text{Å}$. A göbel mirror and three pinholes collimate the primary beam, making it point-shaped with a diameter of about half a millimetre. The detector is a two-dimensional multi-wire gas detector with 1024 x 1024 pixels, so there is a minimum difference between two q-values of $0.0012\,\text{Å}^{-1}$. The q calibration of the instrument is done by measuring silver behenate as a calibration sample and full width half maximum of the peak of silver behenate is also used to estimate the resolution of the detector. Since all samples investigated in this work show an isotropic scattering pattern, the measured intensity can be radially averaged in the detector plane, thus increasing intensity. The temperature of this setup is controlled by a *Linkam stage* and liquid nitrogen making a temperature range between $-100\,°\text{C}$ and $200\,°\text{C}$ accessible.

For water/PEG mixtures the detector distance is about 1.5 m, leading to a q-range of $0.008\,\text{Å}^{-1} \leq q \leq 0.25\,\text{Å}^{-1}$. The resolution from the silver behenate peak is estimated to $\Delta q = 0.007\,\text{Å}^{-1}$. The mixtures are put inside a Teflon ring and covered with Kapton foil. The sample is then sealed with two metal rings so that the beam can pass through the sample, but the sample in its liquid phase will not spill out of the sample holder.

Microemulsions were investigated with a detector distance of 0.75 m, with a q-range of $0.013\,\text{Å}^{-1} \leq q \leq 0.45\,\text{Å}^{-1}$. Due to the shorter detector distance the resolution becomes slightly worse $\Delta q = 0.01\,\text{Å}^{-1}$. The microemulsion are measured inside glass capillaries with a diameter of 1.5 mm and a wall thickness of 0.01 mm. The capillaries are vacuum-sealed, by melting their opening shut with a Bunsen burner.

Small Angle Neutron Scattering (SANS) experiments were performed at the *D33* of the *Institut Laue Langevin (ILL)* in Grenoble. The neutrons had a wavelength of 5 Å with a spread of 10%. The detector was positioned at 2 m, 5 m and 12 m, yielding a q-range of

$0.01\,\text{Å}^{-1} \leq q \leq 0.56\,\text{Å}^{-1}$. The data was then radially averaged and background corrected by measuring the scattering profile of an empty beam and an empty sample cell. Further the is radially averaged, background corrected using an empty beam and empty cell measurements and normalised by measuring the scattering of water, in order to obtain absolute intensities (I in units of cm^{-}1 using *ILL* standard procedures. *Suprasil* glass cuvettes by *Helma* were used as sample cells. They have a wall thickness of 1.25 mm and provide a sample thickness of 1 mm. The sample volume inside the cuvettes is 350 μL.

Part II.
Experimental Results

4 Phase Diagram and Structures of Water and Polyethylene Glycol Mixtures

The synthetic polymer PEG (sometimes referred to as PEO or POE) has a wide area of applications. It is used in chemical and biological research, has industrial and medical utilisations and it is also often processed in cosmetic products [11,30]. As already mentioned it has a unique solubility in water, which is caused by the interaction between PEG and the hydrogen bond network of water. This interaction causes PEG to be soluble in water at any concentration, as long as the temperature of the mixture is high enough. It has been the subject of many studies to investigate, if and how this interaction changes when the mixture is cooled below the crystallisation temperature of PEG and/or water and at which temperature the entire mixture becomes solid.

The following chapter will discuss measurement results of DSC, SAXS and WAXS experiments on water mixed with PEG1500 or PEGDME1650. DSC measurements are employed to demonstrate the eutectic behaviour of the mixtures as well as to determine the phase diagram. With the resulting phase diagram, the mixtures are then structurally investigated using X-Ray scattering techniques. WAXS measurements are able to investigate the crystal structures emerging in the mixture upon cooling and to determine, if the crystals are solid solutions or crystals of the pure components. At last these results are combined with the results from SAXS measurements, which allow for the observation of the size of amorphic and crystalline domains that form below the phase transition temperatures.

4.1 The Phase Diagram of Water/Polyethylene Glycol Mixtures

The phase diagram of water/PEG mixtures containing PEG with varying molecular weight has been extensively studied and it was found that water/PEG mixtures form an eutectic system [30,32,82–84]. The eutectic concentration as well as the eutectic temperature depend on the molecular weight of the PEG, with increasing chain length the eutectic temperature increases, while the eutectic concentration decreases [30,83]. It remains an open question, if the endgroups have an influence on the eutectic concentration and temperature. In order to obtain the phase diagram and with it the eutectic temperature and concentration of the water/PEG1500 respectively the water/PEGDME1650 mixtures, the DSC samples were first held at 333 K for 10 minutes to make sure they are in a homogeneous liquid phase. They were then cooled to 193 K at 5 K/min and held at that temperature for 30 minutes, in order to ensure crystallisation. Finally the samples were then heated at 2 K/min back to 333 K to completely transition back into a homogeneous liquid phase. Since the crystallisation temperature obtained from cooling depends on the cooling rate, the melting temperatures from heating cycles are used to determine phase transition temperatures.

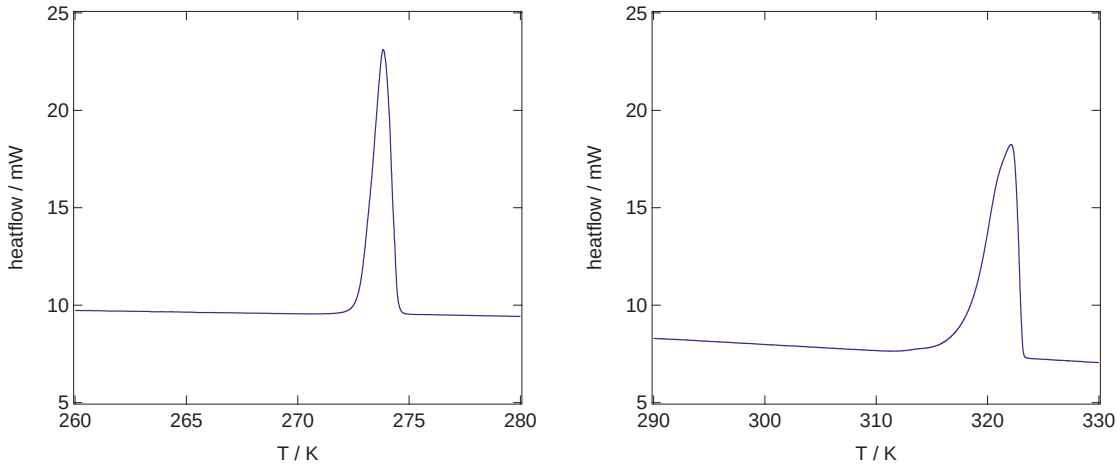

Figure 4.1.: Left: DSC heating curve of water Right: DSC heating curve of PEG1500

Figure 4.1 shows the DSC heating curves obtained for water and PEG1500 with the mentioned temperature cycle. Both components show a very sharp melting peak that yields a melting temperature (peak onset) and the corresponding melting enthalpy. The onset temperature of the water peak can be evaluated to 272.9 K, which is not exactly the literature value of 273 K [83]. So there is an uncertainty when determining the melting temperatures that will be estimated to 0.5 K due to peak form and possible peak overlap. The melting enthalpy of water can be calculated to 345.75 J/g from the observed peak. This value also differs from the literature value of 334 J/g [83,84] and thus the uncertainty of the calculated enthalpy is estimated to 5%. It is assumed that the water from the Millipore DirectQ3 system is not contaminated and that there is no contamination during the transfer to the sample cell. Thus the melting temperature of PEG1500 evaluates to (318.2 ± 0.5) K, while the melting enthalpy calculates to (154.40 ± 7.72) J/g, which is in good agreement with literature [85,86]. It should be mentioned that the crystallinity of PEG1500 is not 100%, but no observable glass transition could be measured. The baselines of the measurements is not a constant value, but instead exhibits a slope that is not equal for all measurements. This is due to the large temperature range, but since the intersection between baseline and peak flank is determined, this slope does not influence the results.

While the pure components only exhibit one melting peak in the heating curve, the mixtures show more features in the DSC curves. This can be seen in figure 4.2 where the heating and cooling curves for the mixtures containing 30 wt% and 60 wt% PEG1500 are shown. The sample containing 30 wt% PEG1500 exhibits one sharp crystallisation peak around 233 K when cooled. The heating curve shows a glass transition around 203 K, then a cold crystallisation occurs at ∼218 K and the curve also exhibits two melting peaks. These features are typical for water/PEG mixtures [30,32,82–84]. On the other hand the 60 wt% sample shows no feature in the cooling curve and only the glass transition and one melting peak in the heating curve. This has also been observed in literature [82].

Figure 4.3 shows the DSC heating curves for all prepared water/PEG1500 samples. It can bee seen that by adding PEG1500 to water a second melting peak, the eutectic peak, around 253 K arises, while the melting peak of water, the liquidus peak, shifts to lower

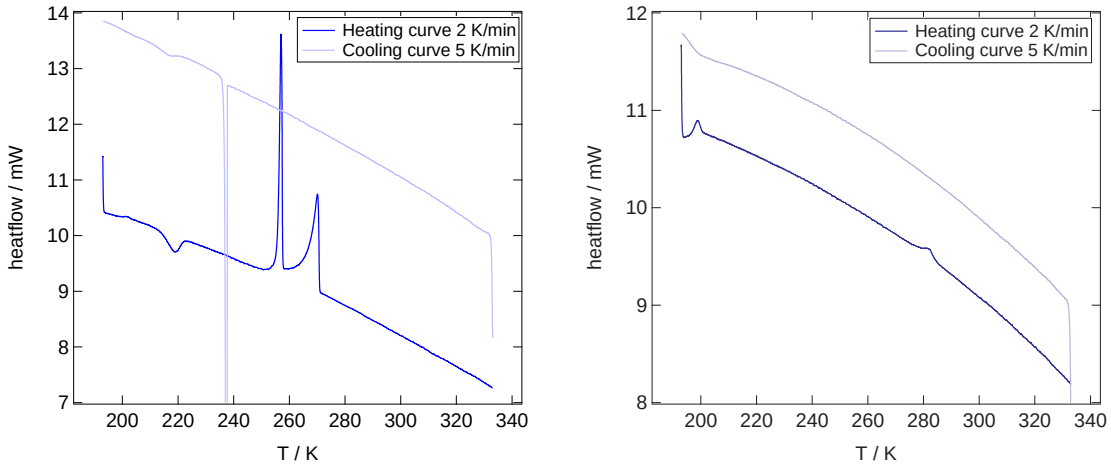

Figure 4.2.: Left: DSC heating and cooling curve of a water/PEG1500 mixture containing 30 wt% PEG1500 Right: DSC heating and cooling curve of a water/PEG1500 mixture containing 60 wt% PEG1500

temperatures and becomes smaller. Additionally the cold crystallisation starts to show and becomes stronger. At 50 wt% PEG1500 there is only one melting peak indicating that this is the eutectic concentration. By increasing the content of PEG1500 further in the mixture the liquidus peak arises again and shift to higher temperatures until it arrives at the melting temperature of pure PEG1500. This causes the eutectic peak to become smaller and to already be gone at a concentration of 95 wt% PEG1500. This is probably due to the fact that for high PEG concentrations there is only one water/PEG solid solution melting at the liquidus temperature and no other solid phase has formed. The glass transition can not be observed for all concentrations, because it moves to temperatures lower than the lowest observed temperature. These findings are also reported on numerous occasions [30,32,82–84].

By obtaining all the eutectic and liquidus peak onset temperatures, the phase diagram of the water/PEG1500 mixtures can be constructed. The phase diagram is shown in figure 4.4. The diagram already contains a line fit to the eutectic onset temperatures in order to determine the eutectic temperature of $(254.2 \pm 0.5)\,\mathrm{K}$. It also shows the fit of the melting point depression model from section 2.1.3:

$$\frac{1}{T_{MA}} - \frac{1}{T^0_{MA}} = \frac{-R}{\Delta H_A}(\ln(1-\phi_B) + \left(1 - \frac{1}{V_r}\right) + \chi\phi_B^2) \tag{4.1}$$

for the water rich side ($wt\%PEG \leq 0.5$), where T^0_{MA} is the measured water melting temperature of 272.9 K and ΔH_A the measured molar enthalpy of water calculated to 6223.5 J/mol. The ratio of the molar volumes can be calculated to $V_r = 68.85$ with the molar volume of water ($18.1\,\mathrm{cm}^3$) and one PEG monomer ($37.0\,\mathrm{cm}^3$) provided by Huang et al. [30]. For the polymer rich side ($wt\%PEG \geq 0.5$) the melting point depression becomes:

$$\frac{1}{T_{MB}} - \frac{1}{T^0_{MB}} = \frac{-RV_u}{\Delta H_B V_A}\left(\left(1 - \frac{1}{V_r}\right)\phi_A - \frac{1}{V_r}\ln(1-\phi_A) - \chi\phi_A^2\right) \tag{4.2}$$

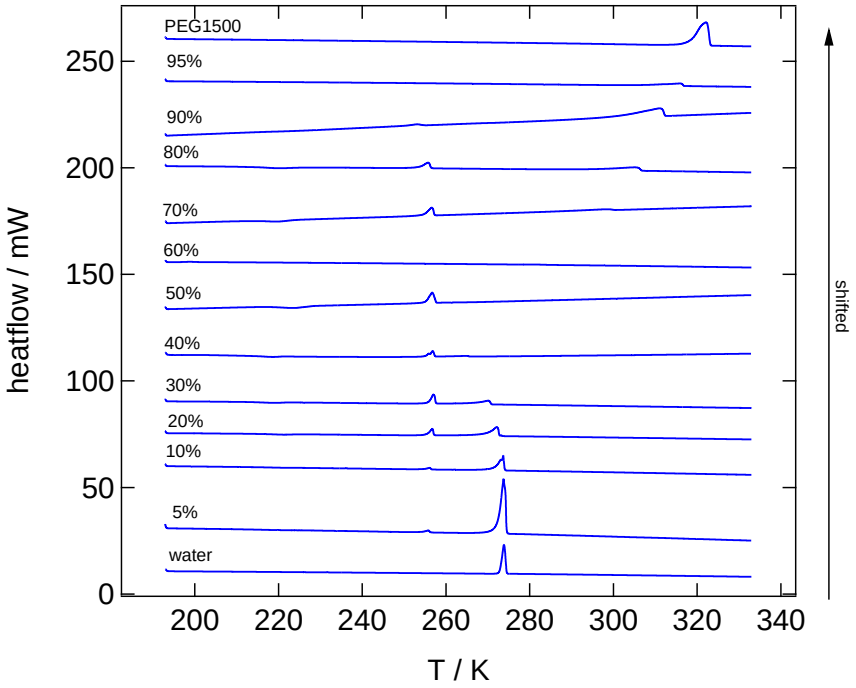

Figure 4.3.: DSC heating curves of all measured mixtures of water and PEG1500 the percentages give the wt% of PEG1500 contained in the mixture. The curves are shifted for clarity.

With the PEG melting temperature T^0_{MB} of 318.2 K and the molar melting enthalpy of one monomer PEG $\Delta H_B = 6876.48\,\mathrm{J/molmonomer}$. It can be seen that the water rich side can be very well described by this model and it yields an interaction parameter of $\chi = -0.10 \pm 0.02$, which is slightly smaller than earlier found values [30,32,83]. On the polymer rich side however the model fails to describe the data. This can already be observed in the course of the transition temperatures by themselves and is further illustrated by the dashed line which shows the theoretical melting point depression for the interaction parameter derived from the water rich side. The data can be described by using a volume fraction dependent interaction parameter of the form (see section 2.1.3):

$$\chi = \chi_0 + \chi_1 \phi_B + \chi_2 \phi_B^2 \tag{4.3}$$

Where $\chi_0 = -0.1$ is set beforehand as a result from the fit to the water rich side. This is just a phenomenological approach, so the values for $\chi_1 = 0.16 \pm 0.09$ and $\chi_2 = 3.97 \pm 0.15$ do not have any physical interpretation and differ from values found in literature [30]. More interesting instead is the fact, that the liquidus transition temperatures of the polymer rich side start to deviate from the constant interaction parameter for the concentrations where an eutectic melting peak is present. At 95 wt% PEG the liquidus transition temperature lies perfectly on the dashed line, indicating that for high concentrations of PEG the formed solid solution obeys the Flory-Huggins melting point theory, but as soon as the eutectic solid 50:50 phase can form due to a higher water concentration the melting point depression is highly hindered and causes the liquidus temperature to be much higher than expected. This has also been reported before [30,32,82,83].

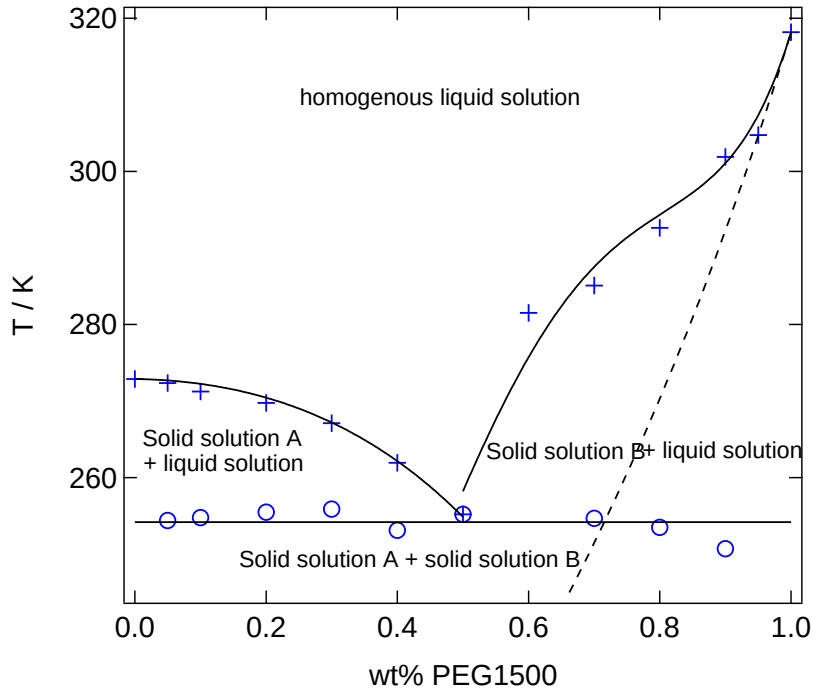

Figure 4.4.: The phase diagram of water/PEG1500 mixtures. Circles represent the eutectic melting peak temperatures , while crosses represent the onset temperatures of the liquidus peak. Eutectic onset temperatures were fitted with a constant and the crosses were fitted with the melting point depression model. Fits a indicated by black lines. The dashed line shows the melting point depression of PEG for the same interaction parameter that was determined for water. Error bars are omitted since they are smaller than the plot symbols.

Focusing on the melting/freezing enthalpies should also yield information about the kinetics of the melting/crystallisation process of water/PEG mixtures. Figure 4.5 shows the calculated enthalpies of the liquidus and eutectic peaks of the heating curves, as well as the enthalpies of the crystallisation and cold crystallisation dips of the cooling/heating curves. The enthalpy of the liquidus peak starts to decrease when PEG is added to water until the eutectic concentration, where it becomes zero. Adding more PEG the liquidus enthalpy rises again until it reaches the enthalpy of pure PEG. The enthalpy of the eutectic peaks behaves the opposite way. It has its maximum at the eutectic concentration and becomes zero for pure water and PEG. Similar behaviour can be found when looking at the exothermic processes happening inside the thermal cycle of the DSC measurements. The crystallisation dip of the cooling curve becomes weaker when approaching the eutectic concentration and stronger when moving closer to the pure components. The cold crystallisation does become stronger when adding PEG to water or vice versa, while it becomes weaker when shifting away from the eutectic concentration. This does indicate that in order to observe a distinguished eutectic melting peak the sample has to be cooled down below the temperature of the cold crystallisation otherwise the eutectic melting peak will not be as prominent. Since a cold crystallisation shows in the heating curve it can be assumed that this crystallisation process is not finished before the mixture transitions into the glassy state. The very sharp dips in the cooling curve show that the

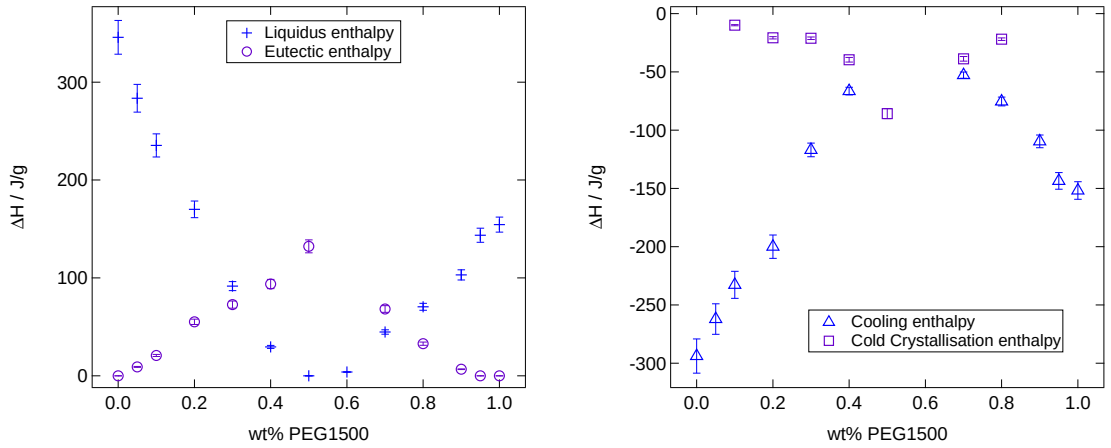

Figure 4.5.: Left: Melting enthalpies of the liquidus and the eutectic peaks of water/PEG1500 mixtures. Right: Enthalpy released by cooling and enthalpy released by the cold crystallisation of water/PEG1500 mixtures. The enthalpy is given per gram of sample.

crystallisation kinetics of the melting point depressed pure components are much faster than the the kinetics of the eutectic crystallisation. This is probably due to the fact that the PEG and water contained in the 50 wt% eutectic composition, which are still liquid after the liquidus crystallisation and above the eutectic temperature, need to separate before they can crystallise. They are not able to crystallise into a solid solution, but instead into crystalline PEG and ice. This separation appears to be very slow and only by heating the mixture very slowly it has enough time to complete this separation and crystallise into the pure components. This would also explain why there is no eutectic peak at 95 wt% PEG1500. At this concentration the mixture is able to form a solid solution crystallising while cooling and leaving no liquid solution behind that would need to separate into the pure components.

For 60 wt% no eutectic peak could be measured, but there was also no crystallisation or cold crystallisation dip in the measured curves. Huang et al.[30] and Bogdanov et al.[82] found that the eutectic melting peak for such a chain length and concentration is very weak or can not be measured. The same is found for the cold crystallisation[30,82]. Also the crystallisation dips are a bit weaker than the melting peaks. So for very high water or PEG concentrations the eutectic melting peak is very small and since the cold crystallisation is even smaller it can not be distinguished from the baseline.

In order to deepen the knowledge about the crystallisation kinetics, the endgroups of the polyethylene glycol are varied and water mixtures containing polyethylene glycol dimethyl ether are investigated. The measurement results of the water/PEGDME1650 mixtures show some similarities to the water/PEG1500 mixtures, but also some differences as well. Since the features exhibited by the heating and cooling curves are the same, figure 4.6 only shows the pure dimethyl ether and the mixture containing 60 wt% PEGDME. PEGDME1650 melts at (310.9 ± 0.5) K and the peak is not as sharp as the melting peak of PEG1500, which is probably due to the fact that the larger chain ends prevent the PEGDME1650 from crystallising as structured as PEG1500, but the peak structure also suggests that a second and third melting process take place inside the sample. This could hint at different species of PEGDME1650 chains, each with a slightly different melting

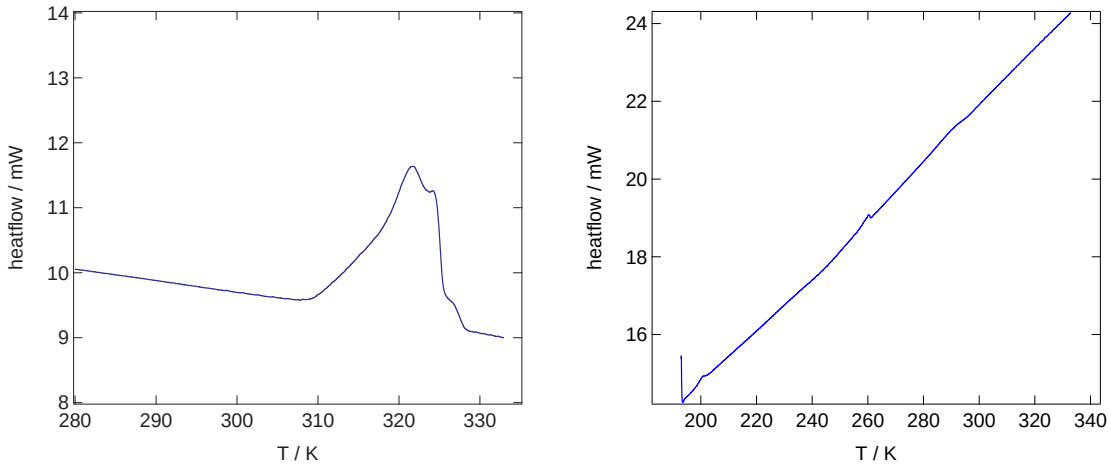

Figure 4.6.: Left: DSC heating curve of PEGDME1650. Right: DSC heating curve of a water/PEG1650 mixture containing 60 wt% PEG1650

temperature. The sample containing 60 wt% PEGDME1650 shows an eutectic melting peak, but no liquidus melting peak. This is opposite to the sample with the same concentration of PEG1500, but the eutectic peak is still very weak.

Figure 4.7 shows the phase diagram obtained for water/PEGDME1650 mixtures. The eutectic concentration is 50 wt% and the same as for water/PEG1500 mixtures. Temperatures obtained from the eutectic melting peaks can be described by a horizontal line for concentrations equal or below the eutectic concentration. For concentrations higher than 50 wt% the eutectic melting peaks yields decreasing temperatures, which is also exhibited by PEG of higher molecular weight (70.000 g/mol) than PEG1500[30]. So to determine the eutectic temperature only the water rich side of the phase diagram is used and yields (259.9 ± 0.5) K. This is also the same as for water mixed with PEG of higher molecular weight[30]. Since the number of monomers is only 3 more for PEGDME1650 than for PEG1500, these effects can not be caused by the chain length increase as is the case for PEG1500 and PEG70000. Thus it seems that changing the endgroups causes changes in the system that can also be caused by a massive increase in the chain length. The phase diagram also shows the melting point depression model for the water and polymer rich side, where the water rich side can again be described with a constant interaction parameter $\chi = 0.07 \pm 0.02$. Taking the degree of polymerisation (N=36-37) into account, an interaction parameter of this size would cause a phase separation[7]. Since this can not be observed in the liquid state of the investigated samples, the real interaction parameter must be smaller. Judging by the blue dashed line in the phase diagram, which represents an interaction parameter of $\chi = -0.1$, the real interaction parameter will most likely lie between -0.1 and 0.05. Due to the fact that 0.05 is within the uncertainty of the χ obtained from the fitting procedure, the interaction parameter will be assumed to $\chi = 0.05$.T he polymer rich side again can only be described by introducing a volume fraction dependent interaction parameter. The dashed line that shows the polymer rich side's melting point depression for the same interaction parameter as the water rich side, deviates completely from the obtained data, although the mixture containing 95 wt% PEGDME shows again no eutectic melting peak. It can also be seen that fitted liquidus

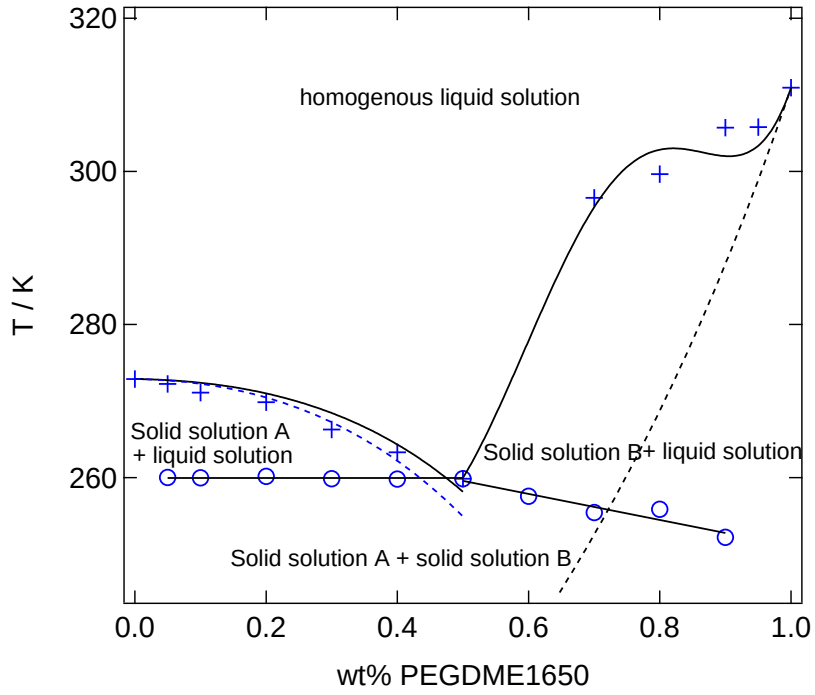

Figure 4.7.: The phase diagram of water/PEGDME1650 mixtures. Circles represent the eutectic melting peak temperatures , while crosses represent the onset temperatures of the liquidus peak. Eutectic onset temperatures were fitted with a line and the crosses were fitted with the melting point depression model. Fits are indicated by black lines. The dashed line shows the melting point depression of PEG for the same interaction parameter that was determined for water. The blue dashed line shows the course of a melting point depression of PEGDME1650 with the same interaction parameter as PEG1500. Error bars are omitted since they are smaller than the plot symbols.

line shows a local maximum, indicating a even greater deviation from the Flory-Huggins model than for water/PEG1500 mixtures. An important difference between the two systems is that now for water/PEGDME1650 mixtures the determined interaction parameter changed and became positive. The blue dashed line in the diagram shows that the same interaction parameter as for water/PEG1500 mixtures would describe the data not as well as a positive one. These observations allow for the assumption that both polymer chains have the same maximum capacity for hydrogen bonding per monomer, since the eutectic concentration does not change, but the interaction between the water molecules and the polymer chains changes as if the chain length was increased by a factor of more than 10. Huang et al.[30] attribute the interaction change to the absence of amorphous PEG chains in water/PEG mixtures with high molecular weight PEG. Since there should be amorphous PEGDME1650 chains in the crystalline state, the interaction change is caused by the methyl groups at the ends of the chain. This would explain the not changing eutectic temperature as well as the change in the interaction parameter. The addition of three monomers is not large enough to accommodate more water molecules per monomer than the PEG1500, but the larger chain ends cause an increase in the energy needed to melt the two pure components into a homogeneous liquid solution at the eutectic temperature. This holds true for the water rich side of the system, for the polymer rich side the eutectic temperature keeps decreasing, because with increasing polymer concentration it becomes

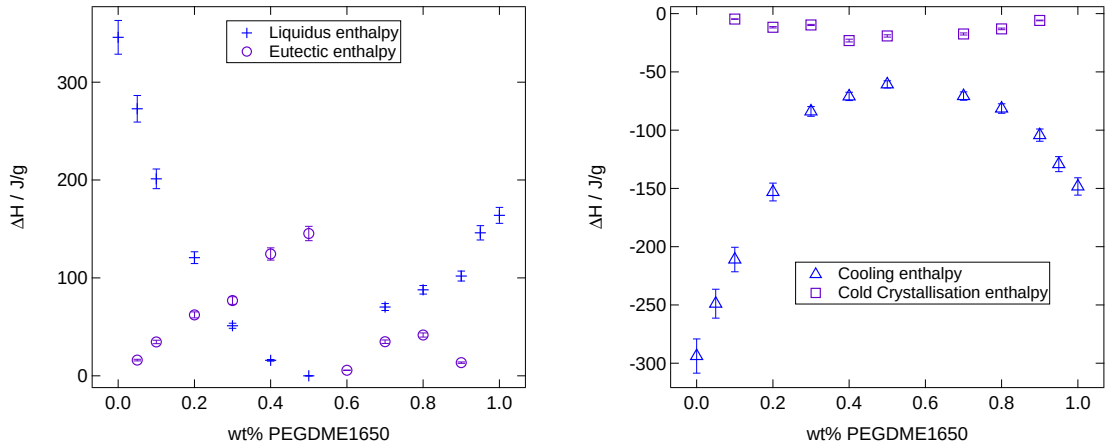

Figure 4.8.: Left: Melting enthalpies of the liquidus peak and the eutectic peaks of water/PEGDME1650 mixtures. Right: Enthalpy released by cooling and enthalpy released by the cold crystallisation of water/PEGDME1650 mixtures. The enthalpy is given per gram of sample.

easier for the PEGDME1650 to expel the water and span a network through it, dissolving its hydrophilic groups in the water, shielding them from the high number of hydrophobic groups provided by the polymer chains (see section 2.1.2)

This interpretation is supported by the comparison of enthalpies in figure 4.8. While the enthalpies of the liquidus and eutectic melting peaks show the same behaviour and about the same strength as the enthalpies for water/PEG1500 mixtures, the enthalpies of the crystallisation and cold crystallisation dip only show the same behaviour, but are different in strength. The enthalpy released during the cold crystallisation is smaller than for water/PEG1500 mixtures, while the enthalpy released during crystallisation is larger for concentrations at which a cold crystallisation also occurs. So during cooling the larger chain ends of the sample cause the crystallisation dynamics to be slightly increased and thus more of the sample can crystallise during the cooling cycle, before the temperature is too low for further crystallisation processes to occur. This is in good agreement with the observed increased in the eutectic temperature of the water rich side. Mixtures containing PEDDME1650 instead of PEG1500 can crystallise faster, because the PEGDME1650 disturbs the water network more than the PEG1500 and so more energy is needed to dissolve the crystalline PEGDME1650 again.

4.2 Crystals and Crystalline Structures inside the Liquidus and Eutectic Phase Boundaries

In order to observe the crystalline structures in water and polyethylene glycol mixtures, WAXS measurements are employed. The samples are put into the sample holder in their homogeneous liquid state. Then the samples were rapidly cooled to 208 K and kept at that temperature for 30 minutes due to the necessity of the cold crystallisation. The samples were then heated again to 233 K and kept there again for 30 minutes to ensure a complete crystallisation of the sample and measured. Then the temperature was increased again, with the increment of the increase depending on the concentration of PEG in the sample, due to the different liquidus temperatures. Increments were chosen to yield a sufficient

number of temperatures below and above the eutectic temperature and below the liquidus line. Measurements above the liquidus line were only done at one temperature in order to obtain the scattering curve produced by a homogeneous liquid phase. Every angle was measured for 120 seconds and then the measured intensities and angles were averaged every ten data points in order to improve statistics, yielding a measuring time of 1200 seconds per angle. WAXS measurements will show, if there are only crystals of the pure components below T_L, due to the separation of the materials and if the presence of a second component causes a difference in the crystals of the pure components.

Figure 4.9 shows the scattering curve obtained for pure water/ice at 260 K and the theoretical model scattering curve for hexagonal ice calculated by the program "POWDER CELL"[87] with the atomic positions in the unit cell provided by Fortes et al.[4]. The model curve is in good agreement with the measured data and both are in good agreement with literature provided scattering curves for hexagonal ice[88–91]. So the ice phase crystallising inside the sample holder seems to be pure hexagonal ice. Still there is some difference in the relative peak intensity between the model and the measurement, which is probably due to a preferred orientation inside the sample holder. Above 273 K the peaks of the ice crystal disappear and only an amorphous halo remains in the scattering data, since the ice melted into liquid water.

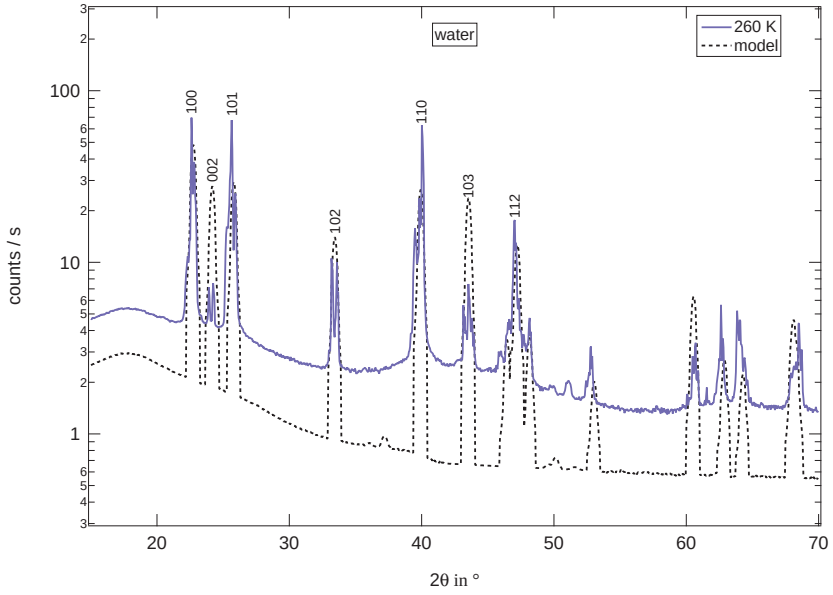

Figure 4.9.: WAXS measurement of pure ice at 260 K. The dashed black line indicates the theoretical scattering curve of hexagonal ice. Sample holder peaks are covered by peaks of the hexagonal ice.

The measurements done on pure PEG1500 at different temperatures are displayed in figure 4.10 alongside the theoretical scattering curve of the crystal. Atomic positions in the unit cell of PEG1500 are provided by Takahashi et al.[92]. Model and measurements are again in good agreement with the above mentioned difference in relative peak intensity. It is also shown that increasing the temperature does not alter the scattering curve significantly, before the crystal melts. There is no decrease in intensity, broadening of the peaks or a shift in peak position observable. At 323 K the PEG is molten and only peaks of the sample holder can be observed.

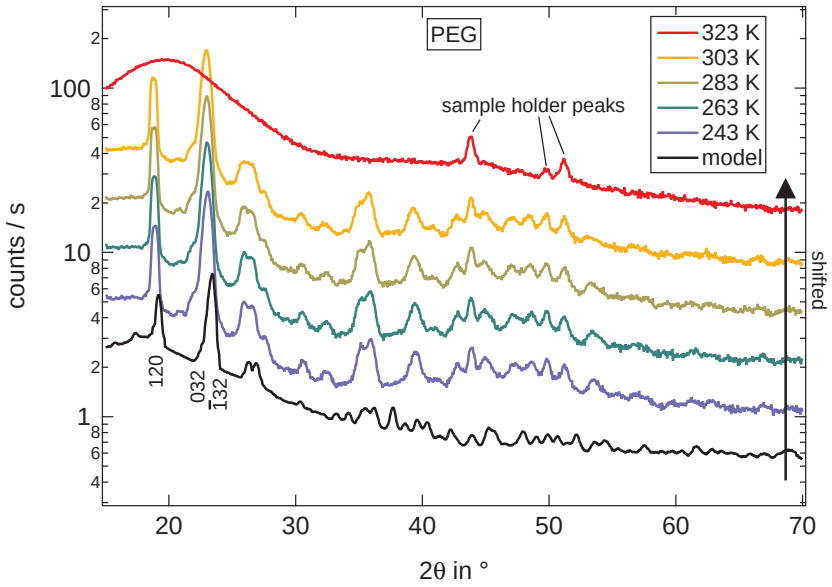

Figure 4.10.: WAXS measurement of pure PEG1500 at different temperatures. The black line indicates the theoretical scattering curve of PEG1500. Curves are shifted for clarity.

The influence of increasing PEG1500 concentration on the scattering curve at 243 K (below T_E) can be seen in figure 4.11. One can see that for low concentrations of water or PEG1500 the scattering curves equal the scattering curves of the pure major component. But increasing the minor component leads to the appearance of peaks from the crystal of the minor phase. All peaks in the diffractogram can be associated with peaks from either pure hexagonal ice or a pure PEG1500 crystal, so there is no evidence of the formation of a solid solution/mixed crystal. The 30 wt% sample yields quite the peculiar scattering curve. While the appearing peaks can be assigned to corresponding hexagonal ice peaks, there are quite a lot of peaks that are present in the 10 wt% and 50 wt% sample, but not the 30 wt% sample. In addition the [101] peak at around 26°, the [112] peak at around 48° and the [203] peak at around 61° become more pronounced in intensity. This is once again seen for measurements with the same samples above the eutectic temperature at 263 K displayed in figure 4.12. Here the scattering curves only show peaks of pure PEG1500 (above 50 wt%) or of pure water (below 50 wt%). The scattering curve of the eutectic concentration sample only exhibits scattering peaks of the sample holder, since it is completely liquid above T_E. This proves that below T_L a pure crystal of the major phase starts to form, while the minor phase remains in a homogeneous liquid phase with the liquid rest of the major phase. Again the scattering curve of the 30 wt% sample exhibits an absence of major water peaks that are present for the 10 wt% sample.

For the samples containing 20 and 40 wt% PEG1500 the same phenomenon can be observed. Changes in the diffraction pattern of hexagonal ice can sometimes be explained with the appearance of a stacking disorder [89–91]. This disorder causes the formation of cubic ice inside the hexagonal ice lattice and thus scattering peaks of cubic ice start to appear and peaks of the hexagonal ice phase become weaker or disappear. But the [101] and the [203] would disappear in an ice crystal made up out of hexagonal and cubic ice, while the [002] peak at 24° would become more pronounced [89–91].

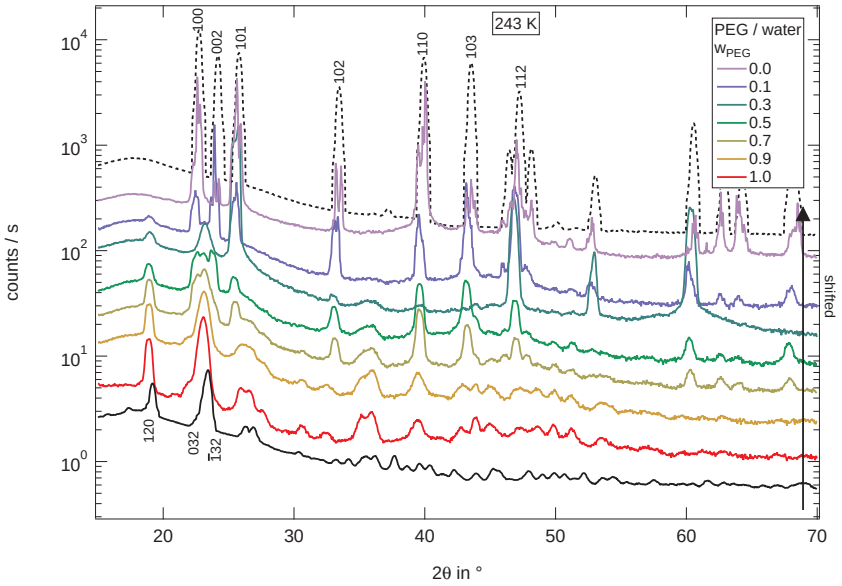

Figure 4.11.: WAXS measurements for samples containing different wt% PEG1500 at 243 K. The dashed black line shows the theoretical hexagonal ice and the black line the theoretical PEG1500 scattering curve. The curves are shifted for clarity with the same multiplication factor.

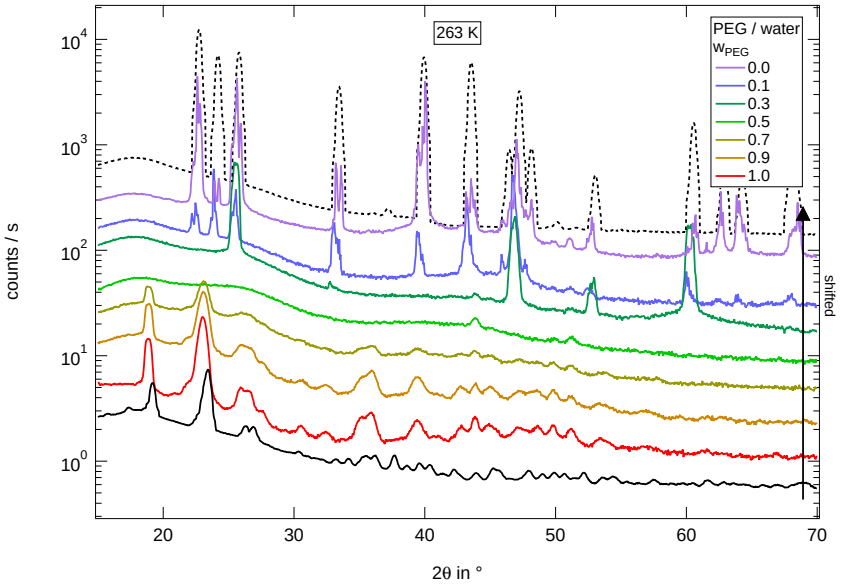

Figure 4.12.: WAXS measurements for samples containing different wt% PEG1500 at 263 K. The dashed black line shows the theoretical hexagonal ice and the black line the theoretical PEG1500 scattering curve. The curves are shifted for clarity with the same multiplication factor.

So instead of a stacking disorder there seems to be a preferred orientation in which the ice crystal grows. This orientation seems only to be present for water amounts between 10 and 50 wt%, since it is not observed for these two samples. Due to the remaining peaks and their miller indices it can be assumed that the preferred growth direction would be along the a- and c-axis of the hexagonal lattice. This could be achieved by PEG molecules

bonding to the water molecules via hydrogen bonding while being surrounded by liquid water molecules on the other side. Thus the PEG would not be part of the ice crystal, but block the growth in the other directions. The PEG can only bind under certain conditions/distances of the water molecules and so does only bind at certain area of the lattice, leaving unbonded sites free to grow.

In figure 4.13 the influence of temperature on the scattering profile can be seen. The model depicted is obtained by adding 30% of the pure ice scattering to 70% of the pure PEG scattering at 243 K. This simple approach describes the scattering data below the eutectic temperature very well, disregarding the differences in relative intensity. Above T_E only scattering of a PEG1500 crystal can be observed and heating above T_L causes only the sample holder peaks to remain. This supports the finding that no solid solution is formed when the samples crystallises. Instead the liquid phase below T_L separates into the two pure components that then crystallise. But it can also be seen that the peaks start to lose intensity before the liquidus line is crossed when heating, hinting at a continuing melting process instead of a sharp one. This could also explain the very broad liquidus melting peaks found for high wt% of PEG1500. In order to validate this assumption the

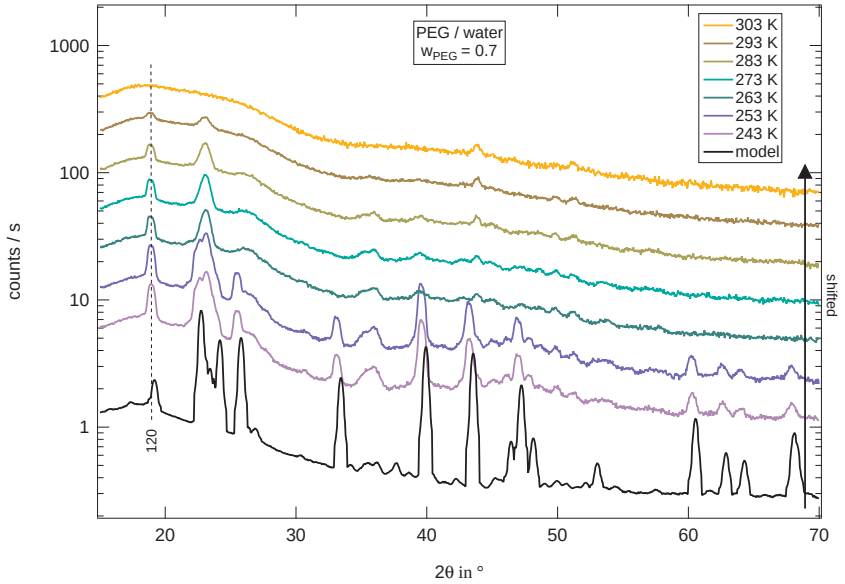

Figure 4.13.: WAXS measurements for samples containing 70 wt% PEG1500 at different temperatures. The black line shows a model curve calculated by adding the corresponding percentages of the ice and PEG1500 scattering curves. The curves are shifted for clarity with the same multiplication factor.

peak area of the [120] PEG peak at around 19° is determined for the samples containing more than or exactly 50 wt% PEG1500 at all temperatures via a Gauss fit. The area is then normalised by dividing it with the area of this peak for the pure PEG1500 sample at 243 °C. The results of this approach can be seen in figure 4.14. The coloured dashed lines show the expected relative intensity, due to the concentration of PEG in the sample. The obtained results deviate strongly from this expectation, especially the sample containing 70 wt% of PEG. Pure PEG1500 remains constant around one, which validates the results yielded by the Gauss Fit.

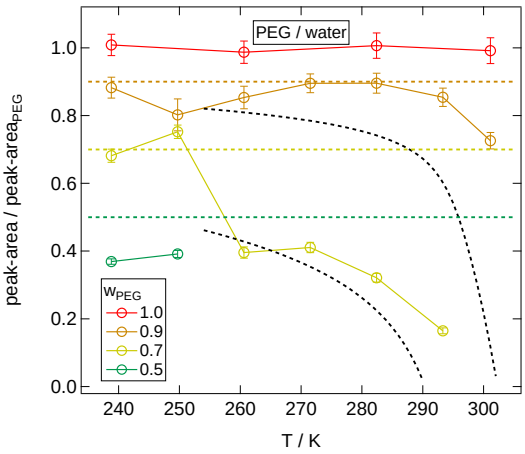

Figure 4.14.: Normalised peak area of the [120] PEG peak appearing in samples of the PEG rich side of the phase diagram. The coloured dashed lines indicate the wt% of the sample and the expected relativ area, while the black dashed lines shows the course calculated with the proposed model for the samples containing 70 and 90 wt%.

The eutectic concentration is completely liquid above T_E and thus the peak can only be observed at two temperatures, but its intensity is slightly lower than expected, probably due to the presence of many ice crystallites disturbing the PEG crystals. While the 90 wt% sample starts to deviate slightly at high temperatures, the 70 wt% sample shows a strong drop in intensity after crossing the eutectic temperature and then it gradually declines further. This process can be described with the proposed assumption of a continuing melting process, where with increasing temperature more and more PEG1500 can be dissolved in water until the crystal completely disappears above T_L. The weight fraction of solid PEG present in the entire sample can be calculated using equation 2.22.

The parameters in equation 2.22 are set to the ones obtained from the fit to the DSC data and the equation needs to be inverted in order to obtain a volume fraction of liquid PEG1500 at a certain temperature. This inversion is only possible, if the logarithmic term in the equation is set to zero. Adjusting the equation in that way does not change its course significantly and thus is a sensible approach. The weight fraction of solid PEG can then be calculated:

$$w_{PEG,solid} = \frac{m_{PEG,solid}}{m_{PEG,solid} + m_{PEG,liquid} + m_{water}} \tag{4.4}$$

Since the entire water is liquid above T_E and the liquid PEG form a homogeneous liquid with it, while the solid PEG remains in crystalline form, the weight fraction of solid PEG can be calculated to:

$$w_{PEG,solid} = \frac{w_{PEG} - w_{PEG,liquid}}{1 - w_{PEG,liquid}} \tag{4.5}$$

Where w_{PEG} is the weight fraction of PEG in the entire sample and $w_{PEG,liquid}$ can be obtained from the inverted equation 2.22. The results from this calculations are represented by the dashed lines in figure 4.14 and describe the behaviour of the sample with 70 wt% very well. The sample with 90 wt% is not as well described, probably due to a sharper melting process as seen in the DSC data and some water could also have evaporated, causing the real wt% to be above 90 %. These results illustrate why the melting point depression derived by the Flory Huggins theory describes the obtained data very well. Water and PEG mixtures do not form any solid solution, but instead both components separate into pure crystals. Upon heating a liquid solution with the eutectic concentration forms. Increasing the temperature further causes more and more of the remaining crystal to be dissolved until the temperature is high enough, so that the remaining crystal can

be dissolved at once. Such a behaviour can be very well described with the assumptions made in the Flory Huggins theory.

Comparing the WAXS data from the polyethylene glycol dimethyl ether PEGDME1650 with the scattering curve obtained for PEG1500 shows no significant difference between the two samples. This is displayed in figure 4.15. Due to this equality there is no need to calculate a new model for the pure PEGDME with "POWDER CELL", instead the same model as for PEG1500 will be used to compare the data of the mixtures with water.

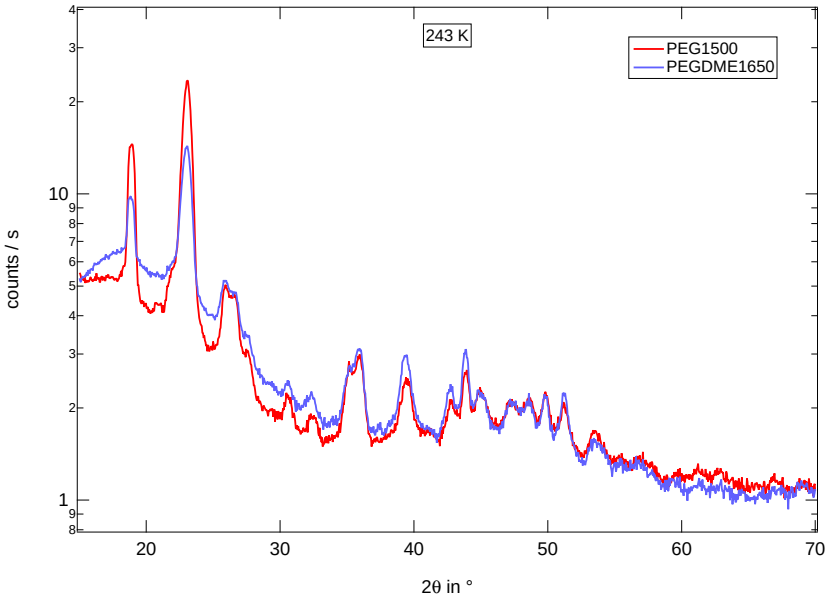

Figure 4.15.: Comparison between the WAXS measurements of PEG1500 and PEGDME1650 at 243 K.

Since the pure PEGDME1650 shows no difference to PEG1500 in the scattering data it is not surprising that the PEGDME1650 mixtures with water exhibit the same behaviour as the PEG1500 water mixtures. This is illustrated in figures 4.16 and 4.17. Again below the eutectic temperature the scattering profile exhibits peaks that can all be associated with pure hexagonal ice or pure PEGDME1650 and above T_E only a pure crystal of the major phase remains. In addition the disappearance of hexagonal ice peaks for the samples containing between 10 and 50 wt% PEGDME1650 can also be seen again. Due to these many similarities the fact that below T_E the mixtures can again be described by adding the appropriate fractions of the pure scattering curves together will not be illustrated here.

Instead the [120] PEG peak of PEGDME rich samples will be analysed directly in figure 4.18. Here the results differ strongly from the results obtained for PEG1500 water mixtures. While the pure PEGDME1650 again is around one for every temperature, the other concentrations deviate strongly from the expected relative peak areas. These deviations are very interesting, since the sample containing 90 wt% lies far below the expectation, while the sample with 70 wt% PEGDME1650 lies far above the expectation and the eutectic concentration sample comes down again, but is still above the expected value.

This indicates a preferred growth direction as seen for water rich mixtures that is dependent on the concentration of PEGDME1650. By decreasing the concentra-

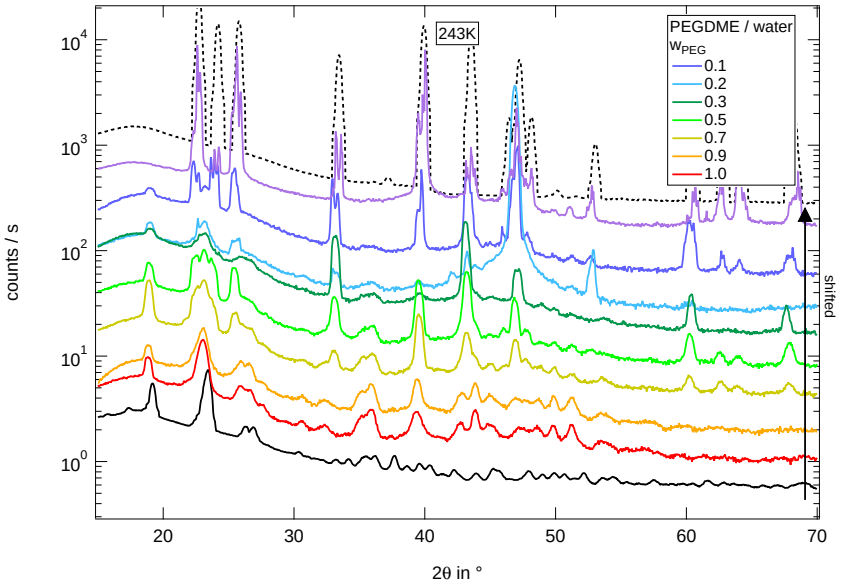

Figure 4.16.: WAXS measurements for samples containing different wt% PEGDME1650 at 243 K. The dashed black line shows the theoretical hexagonal ice and the black line the theoretical PEGDME1650 scattering curve. The curves are shifted for clarity with the same multiplication factor.

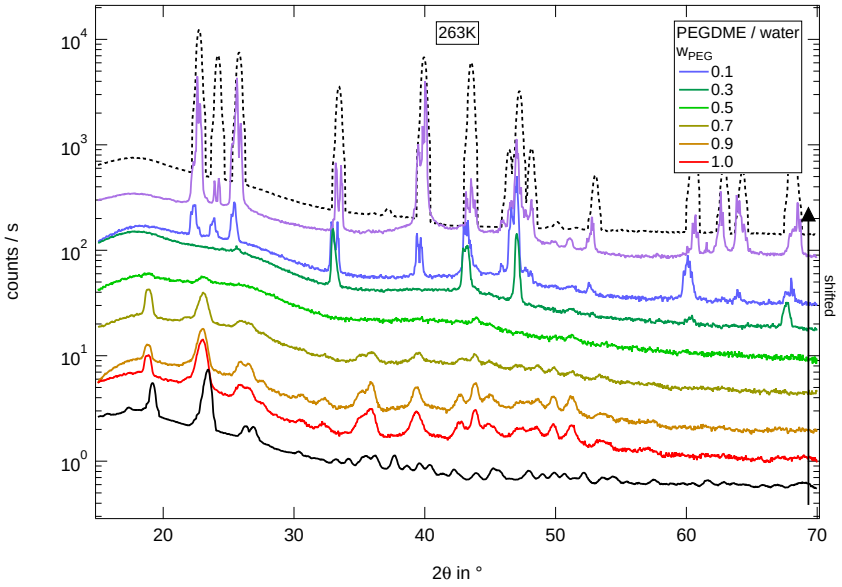

Figure 4.17.: WAXS measurements for samples containing different wt% PEGDME1650 at 263 K. The dashed black line shows the theoretical hexagonal ice and the black line the theoretical PEGDME1650 scattering curve. The curves are shifted for clarity with the same multiplication factor.

tion of PEGDME1650 the [120] direction seems to get hindered, but further decreasing the concentration then promotes growth in the [120] direction, before a further decrease hinders it again. This is very interesting behaviour and will be analysed further with SAXS measurements. The overall course of the curves remains the same however still indicating a continuous melting process in place of a sharp one.

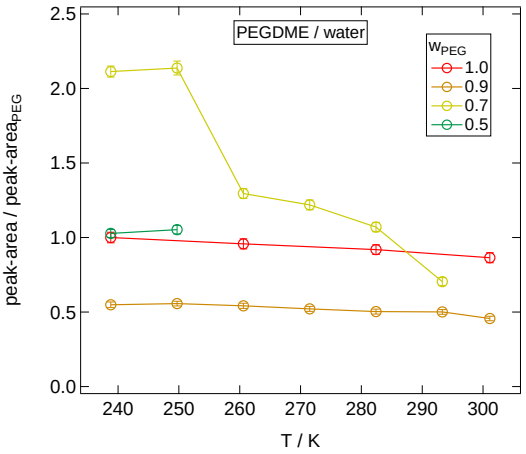

Figure 4.18.: Normalised peak area of the [120] PEG peak appearing in samples of the PEGDME rich side of the phase diagram.

So the only observable difference between WAXS measurements of PEG1500 water and PEGDME1650 water mixtures is the intensity change with concentration. All other discussed features and processes are the same regardless of the slightly different chain length or the end groups. So since the [120] PEGDME peak does not broaden significantly with increasing water concentration the peak intensity difference could be caused by the oscillation of the atoms around their equilibrium position. This is stated in the "Debye-Waller" factor [79] and might explain the measured intensity course.

The increased displacement due to the increasing temperature does not influence the scattered intensity, as can be seen in the constant intensity for the pure PEGDME at all temperatures and the decrease in intensity for the other samples can be explained with the continuous melting process. But at 243 K the intensity varies unexpectedly, which could indicate that at different compositions of water the displacement gets enhanced or depressed. Since the intensity is halved at 90% PEGDME and doubled at 70% PEGDME from the pure PEGDME this enhancement or depression must be very strong. This would be unusual, but could be an explanation for the observed behaviour.

4.3 Investigation of the Long Period and Crystallinity inside the Phase Diagram

Attempting to further characterise the crystallisation behaviour of the water polyethylene glycol mixtures, SAXS measurements are used to observe structures on a larger length scale than the unit cell. SAXS measurements yield the length of the long period d_{ac} of semi crystalline materials, which is the length of one amorphic unit d_a added to the length of a crystalline unit d_c. So the influence of the continuous melting process observed in WAXS measurements on the amorphous and crystalline regions of the semi crystalline polymer can be studied. These measurements might also reveal the reason why the intensity measured with the WAXS set up changes so differently for PEG1500 and PEGDME1650.

The samples are inserted into the sample holder while being in their homogeneous liquid phase and then the sample holder is brought into the SAXS set up. To ensure the same conditions for all measured samples, the sample is then heated to 333 K and then cooled to 208 K as fast as possible in the set up with around 20 K/min. Then a measurement is initiated for 30-45 minutes depending on the scattering signal of the sample, before heated to the next temperature for the next measurement. Again the increments are chosen appropriately in order to obtain sufficient measurements below T_E and between T_E and T_L. Pure PEG1500/PEGDME1650, and compositions containing 95 wt%, 90 wt%, 70 wt% and 50 wt% of PEG1500/PEGDME1650 are measured.

The data is then corrected with subtracting a constant background obtained by fitting a constant to the raw data at large q values. Figure 4.19 shows the SAXS data for PEG1500 and the sample containing 50 wt% PEG1500. For water mixed with PEG1500 the measured scattering curves display two pronounced peaks. The first peak at lower q exhibits a higher intensity and the second peak maximum is located exactly at two times the maximum position of the first peak. So the measured peaks can be associated with the long period d_{ac} of a lamellar structure [76] and this would make the peak at lower q is the first order peak and the peak at higher q is the second order peak. In figure 4.19 the background corrected data for PEG1500 at 253 K is displayed and compared to the scattering data of the sample containing 50 wt% PEG1500.

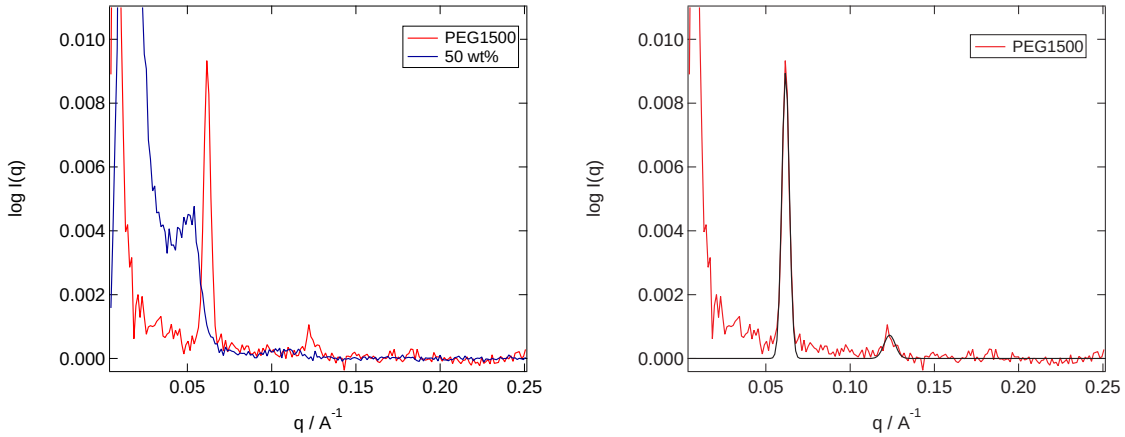

Figure 4.19.: Left: Comparison of SAXS data between PEG1500 and the sample with 50 wt% PEG1500 at 253 K. Right: Exemplary data of PEG1500 at 253 K. In black the fit of the sum of two Gaussian functions is displayed.

Both peaks shift to the left with increasing concentration of water in the sample and thus the observed structure becomes larger. So there definitely is an influence of water on the crystalline or amorphous PEG, although the water crystallises in a separate crystal, respectively the water should completely be in the liquid phase between T_E and T_L. Due to the shift to lower q the first order peak starts to vanish inside the peak of the primary beam and thus concentrations lower than 50 wt% do not yield evaluable scattering curves. To obtain the exact peak positions and also the peak height, the sum of two Gaussian function is fitted to the every sample at every temperature. Thereby both Gaussian functions level out to zero and the position of the second peak is set to two times the position of the first peak q_{max}. The right side of 4.19 shows an example of the fit to the data of pure PEG1500 at 253 K. It seems that the sum describes the data very well and can be used to evaluate the data further.

The long period of the semi crystalline structure present can be calculated by: [76]

$$d_{ac} = \frac{2\pi}{q_{max}} \tag{4.6}$$

Calculating the volume fraction of the amorphous or crystalline region becomes a little more complicated. In general the intensity at the maximum of the peaks is given by: [76]

$$I\left(n \cdot \frac{2\pi}{d_{ac}}\right) = N(\Delta\rho)^2 \frac{d^4}{n^4\pi^4} \frac{\sin(n\pi\phi)}{(\sigma_a^2 + \sigma_b^2)} \tag{4.7}$$

Where $\Delta\rho$ is the difference in scattering length density between the amorphous and crystalline phase, N is the number of lamella present, n is the order of the peak, σ_a and σ_b are the roughness of the amorphous and crystalline phase and ϕ is the volume fraction of either the amorphous or crystalline phase. Assuming a order independent roughness, the volume fraction ϕ can be calculated by dividing the intensity at the maximum of the first order with the intensity at the maximum of the second order:

$$\phi = \frac{\arccos\left(2\sqrt{I(2 \cdot q_{max})/I(q_{max})}\right)}{\pi} \tag{4.8}$$

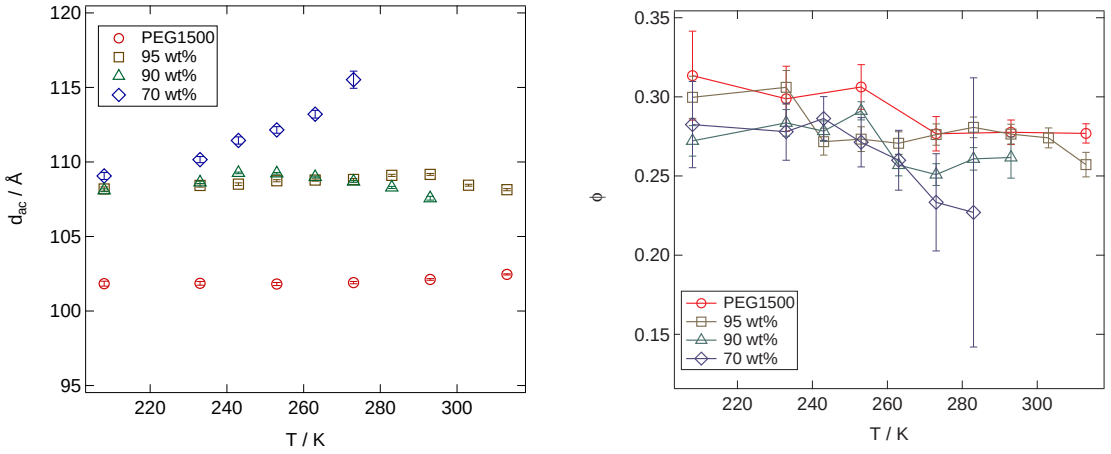

Figure 4.20.: Left: The long period d_{ac} for samples with different weight fractions and temperatures. Right: The volume fraction ϕ_a of the amorphous phase for samples with different weight fractions and temperatures.

The results for d_{ac} and ϕ are displayed in figure 4.20. While the long period for the mixtures is larger than for pure PEG1500, there is no change in d_{ac} with increasing temperature, except for the sample with 70 wt% PEG1500. These results suggest that adding water to PEG1500 increases the long period until a maximum increase is achieved. Adding more water to the mixture does not further increase the long period as the sample with 95 and 90 wt% exhibit the same d_{ac}. So the water molecules seemingly cause the PEG1500 chains to form thicker crystalline areas or increase the size of the amorphous phase or both, but an influence of the continuous melting can still only be seen for the 70 wt% sample, where the long period keeps increasing with increasing temperature. This suggest that a rearrangement of the PEG chains is not only caused by the surrounding ice/liquid water, but also by continuously dissolving more and more semi crystalline PEG into the water PEG solution. So increasing the temperature above T_E dos not only cause the PEG crystallites to decrease in size, but also allows them to rearrange themselves.

The volume fraction calculated by the introduced method is below 0.5 for all investigated samples and temperatures. Since the crystallinity of pure PEG1500 is very high, the obtained volume fraction yields the fraction of the amorphous phase ϕ_a. For low temperatures the ϕ_a remains constant with increasing temperature and changing concentration. It remains this way for samples containing high amounts of PEG1500, while there is significant drop in ϕ_a for the sample containing 70 wt% PEG1500. This further supports the claim of a continuous melting process, that dissolves more and more of the amorphous phase of the semi crystalline PEG1500 in the water PEG1500 solution. Still it is surprising that the addition of water to pure PEG1500 does not increase the volume fraction of the amorphous phase. So it is necessary to investigate the thickness of the amorphous phase d_a, by calculating it via:

$$d_a = d_{ac} \cdot \phi_a \tag{4.9}$$

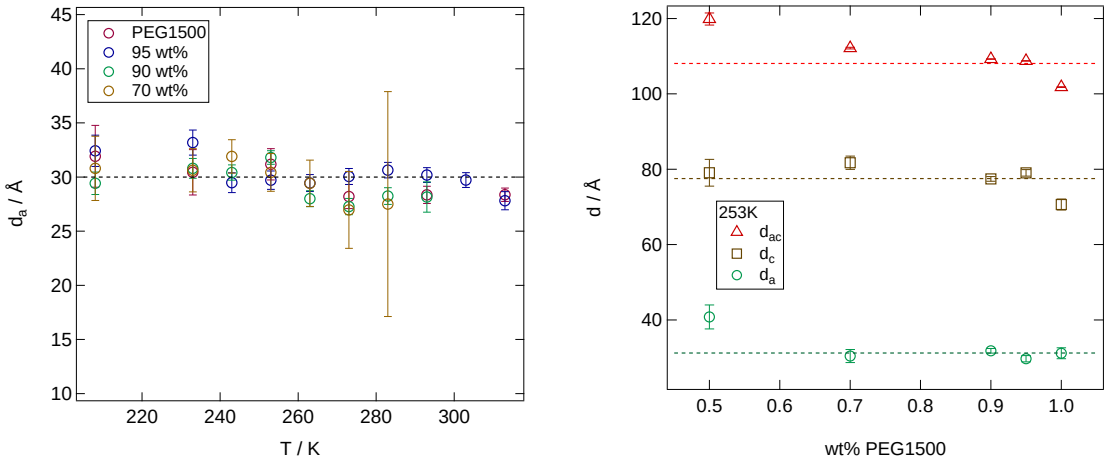

Figure 4.21.: Left: The thickness of the amorphous phase d_a for samples with different weight fractions and temperatures. Right: The long period, thickness of the crystalline phase d_c and the thickness of the amorphous phase d_a at 253 K for all measured wt% of PEG1500. The dashed lines are guides for the eye.

The calculated length d_a is displayed on the left side of figure 4.21. There is no influence of temperature or concentration on the thickness of the amorphous phase. So not only is the decrease in ϕ_a compensated by the increase in d_{ac}, it also means that the increasing long period is caused by an increase in the thickness of the crystalline phase (since $d_c = d_{ac} - d_a$). So d_c shows the same behaviour as d_{ac} and the melting process taking place inside water PEG1500 mixtures with a wt% above the eutectic concentration can be described. First adding water in general increases the length of the crystalline phase to a certain extent. The surrounding water molecules enable the PEG1500 chains to form thicker semi crystalline lamellae than in the pure PEG1500. The amorphous region of the semi crystalline polymer remains unchanged by water, further supporting the picture of water molecules surrounding the PEG crystal rather than penetrating it, since the water would then most likely swell the amorphous region, because WAXS measurements ruled out a solid solution containing water and PEG1500. Upon heating above the eutectic temperature more and more PEG1500 molecules contained in the semi crystalline phase start dissolving in the liquid water PEG1500 solution instead. The data shows

that thereby the volume fraction of the amorphous phase decreases, meaning that more molecules from the amorphous phase get dissolved than from the crystalline phase. Still also crystalline parts need to be dissolved, otherwise the intensity observed in WAXS measurements would need to stay the same instead of decreasing. The solvation of amorphous and crystalline molecules in the liquid phase enables a further increase of the crystalline lamellar thickness. So while some PEG1500 chains get dissolved in the liquid phase, the chains remaining in the semi crystalline phase start to rearrange, accommodating their new environment.

The right side of figure 4.21 illustrates how d_{ac} and d_c behave the same when adding water to PEG1500, while d_a remains constant. This behaviour can be observed for all temperatures, the only difference would be the increase achieved when going from 90 to 70 wt%, because this increase is highly dependent on temperature. Further illustrating the melting and rearranging processes described above. 253 K was chosen as displayed temperature, because only at 253 K and 243 K the peaks of the sample containing 50 wt% PEG1500 could be evaluated, but still show deviations from the described behaviour.

So SAXS measurements yielded important information on the melting process taking place in water and PEG1500 mixtures and might also help in understanding the curious intensity course of water PEGDME1650 mixtures seen in the WAXS measurements. Therefore water and PEGDME1650 mixtures are also measured and exemplary results are shown in figure 4.22. The data for the PEGDME1650 mixtures looks very different from

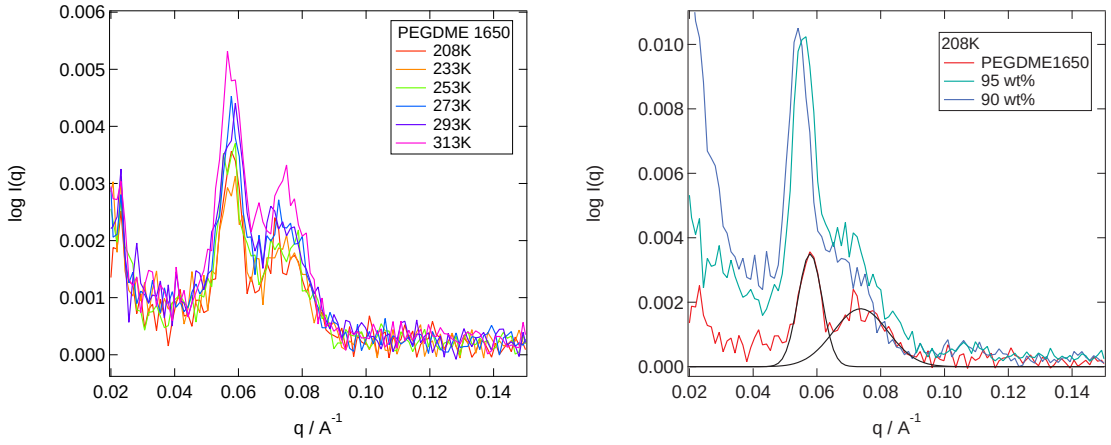

Figure 4.22.: Left: SAXS data of pure PEGDME1650 at different temperatures. Right: Comparison of SAXS data of samples with varying wt% of PEGDME1650 at 208 K

the PEG1500 mixtures. There is no second order peak, but instead the first order peak seems to have split into two peaks that show a maximum around q_{max} from the PEG1500 mixtures. Both peaks increase in intensity with increasing temperature at about same rate. Adding water to the PEGDME1650 seems to favour adding to the larger observed structure, since the first peak increases largely in intensity for the mixtures containing 90 and 95 wt% PEGDME1650, while the second peak becomes almost indeterminable. This "peak splitting" is highly unexpected and is probably due to the existence of two different species of polymer chains. This could also be seen in the melting peak of the DSC measurement of the pure PEGDME1650. This would create two different structures in the sample. The thicker structure increases highly when adding water.

Still the two peaks can be fitted with individual Gaussian functions in order to obtain the d_{ac} of the observed structures. The results of this analysis is displayed in figure 4.23. Just like the d_{ac} of the water PEG1500 mixtures the long periods of both peaks do not change with temperature, but with increasing concentration of water the long period $d_{ac,2}$ increases in size.

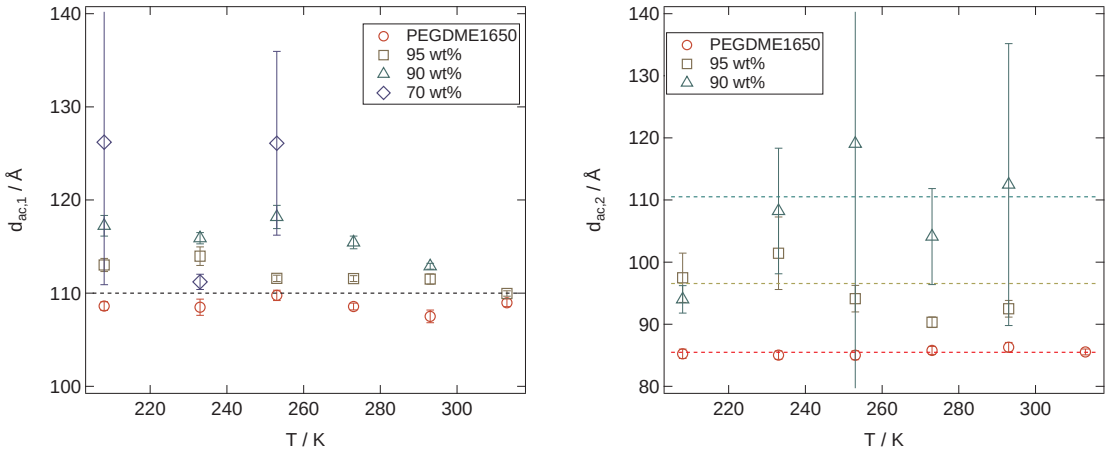

Figure 4.23.: Left: The long period $d_{ac,1}$ of the peak at lower q for samples with varying weight fractions at different temperatures. Right: The long period $d_{ac,2}$ of the peak at higher q for samples with varying weight fractions at different temperatures.

The only implied increase with temperature can be seen for $d_{ac,1}$ of the sample with 70 wt% PEGDME1650, again due to the continuous melting process already mentioned and explained above, but due to the weak intensity and the primary beam peak the data is very uncertain. Since this is the same as for the PEG1500 and water mixtures it can not explain the difference in relative intensity of the [120] PEG peak. So it seems that the appearance of two possible different structures causes the PEGDME1650 crystal to change its preferred growth direction depending on the amount of surrounding water. Adding small amounts of water seems to block growth in the [120] direction, because the relative intensity is far below the expected one, but increasing the amount of water then causes the [120] direction to be the preferred one and the relative intensity increases above the intensity of the pure PEGDME1650. Increasing the amount of water in the sample starts to block that direction again and the intensity drops again. This is related to the two structures observed in SAXS measurements and probably is a result of two different species of polymer chain. Figure 4.24 further illustrates this interpretation by depicting the obtained long periods for the two peaks observed in water PEGDME1650 and comparing it to the d_{ac} of the water PEG1500 mixtures at 208 K and 233 K. The results further show how the PEGDME1650 mixtures behave like the PEG1500 mixtures and that the difference is found in the formation of two structures instead of one. One with smaller and one with larger lamellae than the PEG1500 mixtures.

Summary of the Crystallisation and Melting Processes

Results in this chapter showed that water and PEG1500 or PEGDME1650 mixtures both form eutectic systems with the same eutectic concentration. Cooling the mixture causes a

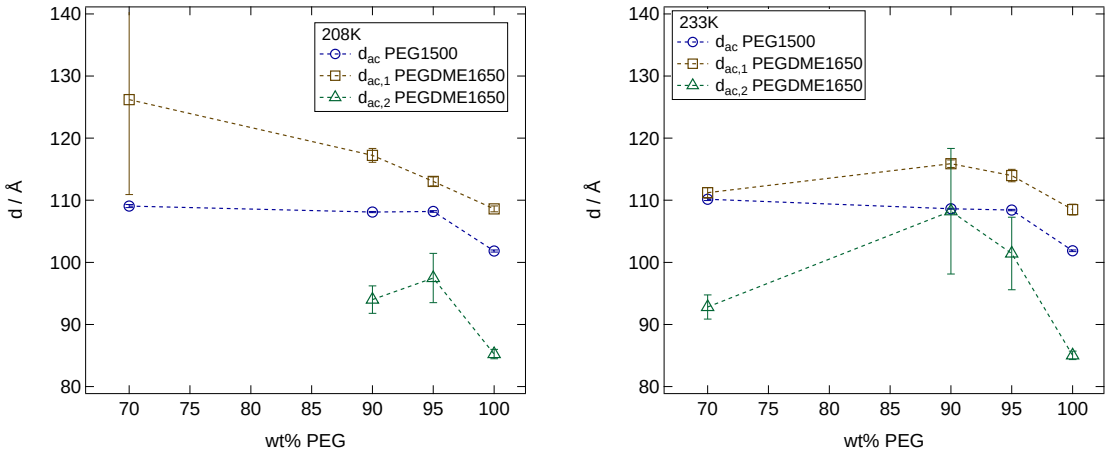

Figure 4.24.: Left: Comparison between $d_{ac,1}$,$d_{ac,2}$ and d_{ac} from PEG1500 mixtures at 208 K for varying concentrations. Right: Comparison between $d_{ac,1}$,$d_{ac,2}$ and d_{ac} from PEG1500 mixtures at 233 K for varying concentrations.

pure crystal of the major phase to appear and grow below T_L. The melting point depression caused by mixing the water and polymer together can be described by the Flory Huggins theory and found a change from an attractive interaction parameter for PEG1500 to a repulsive one for PEGDME1650. WAXS measurements revealed that there is a preferred growth direction for the hexagonal ice crystals, if the concentration of the surrounding liquid polyethylene glycol is high enough to block the other direction for ice crystals. On the polymer rich side such a preferred growth direction can only be found for the PEGDME1650 samples and this is probably due to the appearance of two lamellar structures instead of one. Below T_E the remaining liquid mixture separates into pure crystallites of the two components, but this separation is very slow and can be stopped by cooling the mixture fast enough to achieve a glassy state. Upon heating a cold crystallisation takes place completing the crystallisation of the mixture. Due to the larger endgroups, mixtures containing PEGDME1650 exhibit a faster separation when compared to PEG1500 and a higher eutectic temperature. Upon heating the sample above T_E a liquid phase with the eutectic concentration forms and a further increase in temperature causes more and more of the pure crystal of the major phase to dissolve into the liquid phase in a continuous melting process. This causes the crystalline lamellae of the remaining crystal to thicken, because the polymer chains can rearrange in their changing environment.

5 The Interplay between Polyethylene Glycol and the AOT Surfactant Shell

Loaded microemulsion droplets have a variety of applications, for example in drug delivery or in researching the behaviour of biomolecules inside a cell like confinement. Thus it is very important to understand the interaction between the molecule inside the droplet and the surfactant shell. Not only may the conformation of the molecule be changed by the confinement, but the size or stability of the confinement may also be drastically changed by the molecule inside.

The influence of molecules inside the core of microemulsions droplets on the surfactant shell has been extensively studied. There is the chance of a strong interaction between the surfactant shell and the polymer inside the droplet. For PEG dissolved in water/AOT/oil microemulsions an attractive interaction between PEG and AOT has been proposed, causing the polymer to adsorb at the AOT shell [18,22,47,93]. In order to investigate the influence of polyethylene glycol on the percolation temperature of water/AOT/octane microemulsions, polyethylene glycol with different molecular weight and different chain ends is inserted into the water core. Here the parameter $Z = \frac{\text{chains}}{\text{droplet}}$ is introduced, giving the average number of polymer chains per microemulsion droplet. The percolation temperature and the droplet radius at that temperature have to be determined, before the bending modulus can be calculated. Thus first the percolation temperatures of the microemulsions will be measured by dielectric spectroscopy and then investigated by SAXS to obtain the droplet radius in dependence on temperature. In the following all microemulsions loaded with polyethylene glycol will have a volume fraction $\phi = 0.3$ unless stated otherwise.

5.1 The Influence of Chain Length on the Percolation Temperature

Dielectric spectroscopy is a well proven technique that enables the determination of percolation and critical temperatures of microemlusions in the droplet phase [20,23,25,48]. Figure 5.1 shows how the percolation temperature is obtained. The real part of the conductivity is measured over increasing temperature at 10 kHz. At this frequency the measured signal is not corrupted by electrode polarisation or dielectric relaxations [20]. At low temperatures the conductivity is very low, but with increasing temperature the conductivity increases by several orders of magnitude, before reaching a plateau value. The temperature closest to the inflection point of the large increase is taken as the percolation temperature T_p [20,25,48]. The critical temperature T_c is the temperature at which the conductivity collapses again [20,25,48]. It can be seen that there is no collapse in the measured data and some samples

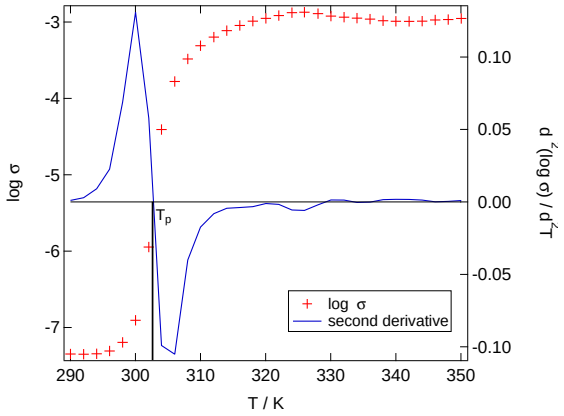

Figure 5.1.: Examplary conductivity measurement of a Water/AOT/octane microemulsion. The logarithmic conducitivity as well as the second derivative in regard to temperature are shown. The first root of the derivative is the percolation temperature.

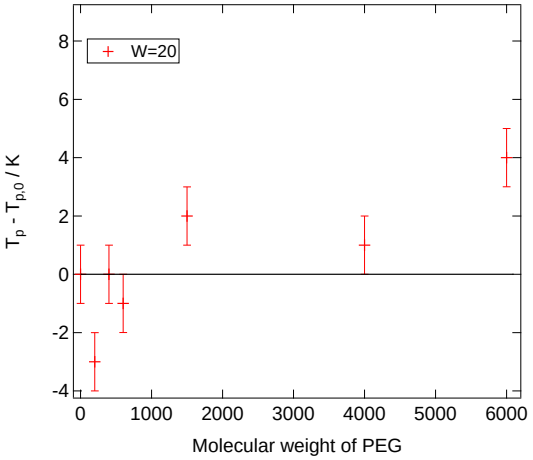

Figure 5.2.: The change in percolation temperature in dependence on the molecular weight of the PEG chain inside for droplets with $w = 20$. For $w = 20$ the microemulsion containing PEG12000 was not stable and thus could not be measured.

do not show any decrease in conductivity for high temperatures, but instead a constant plateau value, probably due to a very stable droplet phase. So the critical temperature can not be reliably determined for the samples investigated in this work. The temperature was varied in steps of 2 Kelvin so the uncertainty of T_p is estimated to be 0.5 K.

Microemulsions with $w = 20; 30; 40$ containing different Z of polyethylene glycol chains were investigated in this work. The molecular weight of the polymer chain was 200, 400, 600, 1500, 4000, 6000 and 12000 g/mol for PEG to study the effect this increase in size has on the percolation temperature.

Since the high molecular weight polymer chains are rather large when compared to the droplet radius, the microemulsion with $w = 20$ containing PEG12000 was already percolated in its droplet phase. Thus the percolation temperature of the particular microemulsion could not be determined. For every other microemulsion the percolation temperature could be obtained as shown in figure 5.1 and the result for $w = 20$ microemulsions is shown in figure 5.2, where the difference in percolation temperature is shown as a function of the molecular weight of the polymer. $T_{p,0}$ is the percolation temperature of a $w = 20$ microemulsion containing no polymer. By adding a small PEG chain (PEG200) into the droplet, the percolation temperature decreases at first. Increasing the polymer chain length increases the percolation temperature again, so that there is no difference between the loaded and empty microemulsion. A further increase in chain length (PEG1500) then causes the percolation temperature to rise above the empty microemulsion and then every increase in chain length causes an increase of the percolation temperature.

This behaviour has already been observed [23,94,95]. The decrease caused by small chains is attributed to a "wedging effect" [23,96,97], where the PEG inserts itself between two AOT head groups, due to an attractive interaction between the PEG and the AOT. The PEG200 chain is so small that the wedge part of the molecule takes up the entire chain, causing

a destabilising effect on the droplet surfactant shell. So the percolation temperature decreases. Longer PEG chains will also wedge between two head groups, but there will be a part of the polymer chain that does not fit between the head groups and instead will adsorb at the water core-surfactant interface. This adsorption has a stabilising effect that cancels the destabilising effect and thus the percolation temperature is the same as for the unloaded microemulsion. This stabilising effect increases with increasing chain length of PEG, while the destabilising is unaffected by it, even if the chain is long enough to provide a second wedge with its second end group. So the percolation temperature increases further with longer PEG chains. The chain length at which a stabilisation in comparison to the unloaded microemulsion, as well as the size of the increase in percolation temperature depend on the ratio of the droplet radius to the polymer size. This can be seen in figure 5.3. Here microemulsions with $w = 30$ and $w = 40$ are loaded with the same PEG chains as the $w = 20$ microemulsion.

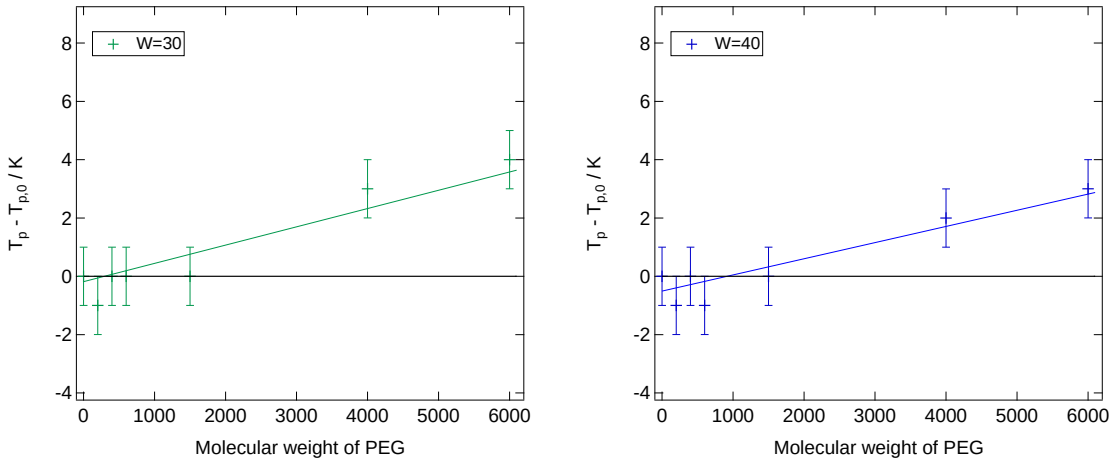

Figure 5.3.: The change in percolation temperature in dependence on the molecular weight of the PEG chain inside for droplets with $w = 30$(left) and $w = 40$ (right).

The droplet radius of these microemulsion is now too large, as that one PEG200 wedge could cause a measurable destabilisation. But the stabilisation effect is also reduced and the chain length must be increased further before a stabilisation effect can be measured. When the chains are long enough the increase in percolation temperature seems to be linear with molecular weight, but it can bee seen that a line fit to the increases temperatures would intersect with the zero line at a molecular weight where no increase in percolation temperature can be found. Thus it would not yield the "critical" chain length at which an increase in T_p would occur. Another interesting fact is that for smaller droplets the increase in T_p caused by long enough chains is larger as for larger droplets, allowing for the assumption that to stabilise the larger droplets significantly, larger PEG chains are needed than for smaller droplets and that the stabilisation effect in turn is smaller. This is also illustrated in figure 5.4, where the difference in percolation temperature is shown for all molecular weights of PEG used in this work over the parameter w. PEG200 only decreases the percolation temperature of the smallest investigated droplet size. Larger droplets do not show any change due to PEG200. PEG400 and PEG600 polymer chains do not influence the percolation temperature in comparison to the unloaded microemulsion.

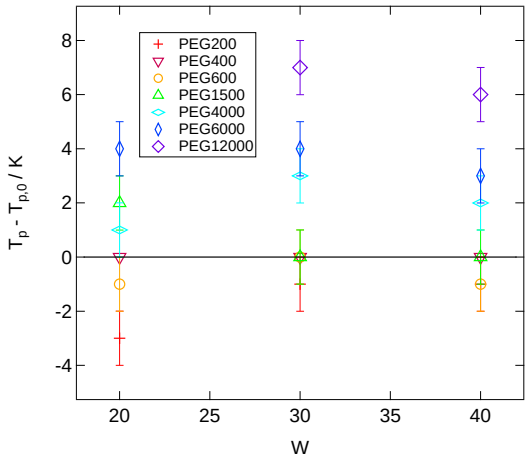

Figure 5.4.: Difference in percolation temperature T_p for all molecular weights of PEG.

For $w = 20$ this is because the additional monomers stabilise the droplet and thus cancel the destabilising, while for larger droplets there is no measurable stabilisation, due to the size of the droplet. Further supporting this is the fact that PEG1500 stabilises the $w = 20$ microemulsion, but has no effect on the larger droplets. Higher molecular weight stabilises all droplet sizes and it seems that smaller droplets become more stabilized than larger droplets, since the polymer can adsorb to a higher percentage of surfactant molecules. There is also no difference between the stabilisation of the $w = 20$ and the $w = 30$ microemulsions. Assuming the droplet radius to be $1.4 \cdot w$ and the area a monomer of PEG can cover to be $30\,\text{Å}^2$ [20,69], this suggests that after the polymer covers about 25% of surfactant interface an even further increase in that percentage does not further stabilise the droplet.

5.2 Varying the Number of PEG Chains Inside the Droplet

Up until now we only considered one molecule per microemulsion droplet, allowing for one to two wedges per droplet, depending on the size of the polymer chain. Leaving the question what would happen, if the number of wedges is increased. So the focus shifts from the droplet and polymer size to the number of polymers inside the droplet, the following investigation will concern itself only with $\phi = 0.3$ and $w = 30$ microemulsions. Figure 5.5 shows how the percolation temperature changes by increasing the number of PEG200 chains inside the microemulsion droplets and compares it to the already discussed change with one chain per droplet that increases in size. The number of monomers and thus the surface area covered by PEG, seems not be the deciding parameter, if the droplet is stabilised or destabilised, because 60 PEG200 chains have about the same number of monomers as one PEG12000 chain, but increasing the number of PEG200 chains instead of the molecular weight of the polymer has the opposite effect on the percolation temperature. So the number of chains and how many monomers are connected with each other seem to be the more influencing parameters. This works very well with the wedge idea. PEG200 loaded droplets with a very low Z show no significant difference to the unloaded droplet when looking at the percolation temperature, since the number of wedges between AOT head groups is too small to destabilise the droplet. Increasing the number of PEG200 chains lowers the percolation temperature, because there are more and more

wedges [23,94,95]. Structural investigations are necessary to determine, if there is a number of wedges that is too high to maintain the droplet structure.

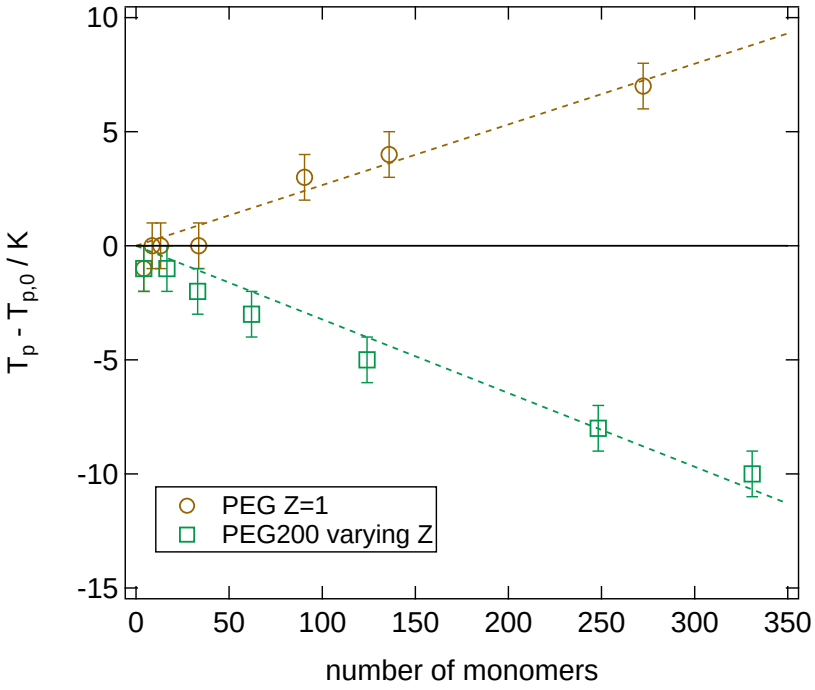

Figure 5.5.: Change in T_p for one chain chain per droplet increasing with increasing molecular weight (yellow) and for varying number of chains of PEG200 in the droplet (green). The droplets have $w = 30$. The dotted lines are guides for the eyes and represent a line fit.

So it seems to be highly interesting to investigate different amounts of PEG chains per droplets as well as varying the chain length. Figure 5.6 shows the result of such a study. On the left side it can be seen how increasing the number of PEG1500 chains influences the percolation temperature. While a small Z once again does not influence the stability of the droplet, increasing Z causes the droplet to stabilise. As already discussed now the wedge has a "tail" that adsorbs at the surfactant interface outweighing the destabilisation caused by the wedges. But increasing the number of PEG1500 chains even further has no additional stabilising effect, which has also been found by Schübel et al. [23]. There it was reported that increasing the number of medium length PEG beyond the number investigated here, would start to decrease the percolation temperature. Thus there seem to be four Z regimes possible, depending on the size of the droplet and the PEG chain. First for small enough chains, low Z and large enough droplets the percolation temperature is unaffected by addition of polymer. Then, if the chain is not too small, the increase in Z stabilises the droplet up until a certain point. After that adding more polymer has no effect again, since now the possible increase in stabilisation is countered by a sufficient number of wedges introduced into the system. Increasing the number of polymer chains per droplet again then causes the droplet to destabilise, since now the number of wedges outweighs the stabilisation caused by the tails of the wedges.
This interpretation is even further supported by the right side of figure 5.6. There the influence of increasing chain length while decreasing Z on T_p is pictured. Starting with

PEG200 $Z = 60$ and going to PEG400 $Z = 30$ there seems to be no stabilising effect by the increase in chain length, since T_p is about the same for PEG400 $Z = 30$ and PEG200 $Z = 30$ (124 monomers of PEG200), both providing the same number of wedges. Meaning that the tail provided by PEG400 is not long enough to cause a stabilisation. Continuing to increase the PEG in size to PEG600 $Z = 20$ shows first stabilisation effects. By crossing a certain threshold of chain length to wedge ratio the stabilisation effect becomes stronger than the destabilisation caused by the number of wedges. There also seems to be an upper limit of stabilisation caused by PEG chain size, since three PEG400, two PEG6000 and one PEG12000 chain inside the droplet cause the same increase in percolation temperature.

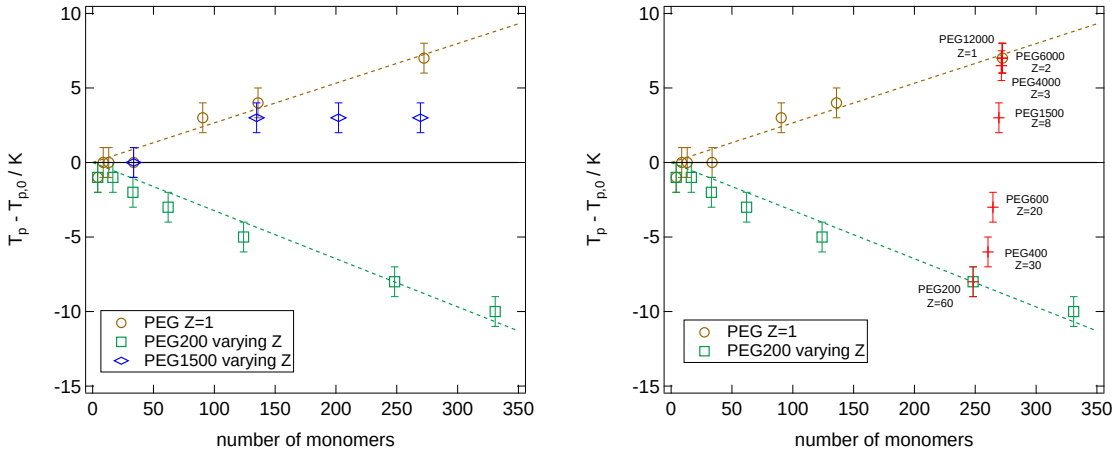

Figure 5.6.: Left: Influence of increasing number of PEG1500 chains on percolation temperature. Right: Infleunce of increasing chain length and simultaneously decreasing number of chains per droplet.

5.3 Comparison Between Different End Groups

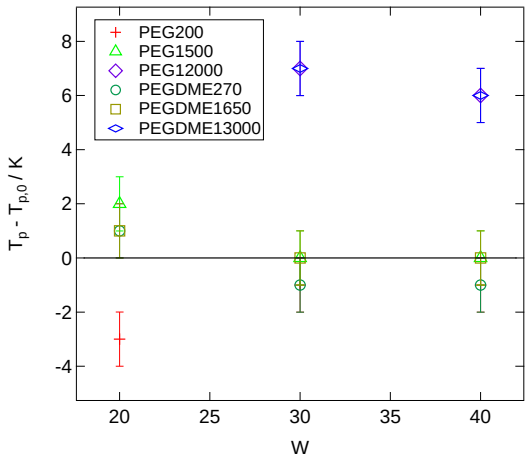

Figure 5.7.: Comparison of the influence of percolation temperature between the used PEGDME and PEG of comparable molecular weight for all used droplet sizes containing one polymer chain.

Since there is an attractive interaction between PEG and the AOT[18,22,47,93], it is interesting to study, whether exchanging the hydrogen atom of the -OH end group with a -OCH_3 group changes the interaction and therefore the influence of the polymer on the percolation temperature. So now the microemulsions are loaded with PEGDME with a molecular weight of 200 g/mol, 1650 g/mol and 13000 g/mol in order to be comparable to PEG200, PEG1500 and PEG12000. The changes to the influence on the percolation temperature can be seen in figure 5.7, where T_p for all droplet sizes containing one polymer chains is shown.

There is no difference in percolation temperature between PEG1500 and PEGDME1650,

indicating that PEGDME also exhibits an attractive interaction with AOT, adsorbing at the surfactant interface and thus stabilising the droplet. The addition of about three monomers is not large enough to further stabilise the droplet and so there is no difference between PEG and PEGDME. Between PEGDME13000 and PEG12000 also no difference can be measured. The microemulsion $w = 20$ containing one chain of PEGDME13000 was already percolated and so T_p could not be determined. For larger droplets PEGDME13000 also stabilises the droplet, but not more than PEG12000. Since now the increase in monomers is about 20 there could be a further stabilisation, recalling the almost linear increase with molecular weight for droplets containing PEG. This would further support the assumption that there is a maximum stabilisation and further increasing the molecular weight of the polymer chain has no further increase in T_p as consequence. For PEGDME270 there is a key difference to PEG200. While there, too, is no influence on the percolation temperature for the larger droplets, there is also no decrease in percolation temperature for the smallest droplet size. Suggesting that for every droplet radius there is an ideal wedge size, where the decrease in T_p is maximal and even a slight increase in size starts to stabilise the droplet again. This is further supported by studying the influence of increasing Z with PEGDME270 on microemulsions with $w = 30$. Figure 5.8 shows that with increasing number of PEGDME270 chains per droplet the percolation temperature decreases drastically and even further than for droplets containing more PEG200 chains. So it seems it is not only important at which number of monomers the wedge also has a stabilising tail, but also below which number of monomers the wedge is not large enough to reach the maximum destabilisation of the droplet. It could also be assumed that the larger end group of the PEGDME is responsible for the greater decrease in T_p, but then the microemulsion with $w = 20$ and one polymer chain PEGDME270 should also destabilise the droplet and not show no effect, since PEG200 destabilises the droplet.

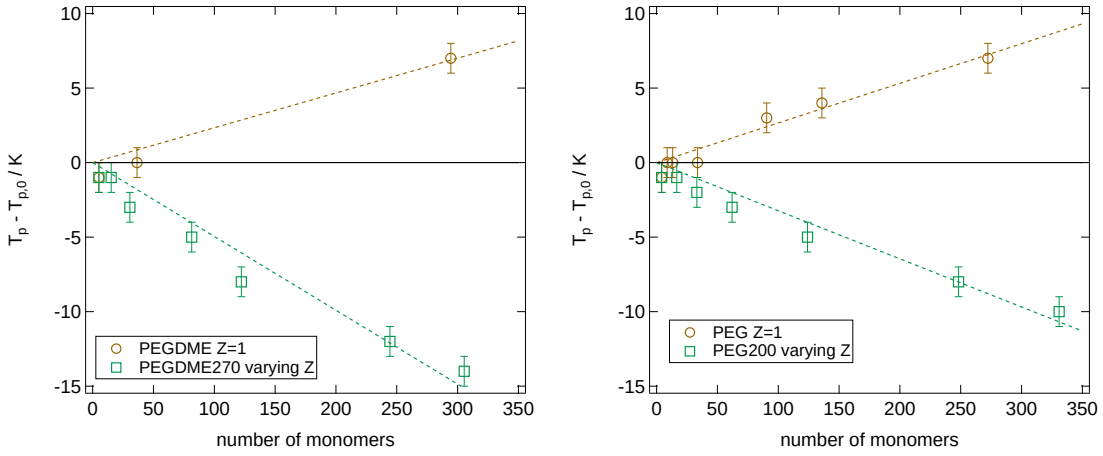

Figure 5.8.: Left: Change in T_p for one chain chain per droplet increasing in size (yellow) and for varying number of chain of PEGDME270 in the droplet (green). The dotted lines are guides for the eyes and represent a line fit. Right: see figure 5.5

So not only is a certain number of wedges needed to eventual counter stabilisation effects caused by the tail of longer chains, but also more wedges are needed, if the polymer chain is too small to completely wedge itself between two AOT head groups. At a certain chain length the destabilisation effect reaches its maximum and further increase in the

chain length starts to stabilise the droplet again. Since the same effects can bee seen for PEG and PEGDME chains with no difference between the different chain ends for certain droplet sizes and differences can be explained inside the wedge model, there seems to be no significant change in the interaction between PEGDME with AOT and PEG with AOT.

5.4 The Influence of Polyethylene Glycol on the Radius of the Water Core of W/A/O Microemulsions

Since the addition of polyethylene glycol influences the percolation temperature depending on polymer size and chain ends, it is interesting to study, if the droplet radius is effected by the polymer addition as well or if the radius of the droplet is unaffected and the change in the bending modulus is only caused by the difference of T_p. Taking the wedge model into account it would be expected that the radius of droplets with small and many PEG chains is larger than the unloaded droplet radius, due to the wedges. For larger polymer chains the stabilisation induced by the polymer could lead to smaller droplet radii, because the polymer chain binds the head groups closer together. In order to investigate the droplet radii, SAXS measurements are used. The microemulsions are studied at different temperatures, where the temperature range starts at 10 K or 11 K below the percolation temperature of the microemulsion and increases in steps of 2 K until it reaches 6 K or 5 K above the percolation temperature. This is done in order to investigate the transition from below to above T_p and also to be able to compare equal temperatures.
After the measurements have been done, the temperature of the SAXS set up and the temperature of the BDS set up need to be compared, because they may not be exactly the same, leading to a different T_p in both set ups. Therefore the liquid crystals 5CB and E7 are studied in both systems, since their transitions from the nematic to the isotropic phase takes place at a well defined temperature and can be observed in both experimental set ups. In SAXS measurements the correlation peak of the nematic ordering disappears at the transition temperature, while they lose their preferred orientation, which can be seen via BDS. The transition temperature of 5CB is at 36 °C and for E7 at 60 °C.

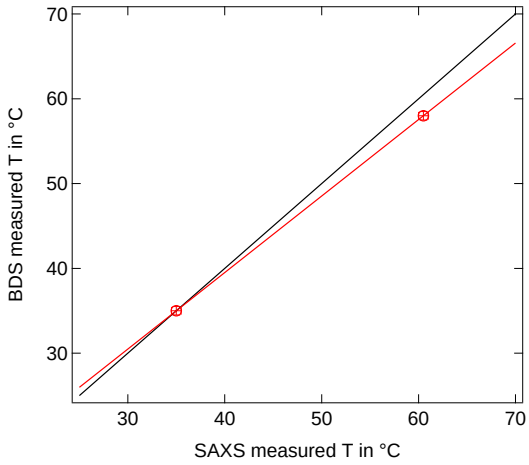

Figure 5.9.: The nematic to isotropic transition temperature of 5CB and E7 liquid crystals measured by BDS and SAXS.

Figure 5.9 shows the measured transition temperatures from BDS and SAXS. The black line indicates the bisecting and both data points should lie on it, if the measured temperatures in both set ups were identical. This is only the case for the transition of 5CB, while the temperature of the E7 transition is different. A linear temperature drift is assumed and fitted with the red line. The red line crosses the bisecting at 35 °C, where the 5CB transition was measured in both set ups. Since the temperature range of the experiment is from 13 °C to 49 °C this calibration seems reasonable, because it includes the intersection point between bisecting and linear fit, and the deviation from the bisecting is very small.
Both set ups show the same result for the 5CB transition, which lies in the observed temperature range. Since the percolation temperatures were already discussed in great

detail and the deviations between both set ups are not high in the observed range, the SAXS temperatures will be corrected here in order to match the T_p observed via BDS.
Exemplary measurement results for the unloaded microemulsion and the microemulsion containing one chain of PEGDME13000 are shown in figure 5.10. The decrease proportional to q^{-4} followed by a minimum and a shoulder exhibited by the scattering curves are typical for the core-shell form factor. Some scattering curves show a more pronounced shoulder than others, but all exhibit these features. As the arrow in both graphs shows, the minimum of the form factor shifts to higher q-values with increasing temperature, indicating a decreasing droplet radius. All scattering curves show a plateau value in the low q-range. As discussed in section 2.2.2, the scattering data can be described by a combination of a core-shell form factor (equation 2.29) and a hard sphere structure factor (equation 2.30). The core-shell form factor needs six fitting parameters: droplet radius r_c, droplet polydispersity σ, shell thickness δ and the three scattering length densities of the water core, surfactant shell and octane matrix. The structure factor adds two more fitting parameters, namely the hard sphere volume fraction η and the hard sphere volume radius r_{HS}. The model needs to be complemented by a constant background and a prefactor, so a total of 10 fitting parameters are included in the model. But the scattering length densities are known and not temperature dependent and thus can be fixed during the fitting procedure, just as the shell thickness, $\delta = 2.1\,\text{Å}$[19]. Using the core radius r_c, the shell thickness δ and the length of the AOT tail group $l = 10.5\,\text{Å}$[19,25], the hard sphere radius can be estimated to $r_{HS} = r_c + \delta + 10.5\,\text{Å}$. Thus 5 fit parameters are left. The background is set to be the same value for all temperatures of one microemulsion sample and so one data set consisting of 9 temperatures can be fitted with 37 parameters.

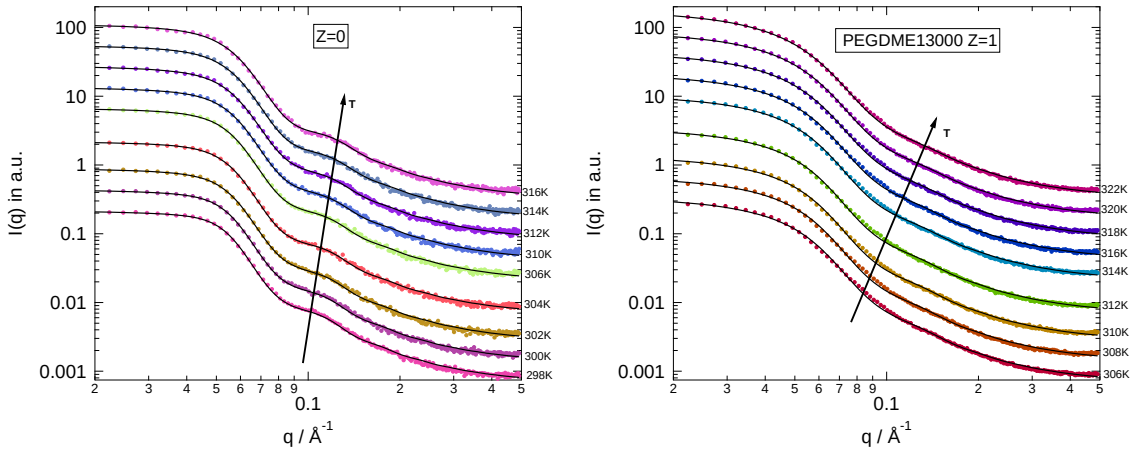

Figure 5.10.: Left: Scattering data from the unloaded microemulsion with $w = 30$. Right: Scattering data from the microemulsion with $w = 30$ containing one PEGDME1300 chain. The data curves are shifted in both graphs in order to better see the fitresults indicated by the black lines.

As seen in figure 5.10 the model describes the data very well, even for microemulsion with a very unpronounced shoulder. Before the radius of the water core is calculated, figure 5.11 shows the polydispersity σ and the hard sphere volume fraction η.

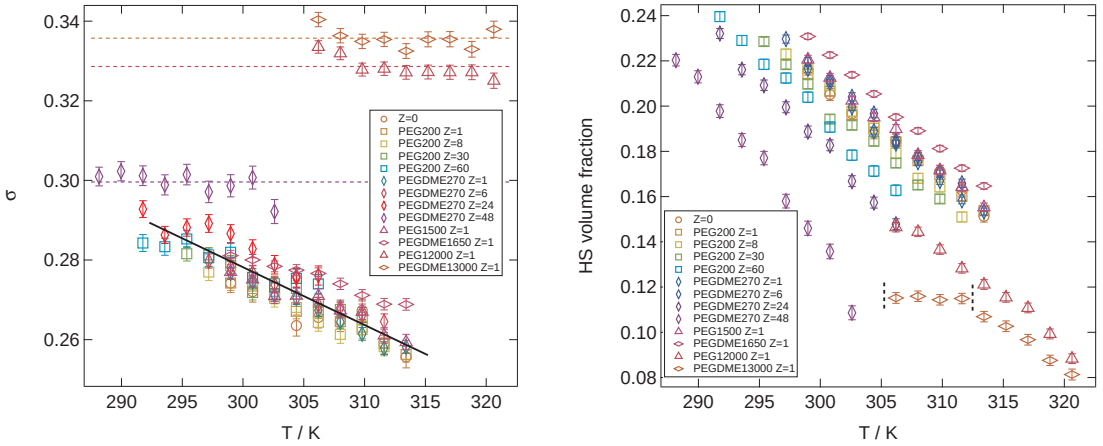

Figure 5.11.: Left: Polydispersity σ of all investigated samples. Right: Hard sphere volume fractions η of all investigated samples. The data points between dashed lines are neglected, since they are due to the unpronounced features of the data.

It can be seen that the polydispersity lies between 0.25 and 0.3 for most samples and decreases linearly with increasing temperature. The microemulsions that lie outside of this range and/or show a deviation from the linear decrease are the droplets that contain the highest number of monomers. The polydispersity increases by adding polymer, but the increase is very slight for small numbers of added monomers and does not seem do depend on the chain ends, but rather on how much the percolation temperature and thus the bending modulus of the droplet is influenced. Adding more monomers to the droplet causes an increase in polydispersity and stops the decrase with increasing temperature. Instead a constant polydispersity value seems to be reached. This increase in polydispersity for samples containing a high number of small PEG chains is probably due to the high number of wedges between the AOT head groups. Since the parameter Z just gives the average number, it is comprehensible that some droplets will contain even more wedges, while some will contain fewer wedges. For higher Z values and small chains this deviation seems to be more impactful than for small Z values and thus the polydispersity of the droplets increases. The highest polydispersity is found for samples containing one chain of the longest investigated chain length. Scattering curves of these two samples show a very unpronounced shoulder. Since the stabilisation caused by such large chains is very strong, it is highly likely that the difference between droplets containing zero, one or two chains of that molecular weight is very high. For these sample $Z = 1$ and thus it could very well be that there are some droplets containing no chain and some containing two chains. So the large difference between those cases causes the high polydispersity. All found polydispersity values exceed the value of 0.2, which was assumed as the maximum polydispersity in deriving our model function. But since most polydispersity only exceed this value slightly and even for the highest deviation the data is still described very well by the model, the obtained parameters are reasonable.

This is supported by the hard sphere volume fraction η. It should be noted that η is smaller than $\phi = 0.3$, but since η is an effective hard sphere volume fraction this result is plausible. The volume fraction seems to be uninfluenced by the addition of small and medium numbers of monomers. The graph suggests deviations from the volume fraction of the unloaded droplet, but the scale of these deviations is very small, so there is no

significant difference. A smaller volume fraction tends to show for an addition of a higher number of monomers. So the change in volume fraction is also influenced by the stability of the surfactant shell, but if the droplet is stabilised or destabilised can not be deduced from η, since it is the same for highly stabilised and highly destabilised droplets. For high temperatures the volume fraction decreases linearly significantly below 0.3, which is the original volume fraction of the the droplets inside the microemulsion. The linear decrease of η was also found by Domschke et al.[19] and the hard sphere volume fraction was interpreted as a parameter yielding information about the number of droplets that move freely inside the micoremulsion. This number decreases when the temperature is increased, since percolation occurs and clusters start to form, although the scattering data can be described without a structure factor that considers clustering, the samples containing high numbers of small polymer chains show an increase in the low q-range indicating clustering. Finally no sample shows a significant change in either σ or η when crossing the percolation threshold, since the nature of the percolation is dynamic.
In the derivation of the fitting model, the core radius r_c is assumed to be monodispers and thus needs to be corrected for the occurring polydispersity. Using the Schulz-Zimm distribution introduced in 2.2.2, it can be shown that r_c derived by the fitting model needs to be corrected with the factor $(1+2\sigma^2)$ in order to account for polydispersity[19,25]. The results for corrected radii of droplets containing PEG200 or PEGDME270 are shown in figure 5.12.

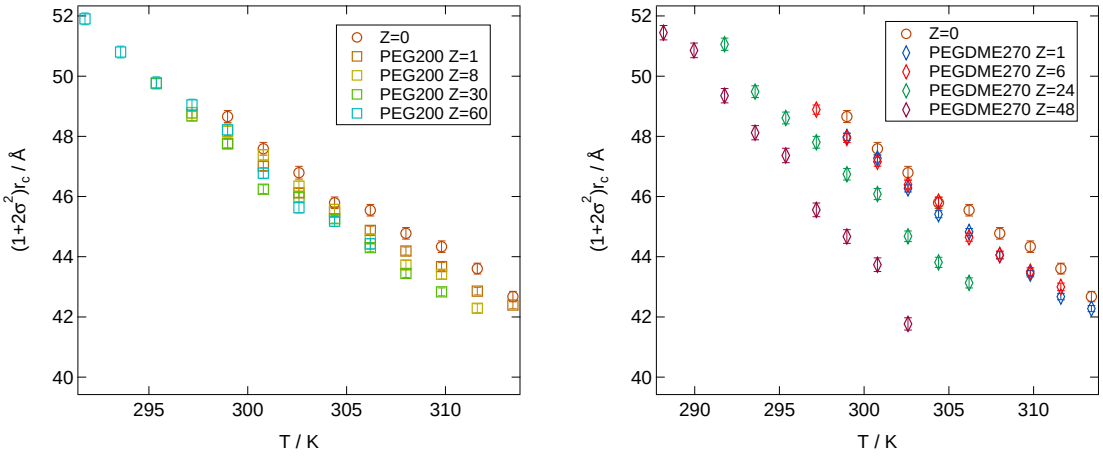

Figure 5.12.: Left: Corrected core radii of droplets containing varying amount of PEG200 chains. Right: Corrected core radii of droplets containing varying amount of PEGDME270 chains.

A very important observation is that the radius of each sample decreases linearly with temperature, which was also found in literature[19]. It can be seen that adding more and more PEG200 chains does not seem to highly influence the droplet radius in the observed temperature range. Due to the different percolation temperatures of the samples there are only some overlapping temperatures between the most loaded and unloaded microemulsion. Droplets loaded with varying number of PEGDME270 chains show radii influenced by the addition of more polymer chains. While the radius is unaffected for small Z, the droplet radius decreases drastically for the droplets containing the highest number of polymer chains. This is interesting for two reasons, first although large numbers of PEG200 chains inside the droplet also destabilise the droplet, the radius stays unaffected, but the sample containing 60 PEG200 chains and the sample containing 24 PEGDME270

chains show the same percolation temperature. Thus it seems that the droplet radius is not only dictated by the strength of the destabilisation, but even more by the process of destabilisation. Second the radius of droplets containing more PEGDME270 chains and thus more wedges is smaller than the radius of droplets with less wedges and the slope with which the radius decreases seems to be steeper. The discussion of the radius will be postponed until the radii of microemulsions containing high molecular weight PEG chains are shown, but the steep decrease of the radius containing large numbers of PEGDME270 chains can be explained by the destabilisation caused by the wedges. The large number of ideal PEGDME270 wedge causes the droplet radius to decrease in comparison to the unloaded microemulsion. Then with increasing temperature the radius decreases much faster than for the unloaded microemulsion.
Figure 5.13 shows the corrected radii of droplets containing one polymer chain with increasing chain length.

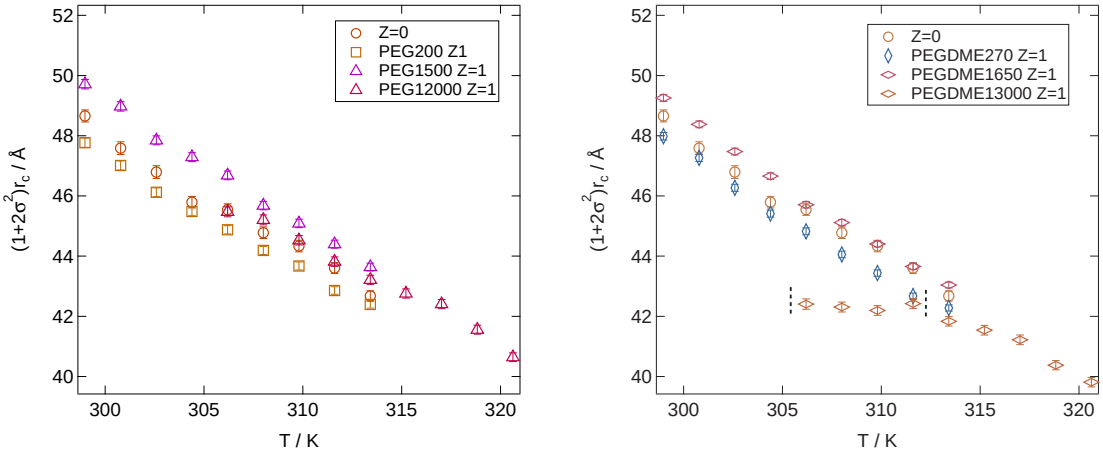

Figure 5.13.: Left: Corrected core radii of droplets containing one chain of PEG with varying chain length. Right: Corrected core radii of droplets containing one chain of PEGDME with varying chain length. The data points between dashed lines are neglected, since they are due to the unpronounced features of the data.

It can be seen again that the addition of monomers to a PEG chain does not influence the droplet radius by a lot. Now there is a slight increase instead of a slight decrease and the radii still decrease linearly with temperature. The same can be said for droplets containing one chain of PEGDME with increasing chain length, where the sample containing PEGDME1300 shows deviations from this linear behaviour, probably due to the unpronounced shoulder, causing the fit model to reproduce the same radius at lower temperatures, but since all other samples show a linear decrease these deviations are not regarded when determining the slope and intersect of the decrease of the radius with temperature.
All radii over temperature curves are fitted with a line in order to determine the rate of the decrease and the intersect with the y-axis, the radius at $T = 0\,\mathrm{K}$. Since all samples show a different percolation temperature, the slope and intersect of the line fit might yield better comparable quantities than the measured temperature. It should be noted that displaying $(1+2\sigma^2)r_c$ over $T - T_c$ is not possible, since T_c can not be determined. So the slope and the radius at $T = 0\,\mathrm{K}$ might provide a deeper insight into the interaction between the

polymer and the surfactant. Figure 5.14 shows the results for the slope and the intersect obtained by the fit.

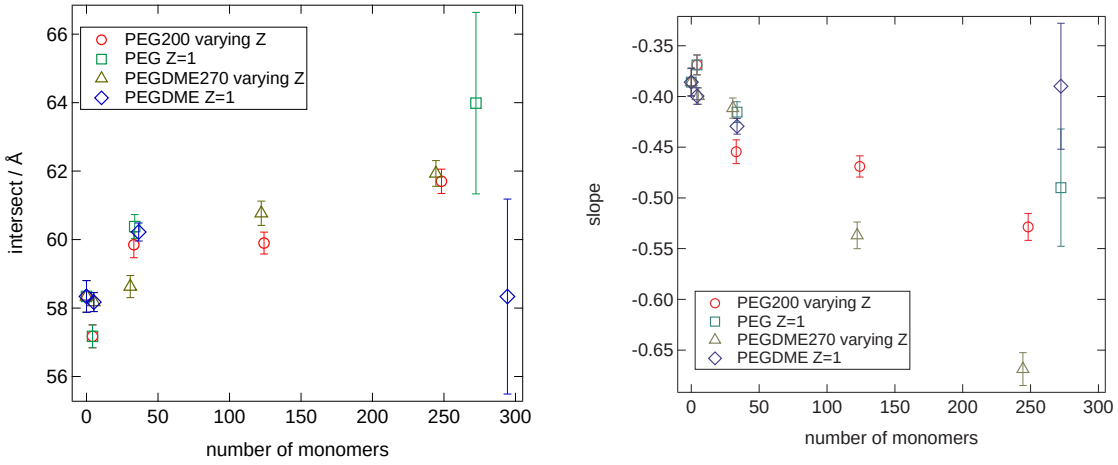

Figure 5.14.: Left:The intersect of the investigated samples. Right: Rate of the decrease of the radii of the investigated samples

The intersect must be discussed while keeping in mind that the samples are not stable microemulsions at $T = 0\,\mathrm{K}$. Still it is interesting to note that the intersect does seem only to depend on the number of monomers inside the droplet and not on the number of chains. Droplets containing one PEG12000/PEGDME13000 chain show deviations from the linear behaviour due to the scattering profile and thus their error bars are that large. So the intersect suggests that adding small numbers of monomers to the droplet increases its radius. For small polymer chains a further addition results in more chains and more wedges increasing the radius even further. For larger chains the results differs between PEG and PEGDME so a result can not be obtained.

This changes when looking at the slope of the decrease. Overall the slope is comparable to previous reported decrease in radius with increasing temperature [19]. Droplets containing a high number of PEGDME270 chains exhibit a much faster decrease in droplet radius than all other samples. The droplets containing PEG200 also decrease their droplet radius faster with increasing number of polymer chains, but the decrease is not as fast as for droplets containing PEGDME270. By increasing the chain length instead of the number of chains it seems the steepening in the decrease rate can be stopped and might even be reversed.

By looking at $(1 + 2\sigma^2)r_c$ at T_p the interpretation can be supported. In this display an increase in the number of polymer chains is shown by a decrease in T_p, while an increase in chain length is shown by an increase in T_p. At the percolation threshold droplets containing more and more small polymer chains show a larger and larger radius. This is due to the increasing number of wedges between the AOT head groups that cause the droplet to "swell". Since PEGDME270 seems to be a more ideal wedge for microemulsions with $w = 30$. The radius at T_p is larger than for droplets containing even more chains of PEG200. Using the geometrical observation from section 2.2.2 that $(1 + 2\sigma^2)r_c = \frac{3v_w}{A_{AOT}}w$ this can be interpreted that at T_p longer chains pull the AOT head groups together effectively increasing the area each head group contributes to the droplet, while smaller chains divide the head groups lowering their contributing area.

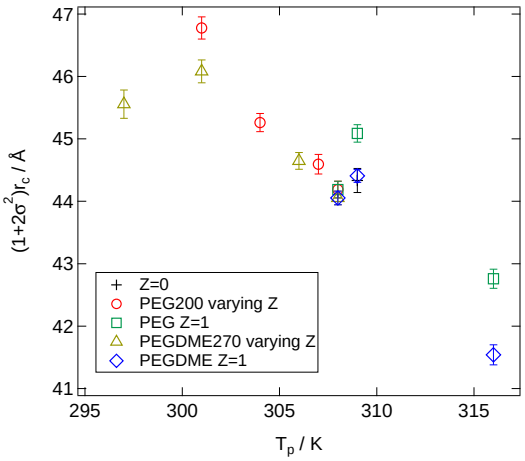

Figure 5.15.: Corrected droplet radius of investigated samples at T_p.

But the high number of chains also causes the droplet radius to decrease faster with increasing temperature than the radius of droplets containing less, longer or no chains. To explain this phenomenon it should be mentioned that the unloaded microemulsion droplet decreases in size with increasing temperature, because the AOT tail volume increases faster than the volume of the AOT head group[19]. Thus it is plausible to assume that the droplet can only swell to a certain radius due to the introduced wedges.

Increasing the number of wedges further decreases the droplet radius, since the spontaneous curvature of the AOT molecules can not accommodate a further swelling and instead the number and volume of the wedges causes the droplet to decrease in size. This would also explain why the droplets containing large number of small chains decrease faster in size than the other droplets. The rise in temperature causes the polymer wedges to increase in volume and due to the large number of wedges this causes the droplet radius to decrease with a higher rate than the droplet radius of microemulsion containing one large polyethylene glycol chain. In these systems the large chain seems to slightly counteract the radius decrease due to the swelling AOT tails, probably by "connecting" AOT head groups.

Summary of the Interaction of Polyethylene Glycol with the AOT Surfactant Shell

BDS and SAXS measurements have shown that the addition of polyethylene glycol can destabilise or stabilise the droplet phase of water/AOT/octane micremulsions by interacting with the surfactant layer. If and how strong the droplet is stabilised or destabilised depends on the radius of the droplet, the length of the polymer chain and the number of polymer chains. The chain ends of the polymer do not seem to influence the interaction. In order to describe the interaction of polyethylene glycol with AOT, the wedge model is employed[23,94,95]. The polymer chains wedge themselves between the AOT head groups and destabilise the droplet, if the wedges have the right size and their number is large enough. Chains that are too small have no effect on the droplet, while chains that are longer than the ideal wedge size start to stabilise the droplet again, by connecting AOT headgroups with the part of the polymer chain that is not wedged between two AOT headgroups.

Droplets that are destabilised by wedges increase in radius compared to the unloaded droplets, while stabilised droplets become smaller. This is probably due to a swelling caused by small wedges between the AOT head groups, while larger chains seem to pull the AOT heads closer together decreasing the droplet radius. All microemulsions exhibit a decreasing droplet radius with increasing temperature. The strength of this decrease

is higher for microemulsions loaded with many smaller chains than for the unloaded microemulsion. Microemulsions loaded with long polymer chains tend to show an even weaker decrease in the droplet radius. So it seems that the temperature induced decrease in radius due to the swelling of the AOT tails can be enhanced by providing a large number of wegdes that will also swell with temperature, while it can be weakened by a large polyethylene glycol chain inside the droplet. This assumption is supported by the fact that at T_p the radius of the droplet containing 48 PEGDME270 wedges is smaller than the radius of the droplet with 24 PEDGME270 wedges, although the pure number of wedges would suggest otherwise.

6 Structure of an Elastin-like Peptide in a Buffer Solution

As mentioned before the ELP investigated in this work should become more compact upon heating before undergoing denaturation. This contraction is reversible and thus cooling the protein will cause the structure to become less compact again [5,14,35–37,98–100]. Meaning that hydrogen bond structure of the ELP and the surrounding water is very dynamic and depends highly on the temperature of the system. Simulations suggest that the change in structure should cause the radius of gyration of the ELP to decrease [98,100,101]. In addition to the Inverse temperature transition (ITT) the ELP also exhibits a LCST, which is supposed to be higher than the boiling point of water for short peptide chains [15]. So the LCST is not expected to be within the temperature range observed in this work, but still the conformation change of a single peptide chain could be overshadowed by the collective phenomenon of a starting aggregation caused by the LCST.
Structural investigations on the ELP in buffer solution are done using SANS. All components of the buffer are deuterated and so a sharp contrast between peptide and buffer should arise, even though some deuterons of the buffer might exchange with protons from the peptide. This enables the observation of a radius of gyration in order to investigate, if the ITT is observable in the structure information obtained by SANS.

6.1 A Model Free Guinier Approach

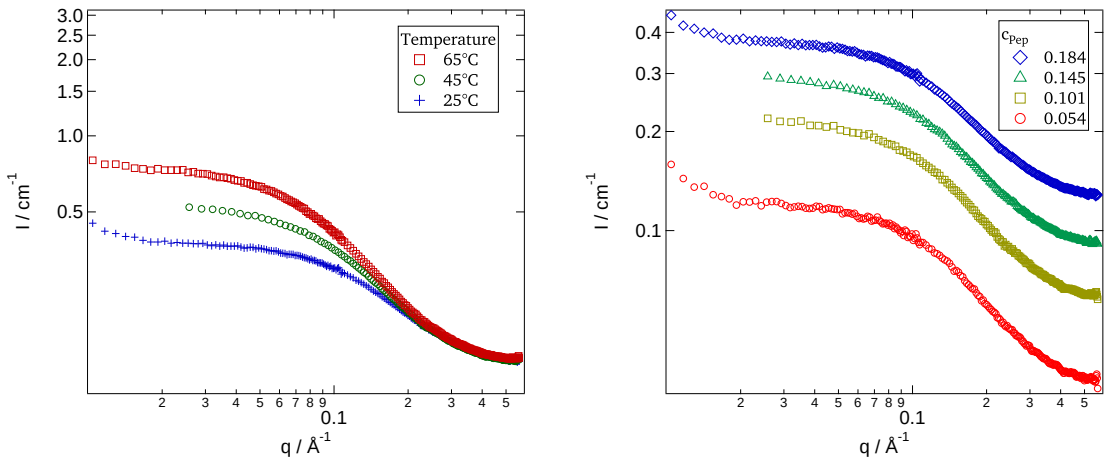

Figure 6.1.: Left: SANS data for the peptide buffer solution containing 18.4 wt% of peptide for different temperatures. Right: SANS data for all observed peptide concentraions in the peptide buffer solution at 25 °C. The data is not shifted.

In this work binary mixtures of peptide and buffer with 5.4, 10.1, 14.5 and 18.4 wt% of peptide were measured between 25 °C and 70 °C. Figure 6.1 shows exemplary measurement results. It can be seen that the intensity increases with temperature as well as

concentration for low q values. At small q values there is a plateau that goes into an steep increase again for q values below 0.02 Å, so single particle scattering was observed and slight tendencies for aggregation can seen. Due to time limits for the SANS measurements the very low q range showing the indication for aggregation is not available for all data sets. At large q values the intensity shows a background level given by incoherent scattering. The background is independent of temperature, but increases with increasing concentration due to the higher number of protons.
From the scattering intensity in the low q range the overall size of the scattering peptide can be extracted. According to Guinier's law the intensity in this range is given by: [77,78]

$$I(q) = I(0) \cdot e^{-\frac{q^2 R_G^2}{3}} \tag{6.1}$$

Where R_G is the radius of gyration of the particle. This law is valid as long as $q \cdot R_G < 1$. The Guinier law describes the data very well as can be seen in figure 6.2 on the left side. There a line fit representing the Guinier law is applied to the data in a ln I over q^2 plot. From the slope of the lines the radii of gyration can be determined and the result is shown on the right side of figure 6.2.

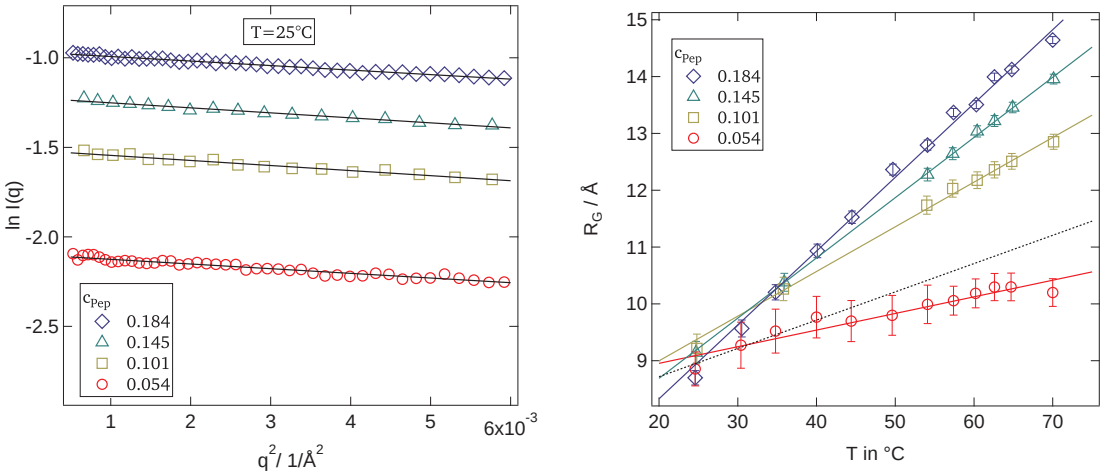

Figure 6.2.: Left: Guinier representation of all concentrations at 25 °C. The fit of the Guinier law is indicated by black lines. Right: Radius of gyration R_G derived from the line fits on the left side. Coloured lines show the line fit applied to the data. The dashed line indicates the expected increase for the lowest concentration.

At low temperatures all concentrations seem to have the same R_G. But the radius of gyration increases strongly with temperature and the increase becomes larger for larger concentrations of peptide. All concentrations show a linear increase in R_G, which can be described by $R_G = \alpha + \beta \cdot T$. This increase indicates a strong aggregation of peptide chains, since the size of the scattering particle becomes larger although there is no evidence for an increase in size of the single peptide chain. The increase is too large to be caused by an increase in temperature, when compared to a polymer and due to the ITT a decrease in R_G would be expected.
Looking at the dependence of β on concentration on the left side of figure 6.3 reveals a linear increase with increasing concentration. Only the low concentration sample deviates from this behaviour and increases much smaller than expected from the other concentrations. This could be an indication of the ITT. Extrapolating the linear behaviour to 5.4

wt% would yield the dashed line on the right side of figure 6.2. So the ITT could be overshadowed by the aggregation process for high concentrations, but for the lowest concentration the influence on R_G of the ITT could be isolated by eliminating the increase due to aggregation on R_G. In order to achieve this elimination the derived radii of gyration are divided by the fitted $\alpha + \beta \cdot T$, except for the lowest concentration. R_G of the lowest concentration is instead divided by the function containing α and β extrapolated from the higher c_{pep}. The result of this procedure is displayed on the right side of figure 6.3.

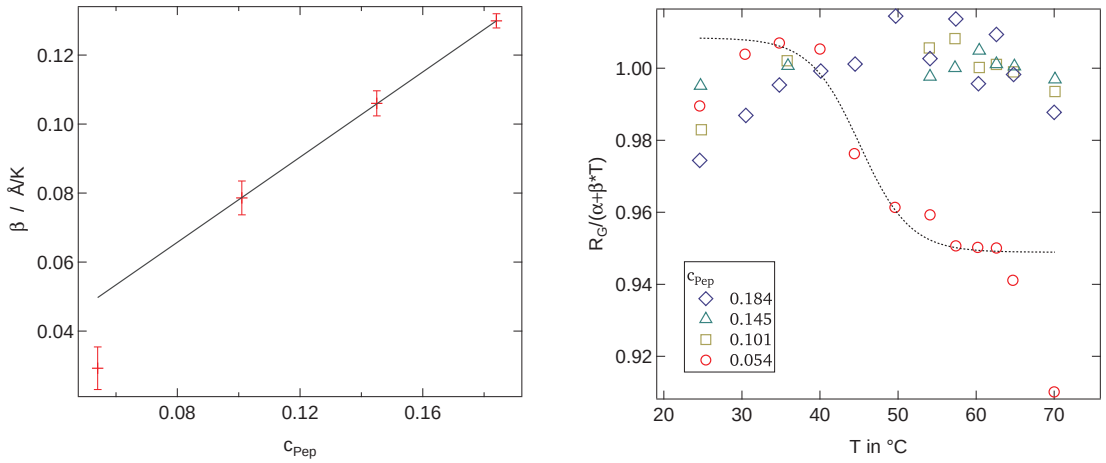

Figure 6.3.: Left: The slope of the line fits to the radius of gyration from the Guinier law. The black line indicates the linear behaviour of the increase. Right: R_G divided by $\alpha + \beta \cdot T$ for all samples. For the lowest concentration the extrapolated beta and not the one derived by the fit was used. The black dashed line is a guide for the eye for the deviations of the lowest concentration.

For the high concentrations the deviations are caused by the difference from the assumption of a linear increase in R_G and the R_G determined by the Guinier law. Since these deviations are very small, the radius of gyration can be assumed to increase linearly with temperature. This increase is probably due to aggregation and should also be observed in the sample with the smallest concentration of peptide. But while the lowest concentration also shows low deviations from the linear increase in R_G there seems to be a countering effect that causes the scattering particle to increase slower in size than the aggregation behaviour observed in all the other samples would dictate. The temperature at which the deviations become observable lies in the range in which the ITT was proposed [5,36]. Above 50 °C the deviations fall on a plateau again, since the conformation change has been undergone and now the increase in R_G is again solely governed by aggregation.
The increase in R_G also indicates that for every temperature and concentration there exists a scattering cluster with an ideal size. Since all concentrations show the same R_G at lower temperatures, it seems that there is a starting system state independent of concentration. Increasing the temperature causes the peptide chains to aggregate, so the energy to form inter molecular hydrogen bonds must be lower than the energy to form hydrogen bonds with the surrounding water or to form intra molecular bonds. Further increasing the temperature then makes more hydrogen bond sites available more neighbouring peptide chains, and thus the cluster increases in size. But the cluster size also increases with increasing concentration, suggesting that the ideal cluster size is also dictated by the number of available bonding partners inside the solution. This argument does not take large entropic changes into account. So the question arises, if the cluster size continues to

increase by adding more peptide chains into the solution or if there is a maximum cluster size that will not increase even if the concentration or temperature is increased. It would also be interesting to study, if denaturing the peptide will only break the intra molecular bonds and thus make even more inter molecular bonding sites available, causing the cluster to further increase or if all peptide bonds will break destroying the cluster.

6.2 Comparing the Peptide with a Gaussian Coil

Up until now only the low q range was used in order to obtain information about the overall size of the scattering particles. Investigating the range of $q \geq 1/R_G$ yields information about the internal structure of the scattering particle (molecule or aggregate). An ideal Gaussian polymer coil would exhibit a $\propto 1/q^2$ decay of intensity. This behaviour can be illustrated fairly well in a Kratky plot where $I \cdot q^2$ vs q is displayed, where the ideal coil would show a plateau for large q values. The standard Kratky plot depiction does not take the changing size found in the Guinier approach into account, therefore figure 6.4 shows a scaled version of the Kratky plot [102]. There the q axis is multiplied with R_G obtained by the Guinier approach and the intensity is divided by the extrapolated intensity at $q = 0$.

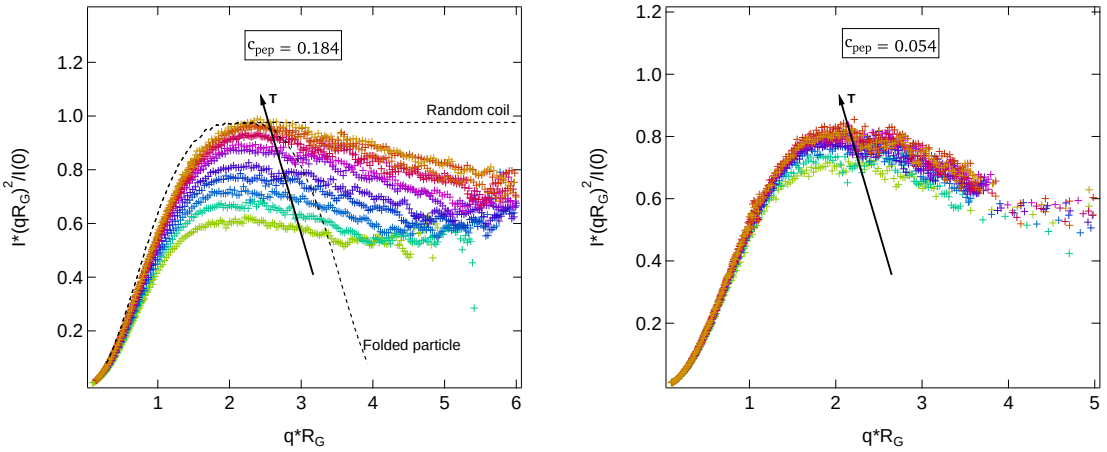

Figure 6.4.: Left: Scaled Kratky plot for the sample with the highest concentration of peptide at all temperatures. Temperature increases in the direction of the arrow. The dashed lines idicate the expected course for an ideal Gaussian coil and a spherical particle. Right: Scaled Kratky plot for the sample with the lowest concentration of peptide at all temperatures. Temperature increases in the direction of the arrow. For large q values the data was averaged every ten points, because the data was very close to the observed incoherent background scattering.

The plot shows that $I \cdot q^2$ decays with q and does not reach a plateau value. Such behaviour is often observed for proteins [7,103,104] and taken as indication for a denser state. In the regime where $q \cdot R_G > 1$ the scattering data gives information about the correlation between inner molecular segments. A globular particle for example would show a bell like curve in the Kratky plot. The data obtained for the peptide shows a behaviour between the two mentioned cases and thus seems to be partially folded and Gaussian particle [103,104]. In the scaled Kratky plot a universal curve independent of temperature can be observed for low q values and while this universal behaviour extends to the large q regime for the smallest peptide concentration, it changes into a temperature dependent behaviour for larger concentrations, further validating the difference between them.

Still neither concentration shows a change in conformation with temperature, implying that the ITT observed in the low q regime via R_G is very subtle and does not show itself in the Kratky plot. It can also be seen that the peptide seems to be closer to a ideal Gaussian coil than to a folded spherical particle and thus the scattering of the peptide could also be described by a model developed for polymer chains. The mean squared distance between two chain segments i and j of a polymer chain that takes on the conformation of an ideal Gaussian coil ($\nu = 0.5$) is given by $< r_{ij}^2 >= a^2 |i-j|^{2\nu}$, with the Flory parameter ν. Calculating the scattering function from this formula for n segments yields: [105]

$$I(q) = c \cdot \left[\frac{1}{\nu \alpha^{\frac{1}{2\nu}}} \gamma \left[\frac{1}{2\nu}, \alpha \right] - \frac{1}{\nu \alpha^{\frac{1}{\nu}}} \gamma \left[\frac{1}{\nu}, \alpha \right] \right] + bkg \tag{6.2}$$

With α defined as:

$$\alpha = \frac{1}{6} R_{Ham}^2 q^2 (2\nu+1)(2\nu+2) \tag{6.3}$$

The radius of gyration in this model is defined as $R_{Ham} = a\{N^{2\nu}/(2\nu+1)(2\nu+2)\}^{1/2}$ and stands in for the segment length a as a parameter to define a length scale. The prefactor is c and γ the lower incomplete gamma function.
Figure 6.5 shows examples of how accurate the model can describe the data. The data was fitted with completely free parameters, except for the background which was set to a common background for each concentration. So the peptide can indeed be compared to a slightly condensed ideal Gaussian coil. From the model quantitative parameters describing the conformation and the influence of concentration and temperature on these parameters can be derived. It can also be seen that the possible onset of aggregation at very low q values limits the range in which the model describes the data. The radius of gyration of the model R_{ham} and its deviation from the radius of gyration R_G obtained from the Guinier approach are shown in figure 6.6.

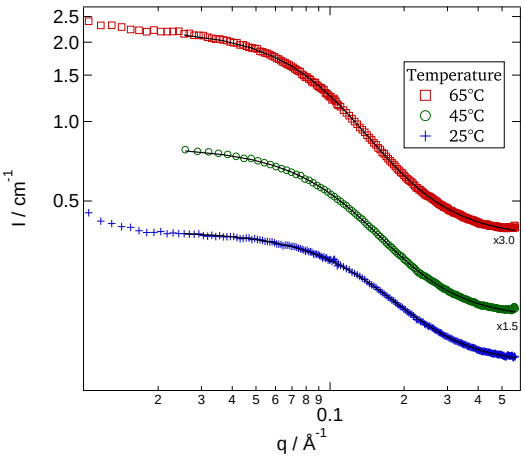

Figure 6.5.: Fit of equation 6.2 to the data of the sample $c_{Pep} = 0.184$. The curves are shifted for clarity.

The radius of gyration R_{Ham} increases linearly with temperature just like R_G derived from the Guinier approach and in general shows the same behaviour for all concentrations and temperatures. But here the lowest concentration does not deviate from the others and exhibits the expected increase instead of a lower one. So it seems that by estimating the radius of gyration from the segment length obtained from the large q regime, information about the ITT is lost. This is probably correlated with the fact that R_{Ham} has larger absolute values than R_G. The right side of figure 6.6 illustrates how the model overestimates the chain length when compared to the model free Guinier approach.

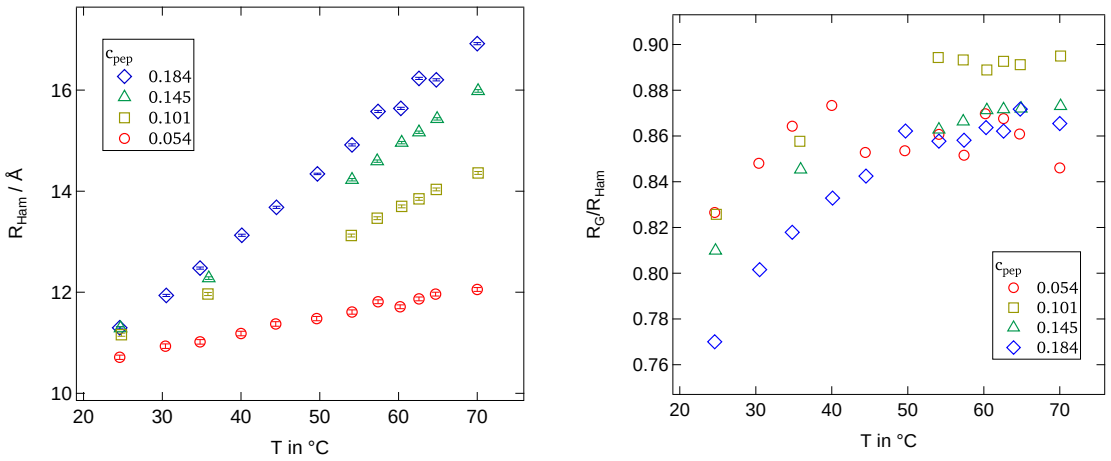

Figure 6.6.: Left: R_{ham} derived from the fit of equation 6.2 on the data. Right: Ratio of R_G to R_{Ham}.

The overestimation becomes larger for lower temperatures, while it seems to reach a plateau value 50 °C. So there is reason to think that the ITT could be hinted at in the displayed ratio. At low temperatures the peptide is a single chain or part of small clusters. A change of conformation caused by the ITT would cause the Guinier approach to show a smaller radius of gyration than the Hammouda model, since the latter takes the segment length to calculate the radius of gyration. As the temperature increases, so do the peptide cluster increase in size and thus the influence of the ITT on the observed radius of gyration becomes smaller in both perspectives. Hence the overestimation of the Hammouda model deceases. Only after the ITT is finished above 50 °C the ratio becomes constant, indicating that there is a difference between the two radii of gyration to begin with, probably due to the difference in structure between a peptide and a Gaussian polymer coil.

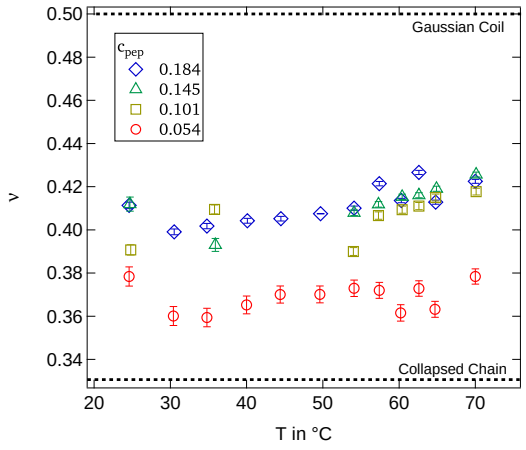

Figure 6.7.: Flory parameter obtained from the Hammouda model fit. The dashed lines indicate the Flory parameter for a Gaussian Coil and a collapsed chain.

Another interesting quantitative parameter is the Flory parameter ν which yields information about the conformity of the peptide inside the buffer solutions. The Flory parameter of the ELP is displayed in figure 6.7. All concentrations show a Flory parameter lower than 0.5 and thus a more dense structure than a Gaussian coil. The Flory parameter for the three highest concentrations shows the same constant value over all temperatures. So the solubility does not seem to change when almost doubling the concentration from 10 to 18 wt%. The lowest concentration however achieves a lower Flory parameter. This could indicate that the deviation from the Gaussian coil is stronger for this concentration than for the other, which would be in good agreement with the Kratky plots, where the lowest concentration has a faster decay with q than the other concentrations. There is also some sort of bump in the Flory exponent leading up to 50 °C for the lowest concentra-

tion. At temperatures above 50 °C the Flory exponent takes on a constant value just like for the other concentrations. So the Guinier approach and the Hammouda model as well as a comparison of the radius of gyration obtained from both perspectives yield parameters indicating that an ITT could have taken place below 50 °C. The ITT is only observable in the data, if the concentration of the peptide is low enough at higher concentrations aggregation effects overshadow the ITT.

6.3 Quantifying the Peptide Aggregate

Since R_G does not contain information about the number of peptide chains inside the cluster, it might be interesting to attain that number to see, if it possibly yields more information about structural changes of the peptide chain. The molecular weight of the scattering particle can be derived by a set of invariants introduced by Porod [80,104]. Since the scattering invariant $Q = \int_0^\infty I(q)q^2dq$ can not be determined, if the curve in the Kratky plot never reaches zero, a new invariant needs to be defined. The integral $Q_p = \int_0^\infty I(q)qdq$ converges for all types of scattering particles and can be calculated to: [76,80]

$$Q_p = 2\pi \cdot c \cdot (\Delta\rho)^2 \cdot V_P \cdot l_c \tag{6.4}$$

Where c is the concentration of scattering particles, $\Delta\rho$ is the differece in scattering length density, V_P is the volume of the scattering particle and l_c is the correlation length. For a detailed derivation of this solution and a proper introduction of the correlation length the reader is referred to [76,80]. The correlation length relates the quantities Q and Q_P: [76,80]

$$l_c = \pi Q_p / Q \tag{6.5}$$

Using the intensity at $q = 0$, Q can be eliminated from this equation and thus a well defined Q is not necessary anymore in order to calculate the volume of the scattering particle: [76,80]

$$\frac{I(0)}{Q_p} = \frac{c_{pep}(\Delta\rho)^2 \cdot V_P^2}{2\pi \cdot c \cdot (\Delta\rho)^2 \cdot V_P \cdot l_c} = \frac{V_P}{2\pi l_c} = A_c \tag{6.6}$$

Defining the ratio $I(0)/Q_p$ as a new parameter A_c [104], a parameter is obtained that has the dimension of an area and is an invariant independent of concentration. A_c does not require a folded particle and is directly related to the structural state of the particle [104]. Since the volume of the scattering particle is directly related to Q_p, it is interesting to display $I \cdot q$ over q. Figure 6.8 shows $I \cdot q$ over q for the highest and lowest concentrations of peptide.

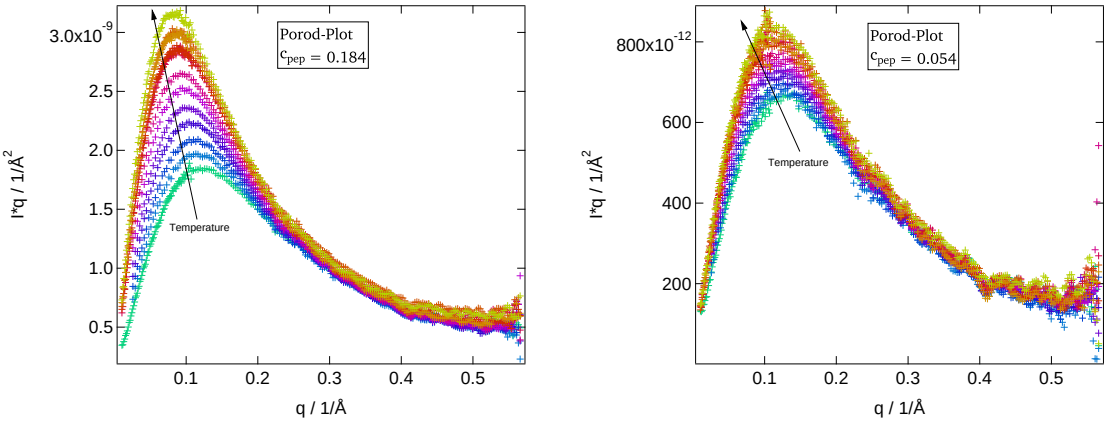

Figure 6.8.: Left: $I \cdot q$ over q for the highest concentration of peptide for all temperatures. Right $I \cdot q$ over q for the lowest concentration of peptide for all temperatures. The arrow indicates increasing temperature.

A partially folded flexible particle shows a bell like curve in this representation and thus the integral Q_p can be determined. The maximum of the peak shifts to slightly lower q and to higher $I \cdot q$ values with increasing temperature, but the course of the curve is independent of temperature. Using $I(0)$ obtained from the Guinier approach, A_c can be calculated (see figure 6.9 on the left). As expected from the $I \cdot q$ over q depiction, A_c increases linearly with temperature for the higher concentrations and increases with concentration at higher temperatures. The lowest concentration shows an almost constant A_c, which could hint at a constant mass and once more emphasizes the special status of the lowest concentration.

Rambo et al. found that the ratio $Q_c = \frac{A_c^2}{R_G}$ exhibits a linear behaviour in a log-log plot over the mass of the protein [104]. Therefore there exists a power law relationship between the ratio Q_c and the particle mass in the form of: [104]

$$Q_c = j(\text{molecular mass})^k \tag{6.7}$$

and therefore:

$$\text{molecular mass} = \left(\frac{Q_c}{j}\right)^{1/k} \tag{6.8}$$

The parameters j and k are empirically determined and specific to a class of macromolecular particles. They are $j = 0.1231$ and $1/k = 1$ for proteins. Taking R_G from the Guinier approach, Q_c can be calculated and thus the mass of the scattering particle can be calculated as well. The result of this calculation can be seen on the right side of figure 6.9.

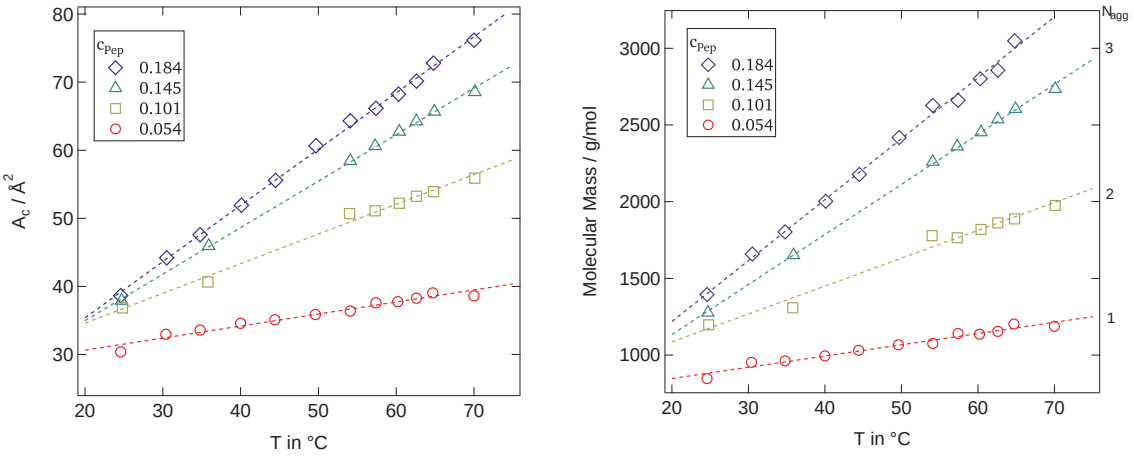

Figure 6.9.: Left: Calculated A_c for all concentrations and temperatures. Right: Molecular mass of the higest and lowest concenteration.

As expected from the results for R_G and A_c the mass increases with temperature for the highest concentration, while it remains constant for the lowest concentration. Since a single peptide chain should yield a molecular mass of 1458 g mol^{-1} it can be assumed that the lowest concentration contains one peptide chain as a scattering particle. This suggests that the uncertainties of the A_c and mass calculation are rather large and hence they are omitted from the figure. Based on the assumption that the sample with the lowest concentration exhibits the scattering of a single chain, the number of chains in the aggregates of the other samples can be estimated and is shown in the figure.

Summary of the ELP Structure Inside a Buffer Solution

In this chapter it was shown that an ELP in buffer solution exhibits many traits of a flexible polymer chain in a solvent. The overall size of the scattering particle was deduced with a model free Guinier approach and an increasing radius of gyration with increasing temperature was found for all concentrations of peptide. Analysing the nature of this increase led to the discovery that for the smallest concentration the increase in R_G is lower than expected and deviates from the other concentrations, due to the ITT. A detailed view on this behaviour revealed a significant temperature of 50 °C. Still the dimensionless Kratky plot did not reveal any change in structural conformation, but instead showed that the peptide behaves more like Gaussian polymer coil. A model for such coils by Hammouda is able to describe the scattering data and the estimated radius of gyration R_{Ham} behaves like R_G, but shows no sign of an ITT. But the ITT can again be found when comparing R_{Ham} and R_G as well as when looking at the Flory parameter, which revealed that the lowest concentration deviates stronger from the Gaussian coil than the other concentrations. In addition to the analysis of the radius of gyration, the molecular mass of the scattering peptide was analysed as well. There it was found that the peptide chains aggregate for all higher concentrations and while the cluster increases in size for the higher concentrations, the lowest concentrations shows a constant mass. Still this mass is lower than that of a single peptide chain, leading to the interpretation that the ITT can only be observed in systems, where the concentration of peptide is low enough

so that aggregation processes do not overshadow the subtle structural changes caused by the ITT.

7 The Influence of Soft Confinement on an Elastin-like Peptide

In the last chapter the structural conformation of an ELP in buffer solution was investigated in dependence on concentration and temperature. It was found that the inverse temperature transition is overshadowed by an aggregation process and that the peptide tends to take on the structure of a flexible chain instead of a folded particle. This could cause the peptide and thus the protein Elastin to lose its biological function. In reality the protein will be inside a cell, which acts as a soft confinement for the protein. There will be many more components inside the cell besides the protein, making a structural investigation of the protein in confinement very difficult. So instead of studying the entire protein Elastin inside a realistic model of a human cell, the ELP will be brought inside the extensively researched soft confinement provided by a buffer, AOT, octane microemulsion. It will also be interesting to see, if an attractive interaction between the surfactant and the peptide can be found, as it was the case for polyethylene glycol confined in the same system and if that interaction stabilises or destabilises the droplet.
Therefore microemulsions with $w = 15$ and $\phi = 0.3$ containing no, one, two, three or four ($Z = 0, 1, 2, 3, 4$) peptide chains are prepared. All components of the microemulsion except for the peptide are deuterated in order to ensure a favourable contrast when using SANS measurements. Since deuterated AOT and the ELP are not available in large quantities, only a small amount of sample could be prepared, enabling SANS and SAXS measurements. Thus allowing for an observation of the influence of confinement on the peptide chain (SANS) and vice versa (SAXS). The results obtained from BDS and SAXS measurements on water/AOT/octane microemulsions loaded with polyethylene glycol will assist in order to determine the influence of the ELP on the confinement.

7.1 Structural Characterisation of the Soft Confinement

In the following the influence of the peptide chains on the microemulsion droplets will be investigated. It should be mentioned that all samples were measured via SANS before the SAXS measurements and extracted from the helma cuvettes in order to be inserted into the capillaries for SAXS measurements. All microemulsion SAXS measurements took place at temperatures ranging from 25 °C to 65 °C in increments of 5 K.
The results for the microemulsions containing no peptide chain and four peptide chains are shown in figure 7.1. Black lines show the fit of the core-shell form factor in combination with a hard sphere structure factor already used in section 5.4. The fit parameters are the same as before, except for the hard sphere radius, which is now a free fit parameter. This can be explained with the small radius of $w = 15$ droplets. Now the AOT tail groups of neighbouring AOT molecules could be far enough apart for octane molecules or AOT tails from other droplets to wedge themselves deeper between them, decreasing the hard sphere radius independently.

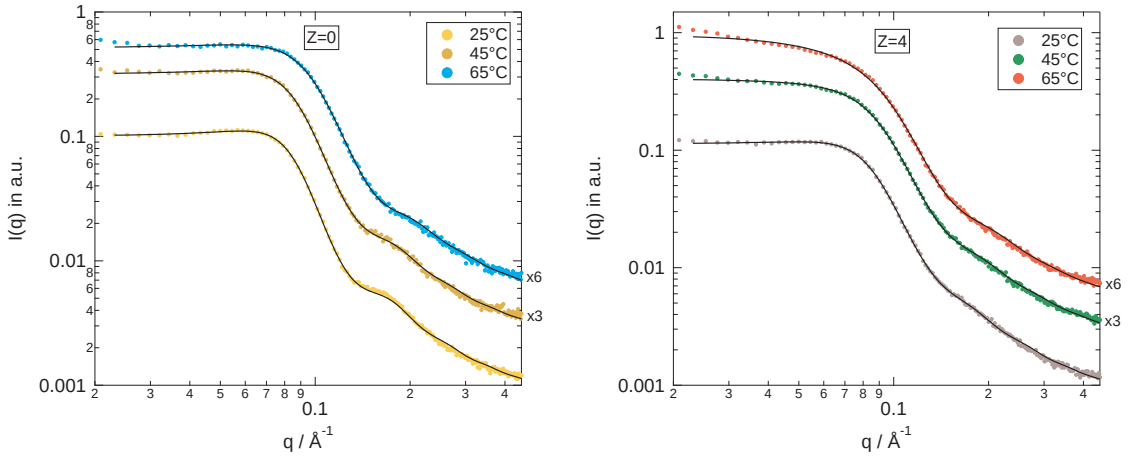

Figure 7.1.: Left: Raw data of the microemulsion containing no peptide chain. Right: Raw data of the microemulsion containing four peptide chains. Black lines indicate the core shell form factor hard sphere structure factor fit. Curves are shifted for clarity.

The model describes the data very well and thus suggests that there is a droplet phase present for all temperatures and concentrations of peptide inside the droplet. Since the peptide does not dissolve in octane it can be assumed that it is inside a droplet and confined by the surfactant layer of that droplet.

For the samples with $Z = 1, 2, 3$ the scattering curves behave very differently with increasing temperatures, decreasing strongly in intensity and exhibiting strong structural peaks (see figure 7.2). Removing the capillaries from the sample holder showed that the samples partly separated, causing the capillary to get porous and the sample to move from the beam for the sample containing three peptide chains. (This behaviour could not be seen during SANS measurement, that took place before the SAXS measurements and will be discussed later). Still the data can be described by the developed fitting model and for low enough temperatures the data seems to be reliable for all samples and thus the low temperature range will be focussed upon.

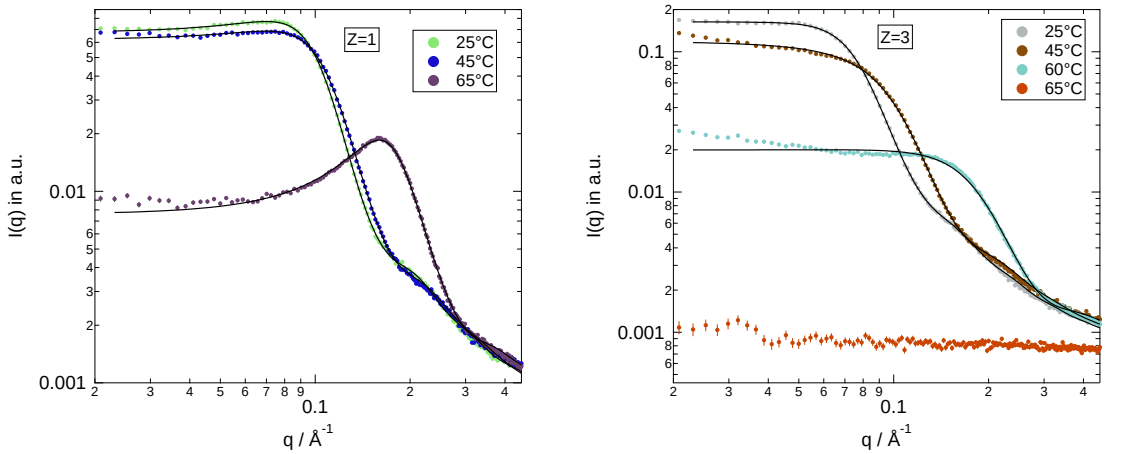

Figure 7.2.: Left: Raw data of the microemulsion containing one peptide chain. Right: Raw data of the microemulsion containing three peptide chains. Black lines indicate the core shell form factor hard sphere structure factor fit.

Once again the polydispersity σ and the hard sphere volume fraction η, shown in figure 7.3, are very interesting parameters to study.

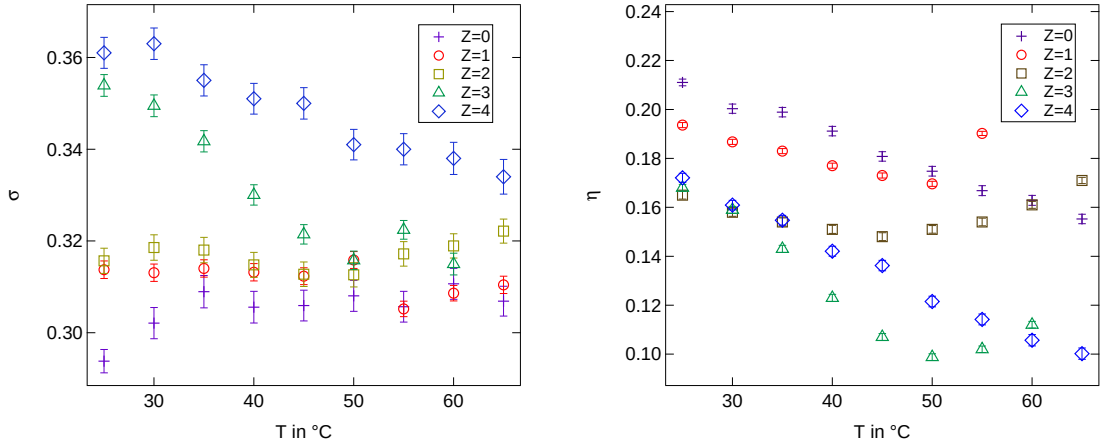

Figure 7.3.: Left: Polydispersity σ. Right: Hard sphere volume fraction η.

The polydispersity lies above 0.3 for all samples. While the polydispersity remains constant for samples with $Z = 0, 1, 2$, it shows a decrease for samples containing three or four peptide chains per droplet, where the decrease for $Z = 3$ is very remarkable and probably due to the bursting of the capillary. Since the molecular weight of of the peptide (1458 g/mol) and its radius of gyration in bulk solution can be compared to PEG1500 [22], there is an interpretation for this behaviour, using the results for microemulsions loaded with polyethylene glycol. By adding one or two peptide chains to the droplet the polydispersity does increase slightly suggesting that the droplet is either slightly stabilised or destabilised. In section 5.1 it was found that for decreasing droplet radii the chain length at which the destabilisation effect is outweighed by the stabilisation effect becomes shorter. Thus the peptide should stabilise the droplet, because PEG1500 showed no effect or stabilised the droplet for $W = 20, 30, 40$. This is further supported by the high polydispersities for the samples containing three or four peptide chains. Microemulsions loaded with polyethylene glycol showed about the same increased polydispersities for highly stabilised droplets.

The hard sphere volume fraction η shows a linear decrease for all samples at low enough temperatures and while the linear decrease continues for $Z = 0$ and $Z = 4$, there is a deviation from this behaviour in form of an increase for the other samples. This indicates the range in which the fit yields trustworthy results and further supports the existence of a droplet phase in the entire temperature range. Also the same conclusion from the polydispersity can be derived when comparing it to the hard sphere volume fraction of microemulsions loaded with polyethylene glycol.

Figure 7.4 shows the corrected water core radius of all investigated microemulsions. Due to the small amount of sample it was not possible to determine percolation temperatures using BDS and thus the radius at T_p can not be given. Instead r_c at the absolute temperature will be studied again. It can be seen that the addition of peptide chains influences the radius strongly. This is in clear contrast to polyethylene, where even strongly stabilised droplets did not exhibit a strongly influenced core radius when looking at absolute temperature values.

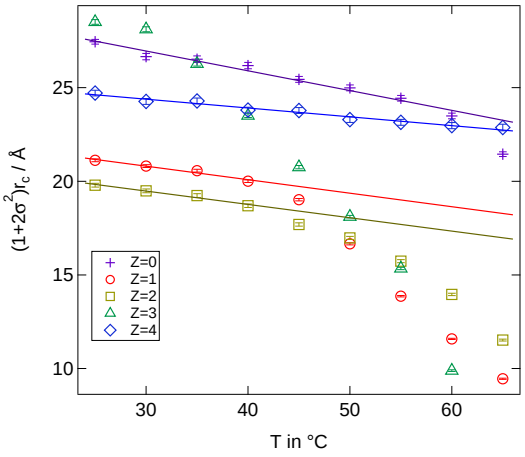

Figure 7.4.: Corrected r_c for microemulsions loaded with different amounts of peptide chains. The lines indicate a linear fit to the data.

Instead such a strong decrease was found for droplets highly destabilised by the addition of many small chains. This would contradict the assumption that the droplets are stabilised by the peptide chains. But it was also found that the radius at T_p for stabilised droplets is smaller and for destabilised droplets larger than in the unloaded case. If the peptide addition would stabilise the droplet it would most likely also increase T_p and thus with increasing number of peptide chains per droplet T_p would also increase and make it necessary to compare radii at higher and higher temperatures.

T_p can not be measured, but the samples show droplet radii that decrease linearly with temperature for almost all samples in the low temperature range. The microemulsion containing three peptide chains per droplet does no exhibit this kind of behaviour at enough temperatures to confidently fit a straight line to the data. Figure 7.5 compares the slopes and intersects for the different samples.

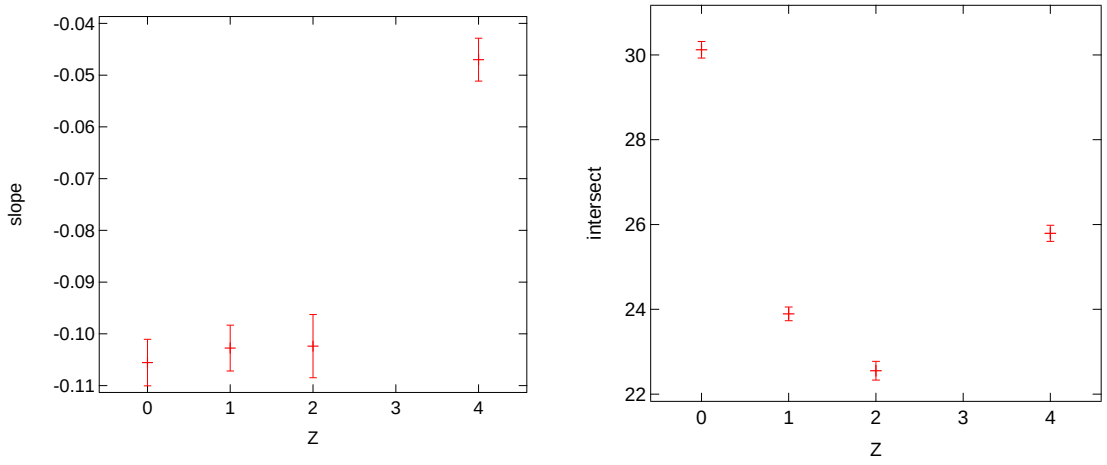

Figure 7.5.: Left: Slope of the radius decrease for different amount of peptide chains per droplet. Right: Intersect of the line fit to the droplet radii at low temperatures.

The slope supports the assumption of a peptide stabilised droplet surfactant shell. For polyethylene glycol loaded droplets it was found that stabilising the droplet causes the radius to decrease slower with increasing temperature and this is again seen here. While the samples with $Z = 1, 2$ show about the same decrease in radius with temperature as the unloaded microemulsion, the sample with $Z = 4$ shows a much slower decrease in radius. Due to the small slope values the intersect does not contain more information than the corrected radius.

So the SAXS investigation shows that the peptide is indeed inside the microemulsion droplet and that the droplet phase prevails through all investigated temperatures (as long as the sample does not separate). It seems that the droplet is stabilised by the interaction

between the peptide and the surfactant shell. To investigate whether the peptide adsorbs at the surfactant layer like polyethylene glycol or stabilises the droplet through some other process, SANS measurements will be used. They might also show, whether the confinement prevents the formation of large peptide chain aggregates and whether the folding process of the peptide is then observable or obstructed by the AOT shell.

7.2 The Peptide in the Soft Confinement of a Microemulsion Droplet Phase

By investigating the peptide loaded deuterated microemulsions with SANS the conformation of the peptide can be studied due to the difference in scattering length density between X-ray and neutron scattering. The samples were measured at 25 °C, 30 °C, 35 °C, 55 °C, 57 °C, 60 °C, 62 °C and 65 °C in order to be comparable to the SANS results from the peptide in buffer measurements and to ensure the existence of the droplet phase. Unlike during the SAXS measurements no separation of the sample components was observed during the measurements, but figure 7.6 shows another problematic effect that occurred.

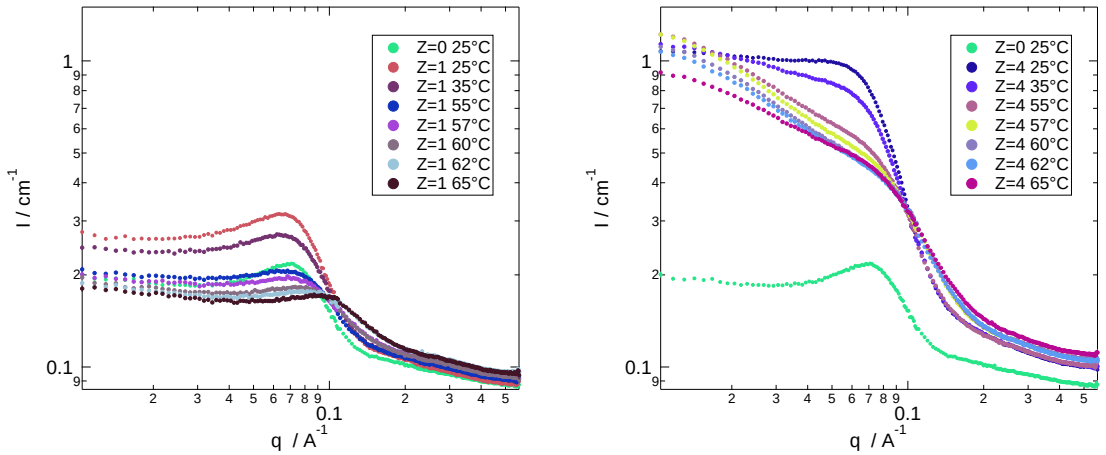

Figure 7.6.: Left: Raw data for the deuterated microemulsion containing one peptide chain compard to the data for $Z = 0$ at 25 °C. Right: Raw data for the deuterated microemulsion containing four peptide chains compard to the data for $Z = 0$ at 25 °C.

It can be seen that the microemulsion containing no peptide chain and thus consisting only of deuterated components shows a very distinct scattering curve. Since the deuteration scheme seems to have worked for the peptide in buffer samples, it can be assumed that there might be a problem with the deuteration inside the octane or the AOT. Protonated AOT would yield a similar contrast situation as present for X-ray scattering. This would enable a description via the model used to describe the SAXS data. But while the model describes the low q range very well it is not able to describe the high q range sufficiently. Even if all fit parameters are left free there is no satisfactory description of the data, implying that there must be a more complex problem in the deuteration scheme. This becomes even more apparent when looking at the temperature dependence of the scattering profiles for the samples with $Z = 1$ and $Z = 4$. The sample containing one peptide chain shows about the same course for all investigated temperatures. There is a plateau followed by a maximum in the low q range and a steep linear fall of intensity in the high q range. The maximum shifts to higher q values with increasing temperatures and decreases in intensity. The decrease is so strong that the intensity of the loaded

microemulsion drops lower than the unloaded microemulsion. So this suggests a temperature effect in scattering curves of the unloaded microemulsion, because the loaded samples contain more protonated molecules and should exhibit a stronger scattering intensity. Still the increase in intensity with increasing peptide concentration suggests that the data contains scattering of the confined peptide. This is further supported by the larger incoherent background that the sample with $Z = 4$ exhibits. Due to the presence of more scattering particles the background increases, the increase is smaller than observed for the bulk samples in the previous chapter, but this is due to the small overall concentration of peptide inside the microemulsion samples. Another interesting effect can be seen in the low q range for high temperatures of the $Z = 4$ sample. There a linear decrease of scattering intensity can be observed which indicates clustering of the scattering particles. This indication is much stronger than the one exhibited in the SAXS measurements or shown by the SANS measurements on the peptide buffer solution. But the intensity for all temperatures lies above the intensity of the unloaded microemulsion, but since there is a clear temperature effect caused by the deuteration scheme problem and not the peptide it would lead to untrustworthy results to just subtract the unloaded microemulsion from data that was not measured at 25 °C. Since the unloaded microemulsion was only measured at 25 °C, because no scattering effect was expected [22], this leaves only the data measured at this temperature. Figure 7.7 shows the unshifted raw data for all samples at 25 °C.

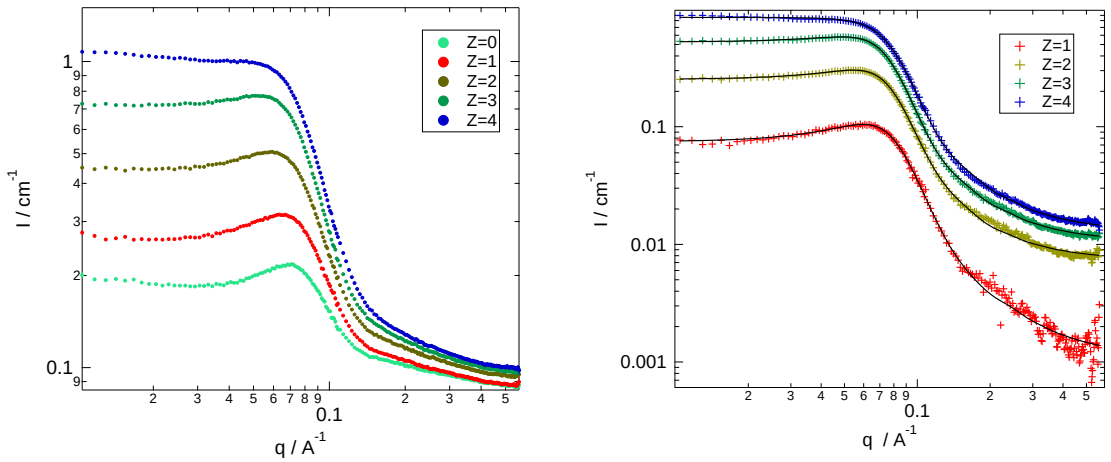

Figure 7.7.: Left: Intensity for all measured samples at 25 °C. Right: Intensity obtained by subtracting the $Z = 0$ data from all samples containing peptide chains at 25 °C. The black lines show the result of the hard sphere model already fitted to the SAXS data.

Looking at all samples at 25 °C reveals that the scattering intensity increases due to the addition of peptide. So the scattering of the peptide is observable as well as the effect of the "failed" deuteration scheme, since the increasing intensity with increasing concentration was also found in the buffer solution. To isolate the peptide scattering from the scattering of its environment the intensity profile from the $Z = 0$ sample is subtracted from the data at 25 °C, shown on the right side of figure 7.7. The obtained data can not be described by the model proposed by Hammouda [105] that was able to describe the bulk data. Instead it can once again be described by the core-shell hard sphere model used to describe the SAXS data of the same samples. Instead of AOT the peptide is assumed to be the shell so the scattering length density and the thickness of the shell is unknown

this time, but kept the same for all samples. This approach is based on the assumption that the peptide adsorbs at the surfactant layer, just like polyethylene glycol[22], due to the many similarities found between the peptide and polyethylene glycol in bulk as well as inside the microemulsion droplet. This model describes the data very well. It yields a shell thickness of 0.80 Å and a scattering length density of 4.26×10^{-6} Å^{-2}. While the obtained scattering length density is plausible, the shell thickness is too small. Since both parameters are unknown and highly correlated it is plausible that a combination of a more physical shell thickness and another scattering length density also describes the data, but the overall result that the peptide adsorbs at the surfactant shell still holds true.
The obtained corrected core radii and hard sphere radii can be compared to the results obtained from the SAXS measurements and this is shown in figure 7.4 on the left side. There it can be seen that the SANS data yields a much more consistent result for the Corrected r_c and r_{HS}, while the SAXS results shows bumps and kinks due the evaporation of the sample. But for the sample with $Z = 4$, where the SAXS measurements seemed to have worked best, both results are in very good agreement and at least for the core radius the difference between SAXS and SANS is not that large. This can be interpreted as the confirmation of the assumption that the peptide adsorbs at the surfactant layer just like polyethylene glycol.

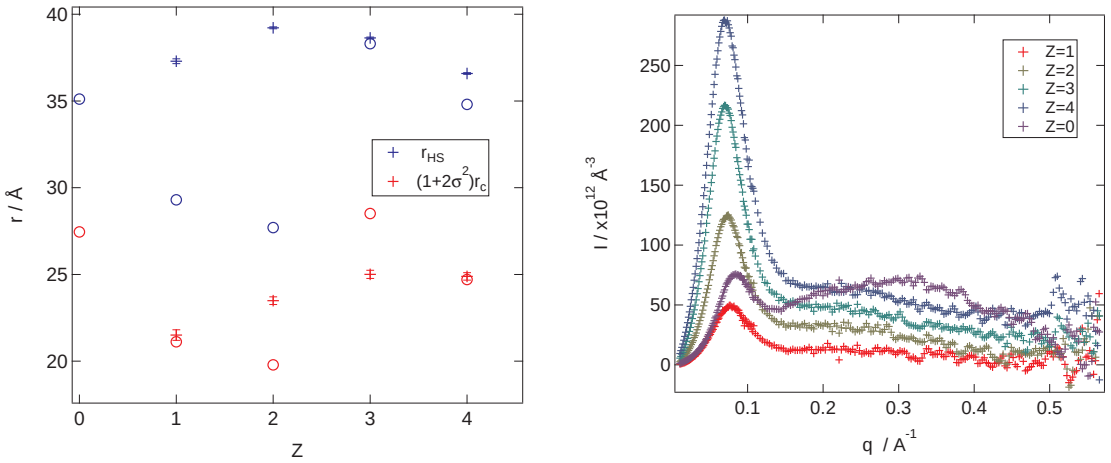

Figure 7.8.: Left: Corrected r_c and r_{HS} for investigated loaded microemulsions at 25 °C. The lines show the results obtained from SAXS measurements. Crosses represent SANS results and circles SAXS results. Right: Kratky plot of the corrected intensities at 25 °C compard to the unloaded microemulsion.

In order to analyse the structural conformation of the peptide chain, figure 7.8 also shows the Kratky plots for the obtained peptide scattering curves. Here the peptide exhibits the form of a spherical/folded particle instead of a flexible one. But the curves do not level out at zero, instead they seem to reach a plateau value in the large q range. The Kratky plot profile of the unloaded microemulsion shows a bell sahpe in the low q range as well followed by an increase. Since the unloaded microemulsion does not contain any peptide and exhibits a peak at the same q value as the loaded microemulsion it can assumed that the peak is caused by the a spherical structure. This would again support the claim that the peptide adsorbs at the surfactant layer, since the peptide should also be unfolded/flexible at 25 °C.

Summary of the Interplay Between AOT Surfactant Shell and the ELP

Despite the various difficulties that occurred during the measurements on the microemulsions containing different amounts of peptide chains, some very interesting and convincing results could be deduced. SAXS investigations revealed that the droplet phase of the microemulsion is present over the entire temperature range of 25 °C - 65 °C. They also showed that the peptide stabilises the droplet and that the stabilisation becomes stronger with increasing number of peptide chains per droplet. The peptide achieves this stabilisation by adsorbing at the surfactant interface. SANS measurements confirmed this, because the scattering of the peptide can be described by a core-shell hard sphere model and the Kratky plot exhibits a peak typical of spherical particles. So the peptide behaves very similar to the polyethylene glycol when confined inside water/AOT/octane microemulsions. Due to the difficulties in the deuteration scheme the influence of confinement on the IIT or conformation of the peptide and changes caused by increasing temperature could not be investigated.

8 Open Questions and Preliminary Results

This thesis dealt with two different systems. First polymer water mixtures were analysed in bulk and confinement and then the same was done for a peptide buffer solution. So future experiments could either explore each system individually and or focus more on finding connections between them. In this chapter ideas for future experiments will be suggested, first for the binary systems and then for the microemulsion samples.

8.1 Open Questions Concerning PEG Water Mixtures

Touching only the polyethylene glycol water system, it would be interesting to expand the study of the phase diagram and the crystallisation behaviour to different chain lengths. There are already phase diagrams for polyethylene glycol with different molecular weight capped with two -OH groups [30,32,82–84]. So PEG with similar molecular weight, but different end groups could be purchased and investigated via DSC, SAXS and WAXS in order to study, if the chain ends or the chain length are responsible for the appearance of two structures in the SAXS measurements. One could also study, if the eutectic temperature becomes more erratic on the polymer rich side with increasing chain length of the dimethyl ether PEG type. In this study the glass transition of the mixtures was ignored due to the accessible temperature range of the DSC set up. Still by investigating the phase diagram separately from the glass transition a second measurements program could be devised for the purpose of examining the glassy state of the mixtures. Since low molecular weight PEG does not crystallise it would be of high interest to see, if this behaviour reflects in any way on the glass transition and if the glass transition becomes weaker with hydrophobic end groups. It would also answer the question, if the mobility of the polymer chain is the deciding factor for the phase and melting behaviour or if the glass transition contributes to it as well.
Another interesting aspect would be a continuing investigation of the preferred orientation growth of the water crystal imposed by the polyethylene glycol present inside the liquid phase surrounding the water crystal on the water rich side of the phase diagram. By extending the accessible angle range, peaks containing a "l" component in their miller indices could be measured and their intensity can be recorded for different concentrations polymer. Further it could be studied, if shorter and longer chains exhibit a similar influence or if different chain lengths promote different preferred growth directions.
Moving away from the static scattering experiments it would also be possible to study the molecular dynamics of the PEG water mixtures, focusing on the slowed down water relaxation that occurs when PEG is introduced into the hydrogen bond network of water. A simple experimental method to investigate the mentioned dynamics would be BDS in the high frequency range. This has already be done, but mostly in the area of the phase diagram where a homogeneous liquid phase exists [11,106–108]. These studies could be

expanded by varying the temperature of the sample in addition to the concentration of polymer[109,110]. One could expect the dynamics to change to the dynamics of a liquid mixture with the eutectic concentration, since all mixtures eventually exhibit a liquid phase with that concentration. It would also be interesting to study, if the onset of the liquidus line can be seen in the hydrogen bond dynamics or if the change rate of the hydrogen bonds is unaffected by the crystallisation of a water/PEG crystal.

8.2 Preliminary Results of further Experminets on ELP-like peptide in buffer solution

The results obtained for the peptide buffer solutions suggest a series of different experiments in order to deepen the knowledge of the structural changes imposed on the peptide by aggregation and the ITT with increasing temperature. Since only the lowest investigated concentration showed any sign of the ITT, it would be of high interest to prepare samples with an even lower concentration of peptide chains. In addition to that, there is also reason to investigate higher concentrations of peptide to study the cluster tendencies. This study found that increasing the concentration leads to larger clusters, but there could be a concentration above which the size of the scattering particle will not increase further or at least deviate from the linear behaviour of the slope of R_G.
Advancing from concentration studies could lead to an investigation of different chain length of peptide. By increasing the number of repeat units the ITT might become more pronounced since more hydrogen bonds could go from hydration shell bonding to intra molecular bonding and thus cause a much more significant decrease in R_G due to the ITT. It might also lead to larger clusters and the aggregation might in turn overshadow the ITT again. Figure 8.1 shows raw data for ELP chains containing 40 and 80 repeat units of the VPGVG block.

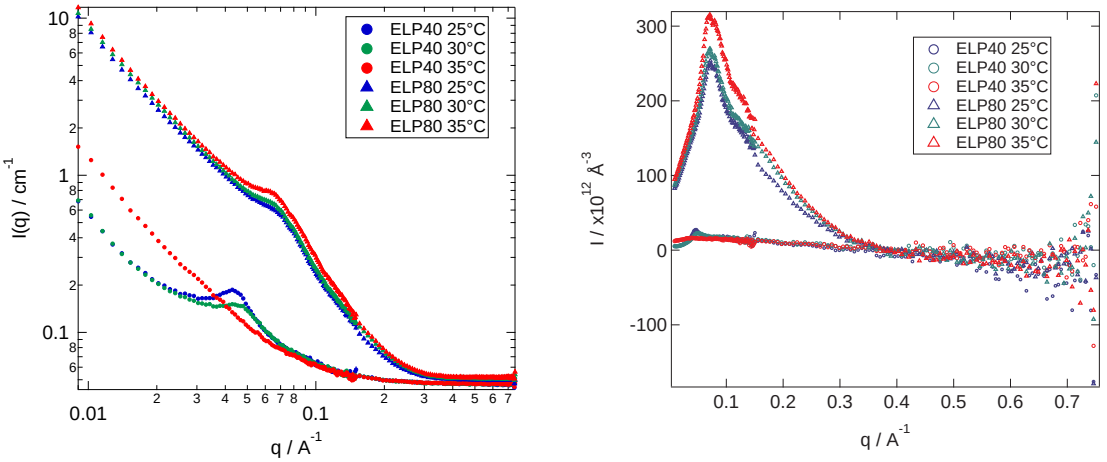

Figure 8.1.: Left: Raw data for ELPs containing 40 and 80 repeat units. Right: Kratky plot for ELPs containing 40 and 80 repeat units.

The raw data differs very much from the raw data recorded for the peptide chain with 3 VPGVG repeat units. In the low q range the data shows a steep increase indicating a strong aggregation, since the LCST should be much lower than for the small chain[15]. Then there is a pronounced peak maximum in the mid q range that disappears at 35 °C

for the peptide with 40 repeat units. It can also be seen that the maximum shifts to higher q with increasing temperature for this peptide, but to lower q for the peptide chain with 80 repeat units. This would indicate that the structure responsible for the peak becomes smaller for the 40 repeat unit peptide and larger for the 80 unit peptide with increasing temperature. Comparing the peak position of the two peptide chains with each other suggests a smaller observed structure for the larger chain. Lebedev et al. proposed that such scattering curves indicate a helical structure in solution or a hollow cylinder [111]. Those first results are very interesting and should be further investigated. This study should also contain some peptide chains with a number of repeat units between 3 and 40 in order to observe the transition from the scattering curves presented in this work (chapter 6) and the ones shown in this chapter.
The right side of figure 8.1 shows the Kratky plot for the two longer peptide chains. There a bell like shape is observed at all measured samples and temperatures, except for the 40 repeat unit chain at 35 °C. This and the position of the peak suggests that it is indeed caused by the structure peak observed in the raw data. The shape of the Kratky curve would indicate a folded spherical particle, which in this case can now either be a spherical cluster of peptide chains or maybe show that the ITT already happened and the chain is in its denser sate. The latter case would be very surprising, since the ITT observed in this work was finished at around 50 °C and said to be around 35 °C for even smaller chains [5]. So it is reasonable to think that larger peptide chains indeed form structures at low temperatures, probably caused by the lower LCST.
Once again in addition to the static structural investigations it would be quite sensible to broaden the knowledge of the behaviour of the peptide with 3 VPGVG repeat units inside a buffer solution by investigating the dynamics of the peptide chain. Due to the salt contained inside the buffer, dielectric experiments are quite difficult due to the high conductivity of the samples. But since the samples are already deuterated, Proton-NMR can be applied in order to observe diffusion coefficients. Figure 8.2 shows the raw data from static field gradient NMR experiments. For a detailed explanation of the pulse sequenced used the reader is referred to [112]

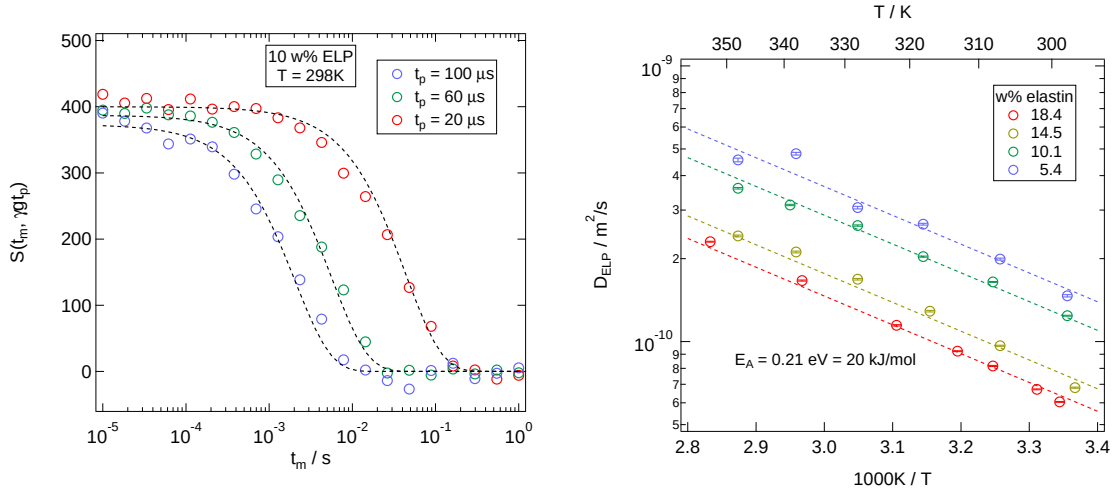

Figure 8.2.: Left: Stimulated echo for the sample with 10 wt% ELP for different t_p. Right: Diffusion coefficient for all ELP bulk samples calculated from [112].

The data exhibits one diffusion process that can be described via the model used by Rosenstihl et al.:[112].

$$\frac{S(t_m, \gamma g t_p)}{S(0, \gamma g t_p)} = exp\left[-(\gamma g t_p)^2 \left(t_m + \frac{2}{3} t_p\right) D\right] \tag{8.1}$$

Where t_m and t_p are the times between the pulses, γ denotes the gyromagnetic ratio, g gives the static field gradient and D is the diffusion coefficient. For every temperature the data is fitted globally for all measured t_p to yield a single diffusion coefficient D. Applying this method to all samples and different temperatures yields the diffusion coefficients displayed on the right side of figure 8.2. It can be seen that the diffusion of the peptide becomes faster with decreasing concentration which was expected due to the smaller R_G of the scattering particles contained in samples with lower concentrations. But the diffusion also becomes faster with increasing temperature, which contradicts the obtained growth in R_G with temperature, not taking the viscosity into account. The decrease in D is linear in an Arrhenius representation and exhibits the same slope for all concentrations, that yields an activation energy of $E_A = 0.21\,\text{eV}$. Due to this decrease it seems that the dynamics investigated are those of a single peptide chain, leading to the assumption that the clusters seen in the static scattering experiments live on time scales long enough to be observed by static scattering, but short enough to enable the observation of single chain dynamics. In order to obtain R_G from D it would be necessary to know the local viscosity, which is very difficult and was not part of this work.
All experiments in this work dealt with a homogeneous peptide buffer liquid and its similarities to water PEG (polymer) mixtures. Thus experiments studying protein crystallisation might be interesting too. The same measurements as done on the PEG water mixtures could be done on the peptide buffer mixtures using SANS and WANS set-ups. Protein crystallisation is well studied[113] and thus it should be possible to derive a peptide crystal from the solutions. These studies can be done using the small peptide or the two larger peptides, but it has to be mentioned that larger macromolecules might not crystallise as well. This would yield information, whether the existence of the ITT also influences the crystallisation behaviour of a protein and if the behaviour upon crystallisation can be compared to that of a polymer in a polymer water mixture (eutectic phase diagram). Protein crystallisation studies would also allow for a combination of both observed binary systems, since PEG is often used as a crystallising agent for protein crystals[114–116].

8.3 Proposal for Experiments on Other Microemulsion Samples

The first thing that comes to mind, when thinking about future experiments with the microemulsion samples, is the failed deuteration scheme and the sample separation in the SAXS set up for the microemulsions containing the ELP. These experiments should obviously be repeated and expanded, measuring the unloaded microemulsion at all investigated temperatures as well. Still based on the results obtained in this work, there are quite a lot of possible experiments that can build on the obtained results, so here only a few will be suggested.
The study of polyethylene glycol in water/AOT/octance microemulsions can be expanded much further to include more different w, different ϕ and even higher number of Z

than investigated in this work. Thus a very detailed picture of the interaction between droplet radius, chain length, number of chain per droplet, chain ends etc. can be obtained, making a calculation of the bending modulus possible[25]. These results can then be complemented by experiments concerning themselves with the dynamics of the surfactant shell and the PEG chains. This has already be done for one molecular weight of PEG by Kuttich et al.[22]. Such measurements can yield information about the influence of chain length (wegde size) on the fluctuations of the surfactant shell and it could be possible to determine if the wedges move alongside the surfactant shell or if a certain chain length is needed in order for the polymer to become mobile.
There is also the possibility of using a co surfactant that shows an even greater attractive interaction with PEG than AOT, for example Ethanol. The surfactant could also be switched completely to Sodium dodecyl sulfate (SDS), whose chemical structure is very similar to AOT. So there are many options that could further expand the understanding of the influence of confinement on the polymer and vice versa.
An even broader spectrum of possible future experiments can be imagined using the peptide containing microemulsion samples. While here too the droplet size, peptide size etc. can be varied, there now arises the question on how to make the investigated system more like a real living cell. The confinement wall could be changed from a single layer to a bilayer, but more intersting would be the addition of other well studied peptides/proteins inside the microemulsion. So by first studying the effect of an increasing peptide length, until the full length of Elastin is reached, in bulk and confinement and then starting to add small peptide sequences from other proteins to the sample, a more and more complete version of a living cell could be achieved. These studies will take quite a bit of time and also expand over many different measurement techniques, but could ultimately lead to the ability of studying more and more life like systems. The results in this work suggest to first focus on the length of the ELP and its concentration in order to obtain a deep knowledge of the clustering and ITT processes and their change in a confinement. It could also be interesting to focus on the interaction between different surfactants and the ELP, since the surfactant interface might block the ITT from taking place and thus keeping Elastin from completing its biological function.
So there are a variety of possible experiments that can build on and expand the results of this thesis and further advance the knowledge about systems relevant to technology and human life in general.

9 Summary

This thesis investigates and compares water mixtures containing the synthetic polymer polyethylene glycol with water mixtures containing a biomolecule made up of an important amino acid sequence of the protein Elastin. These molecules were chosen due to their many similarities and the vast amount of studies concerning themselves with either the polymer or the protein sequence. The mixtures are studied in bulk in order to gain a deeper understanding of their interaction with the hydrogen bond network of water, before both systems are brought into the soft confinement of a water in oil microemulsion droplet. Confinement provided by such a system mimics the confinement exerted by the walls of a living cell. Interactions between the molecule and confinement are observed as well as the change in the behaviour of the molecule the confinement might impose and vice versa.

First the crystallisation and melting behaviour of water polyethylene glycol mixtures and the influence of changing end groups on this behaviour was studied in chapter 4. A combination of DSC, WAXS and SAXS measurements were employed and a phase diagram could be obtained as well as scattering curves revealing the crystalline structures emerging at different temperatures and concentrations. DSC measurements revealed that regardless of end groups an eutectic system is formed and that the eutectic concentration does not change. However the interaction between water and the polymer changes from an attractive one for PEG1500 to a repulsive one for PEGDME1650. This causes a faster separation of the polymer from water and increases the eutectic temperature, since more energy is necessary to dissolve the more hydrophobic PEGDME1650. The diffraction patterns obtained from WAXS measurements showed that there is no evidence for the formation of a solid solution, instead only crystals made up of the pure components form. Analysing the scattering curves also led to two discoveries. First that there is a continuous melting process taking place above the eutectic temperature, where the crystal of the major phase dissolves piece by piece with increasing temperature. Second depending on the polymer concentration and end groups there appears a preferred growth direction of the crystal formed by the major phase. On the water rich side of the phase diagram PEG1500 and PEGDME1650 entice the hexagonal ice crystal to grow along the a- and c-axis. On the polymer rich side only water PEGDME1650 mixtures exhibit a preferred growth direction when analysing the [120] of the pure polymer crystal. With SAXS measurements showing the formation of two lamellar phases for PEGDME1650 and only one for PEG1500, this preferred growth is attributed to the larger structure found in PEGDME1650 that apparently exhibits such a preference. SAXS measurements also revealed that the crystalline phase of the semi crystalline polymer increases in size with the addition of water and that the continuous melting process causes an even further increase in the thickness of the lamellae. So there is a rearranging process taking place inside the polymer crystal that is caused by the changing concentration of polymer in the surrounding liquid phase.

The following chapter 5 dealt with the interaction between the surfactant AOT of the microemulsion and polyethylene glycol of different molecular weights and chain ends. Using

BDS and SAXS measurements the percolation behaviour of the samples could be analysed and connected to the structural changes, allowing for a determination of the surfactant shell stability. Percolation temperatures of loaded water in oil microemulsion droplets are highly influenced by the length and number of the polymer chains inside the droplet, but changing from PEG to PEGDME showed no significant difference in the percolation behaviour. So the attractive interaction between the polymer and the surfactant is most likely caused by the structure of the monomer and its ability to form hydrogen bonds. Analysing the results obtained by BDS yielded that adding polyethylene glycol inside the droplet induces a destabilising and a stabilising interaction. While the droplet is destabilised due to the polymer wedging itself between AOT headgroups it is also stabilised by that process since head groups are connected via the polymer chain. It was found that a complex interplay between the number of wedges(polymer chains) per droplet, their length and the droplet radii determines if the percolation temperature of the microemulsion is increased or decreased. Structural analysis with SAXS measurements revealed that the droplet phase is present throughout the entire observed temperature range. The scattering data showed no significant sign of a clustering process and the description with a core shell form factor and a hard sphere structure factor was sufficient. From this model the droplet polydispersity and radii could be extracted. All samples exhibited a polydispersity above 0.2, but the most destabilised or stabilised samples showed a much higher polydispersity, attributed to their influence on the surfactant shell. The radii of the droplet of the microemulsions samples decreases linearly with temperature, whereas destabilised droplets exhibited a faster decrease than the unloaded droplets and stabilised droplets showed a slower decrease. At the percolation temperature destabilised droplets show a larger radius than stabilised droplets. So results obtained by SAXS measurements were in good agreement with the proposed wedge model.
In chapter 6 the structure of an Elastin-like peptide in a buffer solution was analysed using SANS measurements in order to study the influence of a possible ITT and the LCST on the ELP. The scattered intensity of the samples increased with increasing temperature and concentration and revealed tendencies to aggregate at very low q. Employing a Guinier approach a at low q a radius of gyration could be obtained. Analysing this structural property showed the peptide formed clusters that increased in size with increasing temperature, but at any given temperature there exists an ideal cluster size with a certain radius of gyration. Only for low concentrations the influence of the ITT could be found in the radius of gyration, revealing an ITT temperature of about 50 °C. Further analysing the structure of the ELP inside a Kratky plot showed no sign of a folding process taking place, but instead that the peptide behaves strongly like a perturbed Gaussian coil. This result allowed for the use of an extended Debye model containing the Flory parameter to describe the data imposing the structure of a polymer coil. The radius of gyration was obtained from this approach shows the same behaviour as the radius obtained from the Guinier approach, but the model extrapolates to higher radii and shows no sign of the ITT. But studying the difference of the two approaches as well as the Flory parameter once again revealed a significant change in behaviour at 50 °C. The model also showed that the lowest concentration deviates more from the Gaussian coil than the other, further illustrating its special status. Implementing a new set of invariants and variables introduced in literature [80,104] allowed for the calculation of the mass of the scattering particle, by exploiting the protein nature of the ELP to obtain important parameters. The mass of

the scattering particle showed that in the case of the lowest concentration the scattering observed was the scattering of a single particle. Clusters formed at higher concentrations and temperatures do contain about 2-4 peptide chains, which seems to be enough to overshadow the ITT.
Finally the effect of soft confinement on the ELP structure and vice versa was studied in chapter 7 with SANS and SAXS measurements. Due to the occurring problems with the deuteration scheme and the SAXS measurements, the amount of reliable data was reduced, but still yielded interesting results. Once again SAXS data could be described with the core shell hard sphere model that also described the polymer loaded microemulsions. The presence of a droplet phase could be confirmed for all temperatures and concentrations observed. Comparing the polydispersity and droplet radii od the ELP loaded microemulsions to the polymer loaded ones allowed for the deduction of an unaffected or stabilised droplet depending on the concentration of ELP. The scattering curves of the ELP in soft confinement could not be compared to the scattering curves from the bulk solution due to their large differences. Instead the ELP curves could be described by the same core shell hard sphere model as the droplet scattering observed with SAXS measurements. The radii obtained using this model on the ELP data are very close to the droplet radii and thus it was deduced that the ELP adsorbs at the surfactant interface, just like polyethylene glycol. Ths assumption is supported by the Kratky plot who reveals a spherical shape of the scattering particle on the same length scale as the confinement.
Concluding it can be said that simultaneously studying biomolecules and synthetic polymers with similar properties can help to understand the behaviour of the biomolecule. By studying the polymer water mixtures extensively and obtaining important findings about many different processes, it was possible to deduce a similar amount of important findings for a peptide water mixture with less data. This can be very useful, if the production process of the biomolecule is very elaborate. This work analysed the interaction between polyethylene glycol and the hydrogen bond network of water as well as its interaction with the surfactant AOT of a water, AOT and octane microemulsions and used the results obtained to describe the interaction of an ELP with the same surroundings. But due to the differences between polymers and biomolecules there are some processes that can not be described using the methods derived for describing polymers. The ITT of the ELP could only be observed using a model free Guinier approach for scattering particles, while the model imposing a polymer like behaviour failed to detect the ITT. This work also showed the importance of studying the influence of confinement on polymers and biomolecules, since it is the future aim to be able to study more life-like systems. The choice of confinement structure and its composition highly influence the structure and behaviour of the confined molecules and in the case of the ELP might even prevent the ITT and thus its biological function. To study such systems could also be interesting in order to learn more about the ITT in general, but would not be characterised as life-like. So it is very important to further study confinement effects on biomolecules and polymers in order to study similarities between these two very different type of molecules.

A Appendix

A.1 Scattering Length Densities of Octane and Water

Table A.1.: The scattering length densities for water, deuterated water, octance and deuterated octane. Scattering length densities are calculated based on the denstiy and chemical strucuture of the substance by the *scattering length calculator* form the *NIST Center for Neutron Research*.

substance	$SLD_{Neutrons}/10^{-6}\,1/Å^{-2}$	$SLD_{X\text{-}rays}/10^{-6}\,1/Å^{-2}$
water	-0.56	9.47
d-water	6,34	9.47
octane	-0.52	6.88
d-octane	6.48	6.97

A.2 Scattering Length Densities of the AOT Head and Tail Group

Table A.2.: The X-ray scattering length densities for the tail and head group of the surfactant AOT and its deuterated version. For the head group the SLD for the AOT was taken from literature [25,117,118] and the SLD of the deuterated head group was set to the same value. The SLD for the tail group and deuterated tail groud were set to the values of octance and d-octance.

substance	$SLD_{X\text{-}rays}/10^{-6}\,1/Å^{-2}$
AOT head group	23.8
d-AOT head group	23.8
AOT tail group	6.88
d-AOT tail group	6.97

Bibliography

[1] Kessel A, Ben-Tal N. Introduction to Proteins: Structure, Function, and Motion. Chapman & Hall/CRC Mathematical and Computational Biology. CRC Press, 2010. ISBN 9781439810729.

[2] Buxbaum E. Fundamentals of Protein Structure and Function. Springer, Boston, MA, 2007. ISBN 9780387684802.

[3] Buchner R, Barthel J, Stauber J. The dielectric relaxation of water between 0°C and 35°C. *Chemical Physics Letters*, 306(June):57–63, 1999.

[4] Fortes AD, Wood IG, Grigoriev D, *et al.* No evidence for large-scale proton ordering in Antarctic ice from powder neutron diffraction. *Journal of Chemical Physics*, 120(24):11376–11379, 2004. ISSN 00219606.

[5] Nicolini C, Ravindra R, Ludolph B, *et al.* Characterization of the Temperature- and Pressure-Induced Inverse and Reentrant Transition of the Minimum Elastin-Like Polypeptide GVG (VPGVG) by DSC , PPC , CD , and FT-IR Spectroscopy. *Biophysical Journal*, 86(3):1385–1392, 2004. ISSN 0006-3495.

[6] Erlkamp M, Grobelny S, Winter R. Crowding effects on the temperature and pressure dependent structure, stability and folding kinetics of Staphylococcal Nuclease. *Physical Chemistry Chemical Physics*, 16(13):5965–5976, 2014. ISSN 14639076.

[7] Strobl G. The Physics of Polymers: Concepts for Understanding Their Structures and Behavior. Springer Berlin Heidelberg, 2013. ISBN 9783662032435.

[8] Ruff KM, Roberts S, Chilkoti A, *et al.* Advances in Understanding Stimulus Responsive Phase Behavior of Intrinsically Disordered Protein Polymers. *Journal of Molecular Biology*, 2018. ISSN 00222836.

[9] Hocine S, Li MH. Thermoresponsive self-assembled polymer colloids in water. *Soft Matter*, 9(25):5839–5861, 2013. ISSN 1744683X.

[10] Pappu RV, Wang X, Vitalis A, *et al.* A polymer physics perspective on driving forces and mechanisms for protein aggregation. *Archives of Biochemistry and Biophysics*, 469(1):132–141, 2008. ISSN 1096-0384; 0003-9861.

[11] Hanke E, Schulz U, Kaatze U. Molecular Interactions in Poly(ethylene glycol)-Water Mixtures at Various Temperatures: Density and Isentropic Compressibility Study. *ChemPhysChem*, 8(4):553–560, 2007. ISSN 1439-7641.

[12] Hammouda B, Ho D, Kline S. Insight into Clustering in Poly(ethylene oxide) Solutions. *Macromolecules*, 37(18):6932–6937, 2004.

[13] Kjellander R, Florin E. Water structure and changes in thermal stability of the system poly(ethylene oxide-water. *Journal of the Chemical Society, Faraday Transactions 1: Physical Chemistry in Condensed Phases*, 77(9):2053, 1981. ISSN 0300-9599.

[14] Urry DW, Hayes LC, Gowda D, *et al.* Reduction-driven polypeptide folding by the ΔTt mechanism. *Biochemical and Biophysical Research Communications*, 188(2):611–617, 1992. ISSN 0006291X.

[15] Zhao B, Li NK, Yingling YG, *et al.* LCST Behavior is Manifested in a Single Molecule: Elastin-Like polypeptide (VPGVG)n. *Biomacromolecules*, 17(1):111–118, 2016. ISSN 15264602.

[16] Kyte J, Doolittle RF. A simple method for displaying the hydropathic character of a protein. *Journal of Molecular Biology*, 157(1):105–132, 1982. ISSN 00222836.

[17] Li NK, Quiroz FG, Hall CK, *et al.* Molecular Description of the LCST Behavior of an Elastin-Like Polypeptide. *Biomacromolecules*, 15(10):3522–3530, 2014. ISSN 1525-7797.

[18] Meier W. Poly(oxyethylene) Adsorption in Water/Oil Microemulsions: A Conductivity Study. *Langmuir*, 12(5):1188–1192, 1996. ISSN 0743-7463.

[19] Domschke M, Kraska M, Feile R, *et al.* AOT microemulsions: droplet size and clustering in the temperature range between the supercooled state and the upper phase boundary. *Soft Matter*, 9(48):11503, 2013. ISSN 1744-683X.

[20] Wipf R, Jaksch S, Stühn B. Dynamics in water-AOT-n-decane microemulsions with poly(ethylene glycol) probed by dielectric spectroscopy. *Colloid and Polymer Science*, 288(5):589–601, 2010. ISSN 0303-402X.

[21] Kuttich B, Falus P, Grillo I, *et al.* Form fluctuations of polymer loaded spherical microemulsions studied by neutron scattering and dielectric spectroscopy. *Journal of Chemical Physics*, 141(8), 2014. ISSN 00219606.

[22] Kuttich B, Grillo I, Schöttner S, *et al.* Polymer conformation in nanoscopic soft confinement. *Soft Matter*, 13(38):6709–6717, 2017. ISSN 1744-683X.

[23] Schübel D, Ilgenfritz G. Influence of Polyethylene Glycols on the Percolation Behavior of Anionic and Nonionic Water-in-Oil Microemulsions. *Langmuir*, 13(16):4246–4250, 1997. ISSN 0743-7463.

[24] Stubenrauch C. Microemulsions: Background, New Concepts, Applications, Perspectives. Wiley, 2009. ISBN 9781405167826.

[25] Kuttich B, Grefe Ak, Stühn B. Changes in the bending modulus of AOT based microemulsions induced by the incorporation of polymers in the water core. *Soft Matter*, 12(30):6400–6411, 2016. ISSN 1744-683X.

[26] Jones R. Soft Condensed Matter. Oxford Master Series in Physics. OUP Oxford, 2002. ISBN 9780198505891.

[27] Aharony A, Stauffer D. Introduction To Percolation Theory. Taylor & Francis, 2003. ISBN 9781135747831.

[28] Chaikin P, Lubensky T. Principles of Condensed Matter Physics. Cambridge University Press, 2000. ISBN 9780521794503.

[29] Bae YC, Shim JJ, Soane DS, *et al.* Representation of vaporliquid and liquid-liquid equilibria for binary systems containing polymers: Applicability of an extended flory-huggins equation. *Journal of Applied Polymer Science*, 47(7):1193–1206, 1993. ISSN 1097-4628.

[30] Huang L, Nishinari K. Interaction between poly(ethylene glycol) and water as studied by differential scanning calorimetry. *Journal of Polymer Science, Part B: Polymer Physics*, 39(5):496–506, 2001. ISSN 08876266.

[31] Smith P, Pennings A. Eutectic crystallization of pseudo binary systems of polyethylene and high melting diluents. *Polymer*, 15(7):413 – 419, 1974. ISSN 0032-3861.

[32] Hey M, M Ilett S. Poly(ethylene oxide) hydration studied by differential scanning calorimetry. *Journal of the Chemical Society Faraday Transactions*, 87:3671–3675, 1991.

[33] Gundert F. Polymer handbook. 3rd edition. J. BRANDRUP and E. H. IMMERGUT (editors). *Acta Polymerica*, 41(6):361–362, 1990. ISSN 1521-4044.

[34] Israelachvili J. The different faces of poly(ethylene glycol). *Proceedings of the National Academy of Sciences*, 94(16):8378–8379, 1997. ISSN 0027-8424.

[35] Perticaroli S, Ehlers G, Jalarvo N, *et al.* Elasticity and Inverse Temperature Transition in Elastin. *The Journal of Physical Chemistry Letters*, 4018–4025, 2015. ISSN 1948-7185.

[36] Urry DW, Hugel T, Seitz M, *et al.* Elastin: a representative ideal protein elastomer. *Philosophical transactions of the Royal Society of London Series B, Biological sciences*, 357(1418):169–184, 2002. ISSN 0962-8436.

[37] Ma X, Sun C, Huang J, *et al.* Thermal hysteresis in the backbone and side-chain dynamics of the elastin mimetic peptide [VPGVG]3 revealed by 2H NMR. *Journal of Physical Chemistry B*, 116(1):555–564, 2012. ISSN 15205207.

[38] Helfrich, W. Elastic Properties of Lipid Bilayers-Theory and Possible Experiments. *Zeitschrift fur Naturforschung Teil C Biochemie Biophysik Biologie Virologie*, 28:693–703, 1973. ISSN 1932-1058.

[39] Christen H, Eicke HF, Hammerich H, *et al.* Kalorimetrische Untersuchungen des Wassereinflusses auf den Lösungsvorgang von Aerosol OT in apolaren Lösungsmitteln. *Helvetica Chimica Acta*, 59(4):1297–1306, 1976. ISSN 15222675.

[40] Eicke, H and Zinsli, P. Nanosecond spectroscopic investigations of molecular processes in W/O microemulsions. *Journal of Colloid and Interface Science*, 65:131–140, 1978.

[41] Kotlarchyk M, Chen SH, Huang JS. Temperature dependence of size and polydispersity in a three-component microemulsion by small-angle neutron scattering. *The Journal of Physical Chemistry*, 86(17):3273–3276, 1982. ISSN 0022-3654.

[42] Kotlarchyk M, Chen SH. Critical behavior of a microemulsion studied by small angle neutron scattering. *Physical Review A*, 28(1):508–511, 1983. ISSN 0556-2791.

[43] Kotlarchyk M, Chen SH, Huang JS, *et al.* Structure of three-component microemulsions in the critical region determined by small-angle neutron scattering. *Physical Review A*, 29(4):2054–2069, 1984. ISSN 10502947.

[44] Endo H, Allgaier J, Gompper G, *et al.* Membrane decoration by amphiphilic block copolymers in bicontinuous microemulsions. *Physical Review Letters*, 85(1):102–105, 2000. ISSN 00319007.

[45] Jakobs B, Sottmann T, Strey R, *et al.* Amphiphilic block copolymers as efficiency boosters for microemulsions. *Langmuir*, 15(20):6707–6711, 1999. ISSN 07437463.

[46] Lianos P, Modest S, Staikos G, *et al.* Interaction of Poly(oxyethylene glycol) with Cyclohexane-Pentanol-Sodium Dodecyl Sulfate Water-in-Oil Microemulsions. *Langmuir*, 8(4):1054–1059, 1992. ISSN 15205827.

[47] Schübel D, Bedford OD, Ilgenfritz G, *et al.* Oligo- and polyethylene glycols in water-in-oil microemulsions. A SANS study. *Physical Chemistry Chemical Physics*, 1(10):2521–2525, 1999. ISSN 14639076.

[48] Geethu PM, Yadav I, Aswal VK, *et al.* Enhancement in Elastic Bending Rigidity of Polymer Loaded Reverse Microemulsions. *Langmuir*, 33(45):13014–13026, 2017. ISSN 15205827.

[49] Chen SH. Small Angle Neutron Scattering Studies of the Structure and Interaction in Micellar and Microemulsion Systems. *Annual Review of Physical Chemistry*, 37(1):351–399, 1986. ISSN 0066-426X.

[50] Ashcroft NW, Lekner J. Structure and Resistivity of Liquid Metals. *Physical Review*, 145(1):83–90, 1966. ISSN 0031-899X.

[51] Milner ST, Safran SA. Dynamical fluctuations of droplet microemulsions and vesicles. *Physical Review A*, 36(9):4371–4379, 1987. ISSN 10502947.

[52] Komura S, Seki K. Dynamical fluctuations of spherically closed fluid membranes. *Physica A: Statistical Mechanics and its Applications*, 192(1-2):27–46, 1993. ISSN 03784371.

[53] Kawabata Y, Nagao M, Seto H, *et al.* Temperature and Pressure Effects on the Bending Modulus of Monolayers in a Ternary Microemulsion. *Physical Review Letters*, 92(5):4, 2004. ISSN 10797114.

[54] Bartlett P, Ottewill RH. A neutron scattering study of the structure of a bimodal colloidal crystal. *The Journal of Chemical Physics*, 96(4):3306–3318, 1992. ISSN 00219606.

[55] Zimm BH. The scattering of light and the radial distribution function of high polymer solutions. *The Journal of Chemical Physics*, 16(12):1093–1099, 1948. ISSN 00219606.

[56] D'Arrigo G, Paparelli A, D'Aprano A, *et al.* Ultrasonic investigation of dynamic properties of the water/AOT/n-heptane system. *Journal of Physical Chemistry*, 93(26):8367–8370, 1989. ISSN 00223654.

[57] Spehr TL, Frick B, Zamponi M, *et al.* Dynamics of water confined to reverse AOT micelles. *Soft Matter*, 7(12):5745, 2011. ISSN 1744-683X.

[58] Tatam R, Champion J. Depolarized Rayleigh-Brillouin scattering studies of isomers of the homologous alkanes series n-pentane to n-octane. *Molecular Physics*, 60(2):291–317, 1987. ISSN 0026-8976.

[59] Huang JS, Milner ST, Farago B, *et al.* Study of Dynamics of Microemulsion Droplets by Neutron Spin-Echo Spectroscopy. *Physical Review Letters*, 59(22):2600–2603, 1987. ISSN 0031-9007.

[60] Cazabat A, Chatenay D, Langevin D, *et al.* Light scattering study of microemulsions and its relation to percolation phenomena. *Journal de Physique Lettres*, 41(18):441–445, 1980. ISSN 0302-072X.

[61] Carlstrom G, Halle B. Shape Fluctuations and Water Diffusion in Microemulsion Droplets . A Nuclear Spin Relaxation Study. *Journal of Physical Chemistry*, 93(20):3287–3299, 1989. ISSN 00223654.

[62] Kraska M, Kuttich B, Stühn B. Bottom-Up Self-Organization in Supramolecular Soft Matter: Principles and Prototypical Examples of Recent Advances, Chapter 2: Aggregate Structure and Dynmaic Percolation in Microemulsions. Springer Series in Materials Science. Springer International Publishing, 2015. ISBN 9783319194103.

[63] Grest GS, Webman I, Safran SA, *et al.* Dynamic percolation in microemulsions. *Physical Review A*, 33(4):2842–2845, 1986. ISSN 0556-2791.

[64] Fletcher PDI, Howe AM, Robinson BH. The kinetics of solubilisate exchange between water droplets of a water-in-oil microemulsion. *Journal of the Chemical Society, Faraday Transactions 1: Physical Chemistry in Condensed Phases*, 83(4):985, 1987. ISSN 0300-9599.

[65] De Gennes PG, Taupin C. Microemulsions and the flexibility of oil/water interfaces. *The Journal of Physical Chemistry*, 86(13):2294–2304, 1982. ISSN 0022-3654.

[66] Gompper G, M KD. Statistical Mechanics Of Membranes And Surfaces: 2nd Edition, Chapter 12: Triangulated Surface Models of Fluctuating Membranes. World Scientific Publishing Company, 2004. ISBN 9789814483223.

[67] Weißheit S, Kahse M, Kämpf K, *et al.* Elastin-like Peptide in Confinement: FT-IR and NMR T1 Relaxation Data. *Zeitschrift für Physikalische Chemie*, 2018. ISSN 2196-7156.

[68] Bates R, Acree S. pH values of certain phosphate-chloride mixtures, and the second dissociation constant of phosphoric acid from 0 degrees to 60 degrees C. *Journal of Research of the National Bureau of Standards*, 30(2):129, 1943. ISSN 0091-0635.

[69] Van Dijk Ma, Joosten JGH, Levine YK, *et al.* Dielectric study of temperature-dependent aerosol OT/water/isooctane microemulsion structure. *The Journal of Physical Chemistry*, 93(6):2506–2512, 1989. ISSN 0022-3654.

[70] Trickett K, Brice H, Myakonkaya O, *et al.* Microemulsion-based organogels containing inorganic nanoparticles. *Soft Matter*, 6(6):1291–1296, 2010. ISSN 1744-6848.

[71] Tanaka S. Theory of power-compensated DSC. *Thermochimica Acta*, 210:67 – 76, 1992. ISSN 0040-6031.

[72] Kremer F, Schönhals A. Broadband Dielectric Spectroscopy. Springer Berlin Heidelberg, 2012. ISBN 9783642561207.

[73] Böttcher C, Rip A, van Belle O, *et al.* Theory of Electric Polarization: Dielectrics in time-dependent fields. Theory of Electric Polarization. Elsevier Scientific Publishing Company, 1973. ISBN 9780711002654.

[74] Wagner H, Richert R. Equilibrium and Non-Equilibrium Type β-Relaxations: d -Sorbitol versus o -Terphenyl. *The Journal of Physical Chemistry B*, 103(20):4071–4077, 1999. ISSN 1520-6106.

[75] Lechner M, Wohlfarth C. Static Dielectric Constants of Pure Liquids and Binary Liquid Mixtures: Supplement to IV/6. Landolt-Börnstein: Numerical Data and Functional Relationships in Science and Technology - New Series. Springer Berlin Heidelberg, 2008. ISBN 9783540755050.

[76] Roe R. Methods of X-ray and Neutron Scattering in Polymer Science. ACS symposium series. Oxford University Press, 2000. ISBN 9780195113211.

[77] Zemb T, Lindner P. Neutrons, X-rays and Light: Scattering Methods Applied to Soft Condensed Matter. North-Holland delta series. Elsevier, 2002. ISBN 9780444511225.

[78] Guinier A. X-ray Diffraction in Crystals, Imperfect Crystals, and Amorphous Bodies. Dover Books on Physics Series. Dover Publications, 1994. ISBN 9780486680118.

[79] Hunklinger S. Festkörperphysik. de Gruyter Studium. Walter de Gruyter GmbH, 2017. ISBN 9783110567755.

[80] Glatter O, Kratky O. Small Angle X-ray Scattering. Academic Press, 1982. ISBN 9780122862809.

[81] Kline SR. Reduction and analysis of SANS and USANS data using IGOR Pro. *Journal of Applied Crystallography*, 39(6):895–900, 2006. ISSN 0021-8898.

[82] Bogdanov B, Mihailov M. Melting of water/poly(ethylene oxide) systems. *Journal of Polymer Science: Polymer Physics Edition*, 23(10):2149–2158, 1985. ISSN 00981273.

[83] Hager SL, Macrury TB. Investigation of phase behavior and water binding in poly(alkylene oxide) solutions. *Journal of Applied Polymer Science*, 25(8):1559–1571, 1980. ISSN 00218995.

[84] De Vringer T, Joostenl JGH, Junginger HE. A study of the hydration of polYoxyethylene_ at low temperatures by differential scanning calorimetry. *Colloid & Polymer Science Colloid & Polymer Sci*, 264:623–630, 1986. ISSN 0303-402X.

[85] Ginés JM, Arias MJ, Rabasco AM, *et al.* Thermal characterization of polyethylene glycols applied in the pharmaceutical technology using differential scanning calorimetry and hot stage microscopy. *Journal of Thermal Analysis*, 46(1):291–304, 1996. ISSN 0368-4466.

[86] Pielichowski K, Flejtuch K. Differential scanning calorimetry studies on poly(ethylene glycol) with different molecular weights for thermal energy storage materials. *Polymers for Advanced Technologies*, 13(10-12):690–696, 2002. ISSN 1042-7147.

[87] Kraus W, Nolze G. POWDER CELL - a program for the representation and manipulation of crystal structures and calculation of the resulting X-ray powder patterns. *Journal of Applied Crystallography*, 29(3):301–303, 1996. ISSN 0021-8898.

[88] Fuentes-Landete V, Mitterdorfer C, Handle P, *et al.* Crystalline and amorphous ices. 187:173–208, 2015.

[89] Uchida T, Takeya S. Powder X-ray diffraction observations of ice crystals formed from disaccharide solutions. *Physical Chemistry Chemical Physics*, 12(45):15034, 2010. ISSN 1463-9076.

[90] Malkin TL, Murray BJ, Andrey V, *et al.* Correction for Malkin et al., Structure of ice crystallized from supercooled water. *Proceedings of the National Academy of Sciences*, 109(10):4020–4020, 2012. ISSN 0027-8424.

[91] Malkin TL, Murray BJ, Salzmann CG, *et al.* Stacking disorder in ice I. *Physical Chemistry Chemical Physics*, 17(1):60–76, 2015. ISSN 1463-9076.

[92] Takahashi Y, Tadokoro H. Structural Studies of Polyethers, (-(CH 2)m-O-) n . X. Crystal Structure of Poly(ethylene oxide). *Macromolecules*, 6(5):672–675, 1973. ISSN 0024-9297.

[93] De Gennes PG. Interactions between polymers and surfactants. *The Journal of Physical Chemistry*, 94(22):8407–8413, 1990. ISSN 0022-3654.

[94] Papoutsi D, Lianos P, Brown W. Interaction of Polyethylene Glycol with Water-in-Oil Microemulsions. 3. Effect of Polymer Size and Polymer Concentration. *Langmuir*, 10(10):3402–3405, 1994. ISSN 0743-7463.

[95] Suarez MJ, Levy H, Lang J. Effect of addition of polymer to water-in-oil microemulsions on droplet size and exchange of material between droplets. *The Journal of Physical Chemistry*, 97(38):9808–9816, 1993. ISSN 0022-3654.

[96] Israelachvili JN, Marčelja S, Horn RG. Physical principles of membrane organization, volume 13. 1980. ISBN doi:10.1017/S0033583500001645.

[97] Mitchell DJ, Ninham BW. Micelles, vesicles and microemulsions. *Journal of the Chemical Society, Faraday Transactions*, 77(4):601, 1981. ISSN 0300-9238.

[98] Krukau A, Brovchenko I, Geiger A. Temperature-induced conformational transition of a model elastin-like peptide GVG(VPGVG)3 in water. *Biomacromolecules*, 8:2196–2202, 2007. ISSN 15257797.

[99] Schreiner E, Nicolini C, Ludolph B, *et al.* Folding and unfolding of an elastinlike oligopeptide: "inverse temperature transition," reentrance, and hydrogen-bond dynamics. *Physical Review Letters*, 92(14):148101–1, 2004. ISSN 00319007.

[100] Rousseau R, Schreiner E, Kohlmeyer A, *et al.* Temperature-Dependent Conformational Transitions and Hydrogen-Bond Dynamics of the Elastin-Like Octapeptide GVG(VPGVG): A Molecular-Dynamics Study. *Biophysical Journal*, 86(3):1393–1407, 2004. ISSN 00063495.

[101] Li B, Alonso DO, Daggett V. The molecular basis for the inverse temperature transition of elastin. *Journal of Molecular Biology*, 305(3):581–592, 2001. ISSN 00222836.

[102] Durand D, Vivès C, Cannella D, *et al.* NADPH oxidase activator p67phox behaves in solution as a multidomain protein with semi-flexible linkers. *Journal of Structural Biology*, 169(1):45 – 53, 2010. ISSN 1047-8477.

[103] Rambo RP, Tainer JA. Characterizing flexible and intrinsically unstructured biological macromolecules by SAS using the Porod-Debye law. *Biopolymers*, 95(8):559–571, 2011. ISSN 00063525.

[104] Rambo RP, Tainer Ja. Accurate assessment of mass, models and resolution by small-angle scattering. *Nature*, 496(7446):477–81, 2013. ISSN 1476-4687.

[105] Hammouda B. SANS from homogeneous polymer mixtures: A unified overview, 87–133. Springer Berlin Heidelberg, Berlin, Heidelberg, 1993. ISBN 978-3-540-47477-7.

[106] Shinyashiki N, Asaka N, Mashimo S, *et al.* Dielectric study on dynamics of water in polymer matrix using a frequency range 10 6 â10 10 Hz. *The Journal of Chemical Physics*, 93(1):760–764, 1990. ISSN 0021-9606.

[107] Sengwa RJ. Solvent effects on microwave dielectric relaxation in poly(ethylene glycols). *Polymer International*, 45(1):43–46, 1998. ISSN 09598103.

[108] Sato T, Niwa H, Chiba A, *et al.* Dynamical structure of oligo(ethylene glycol)s-water solutions studied by time domain reflectometry. *The Journal of Chemical Physics*, 108(10):4138, 1998. ISSN 00219606.

[109] Kuttich B, Matt A, Weber A, *et al.* Water/PEG Mixtures: Phase Behavior, Dynamics and Soft Confinement. *Zeitschrift für Physikalische Chemie*, 2017.

[110] Miyara M, Takashima I, Sasaki K, *et al.* Dynamics of Uncrystallized Water in Partially Crystallized Poly(ethylene glycol)Water Mixtures Studied by Dielectric Spectroscopy. *Polymer Journal*, 49:511–518, 2017.

[111] Lebedev D, Baitin D, Islamov A, *et al.* Analytical model for determination of parameters of helical structures in solution by small angle scattering: comparison of RecA structures by SANS. *FEBS Letters*, 537(1):182 – 186, 2003. ISSN 0014-5793.

[112] Rosenstihl M, Vogel M. Static and pulsed field gradient nuclear magnetic resonance studies of water diffusion in protein matrices. *The Journal of Chemical Physics*, 135(16):164503, 2011. ISSN 0021-9606.

[113] McPherson A, Gavira JA. Introduction to protein crystallization. *Acta Crystallographica Section F Structural Biology Communications*, 70(1):2–20, 2014. ISSN 2053-230X.

[114] McPherson A. Crystallization of proteins from polyethylene glycol. *Journal of Biological Chemistry*, 251(20):6300–6303, 1976.

[115] Tanaka S, Ataka M. Protein crystallization induced by polyethylene glycol: A model study using apoferritin. *The Journal of Chemical Physics*, 117(7):3504–3510, 2002. ISSN 0021-9606.

[116] Yamanaka M, Inaka K, Furubayashi N, *et al.* Optimization of salt concentration in PEG-based crystallization solutions. *Journal of Synchrotron Radiation*, 18(1):84–87, 2011. ISSN 09090495.

[117] Svergun DI, Konarev PV, Volkov VV, *et al.* A small angle x-ray scattering study of the dropletâcylinder transition in oil-rich sodium bis(2-ethylhexyl) sulfosuccinate microemulsions. *The Journal of Chemical Physics*, 113(4):1651–1665, 2000. ISSN 0021-9606.

[118] Müller M, Stühn B, Busse K, *et al.* Modification of a reverse microemulsion with a fluorinated triblock copolymer. *Journal of Colloid and Interface Science*, 335(2):228–233, 2009. ISSN 00219797.

Publications

1. Björn Kuttich, Alexander Matt, Andreas Weber, Ann-Kathrin Grefe, Laura Vietze and Bernd Stühn. Water/PEG Mixtures: Phase Behavior, Dynamics and Soft Confinement. *Zeitschrift für physikalische Chemie*, **232(7-8)**, 1089-1110, (2017).

2. Alexander Matt, Björn Kuttich, Isabelle Grillo, Susann Weißheit, Christina M. Thiele and Bernd Stühn. Temperature induced conformational changes in the elastin-like Peptide GVG(VPGVG)$_3$. *submitted*, (2018).

3. Björn Kuttich, Alexander Matt and Bernd Stühn. Structure formation in water/PEG mixtures. *in preparation*, (2018).

Curriculum Vitae

Personal Information

Name	Alexander Daniel Matt
Date and place of birth	10. February 1990 in Hanau
Nationality	german

Academic Education

Feb. 2015 – Nov. 2018	Post-graduate student, TU Darmstadt, Germany
Dec. 2014	Master of Science (Physics), TU Darmstadt, Germany
Oct. 2012 – Dec. 2014	Physics studies, TU Darmstadt, Germany
Oct. 2012	Bachelor of Science (Physics), TU Darmstadt, Germany
Oct. 2009 – Oct. 2012	Physics studies, TU Darmstadt, Germany
Jun. 2009	Abitur, Franziskanergymnasium Kreuzburg in Grosskrotzenburg, Germany

Pratical Work

Feb. 2015 – present	Scientific staff member Institut für Festkörperphysik TU Darmstadt
Apr. 2012 – Sep. 2014	Student assistant